RIGA TECHNICAL UNIVERSITY

Marika Ščeglova

GALLIUM CONTAINING CALCIUM PHOSPHATES

Doctoral Thesis

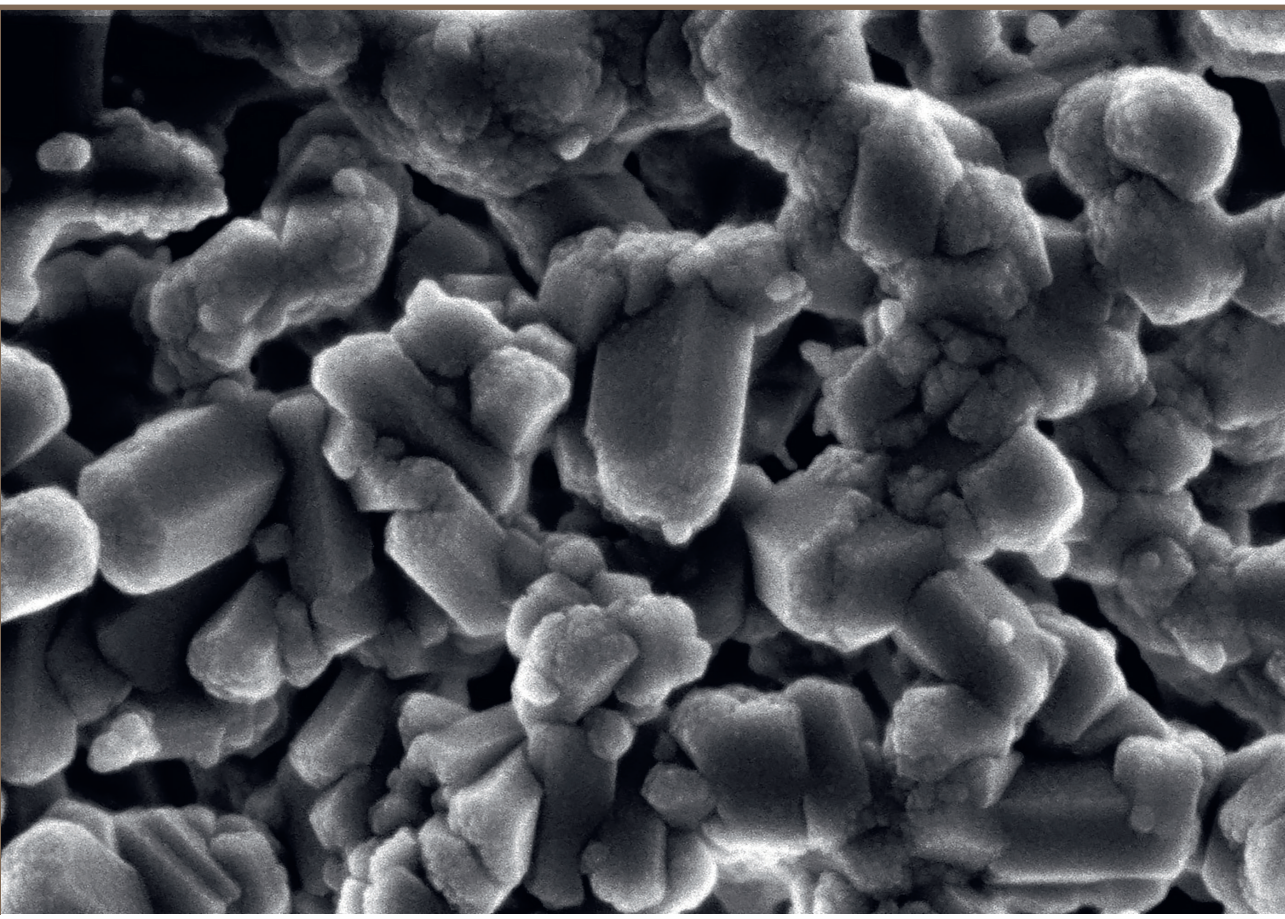

RTU Press
Riga 2026

RIGA TECHNICAL UNIVERSITY
Faculty of Natural Sciences and Technology
Institute of Biomaterials and Bioengineering

Marika Ščeglova
Doctoral Student of the Study Programme "Chemistry, Materials Science and Engineering"

GALLIUM CONTAINING CALCIUM PHOSPHATES

Doctoral Thesis

Scientific supervisors
Professor Dr. sc. ing
JĀNIS LOČS

Senior Researcher Dr. sc. ing.
LĪGA STĪPNIECE

RTU Press
Riga 2026

Ščeglova, M. Gallium Containing Calcium Phosphates. Doctoral Thesis. – Riga: RTU Press, 2026. 92 p.

Published in accordance with the decision of the Promotion Council "RTU P-02", January 26, 2026, Minutes No 04030- 9.2/3.

The Doctoral Thesis research was supported by the European Union`s Horizon 2020 research and innovation programme under grant agreements No. 857287 (BBCE), No. 952347 (RISEus2), and EuroNanoMedIII project "NANO delivery system for one-shot regenerative therapy of peri-implantis" (ImplantNano)**,** No. ES RTD/2020/19**.**

ACKNOWLEDGEMENTS

I would like to express my sincere gratitude to my family. My husband Artemijs for believing in me more than I believed sometimes in myself, for the support, encouragement and discussions outside of working hours. I am beyond grateful to share this journey and these accomplishments with him. Thanks to my biggest gift and motivator – my son Adrian, to my mother Galina, my mother-in-law Jelena, my nieces Arina, Sofia and Marija for believing in my strength and being there for me!

My heartfelt thanks to my friend Kristīne for support, encouragement, and the effort to understand what I do, for "the push" in those times when I felt like quitting!

Huge thanks to Renāts, an excellent student, for his dedication and responsiveness, and for being there for me in the laboratory.

To my esteemed colleagues at IBB for inspiring stories and fruitful scientific discussions, and their contribution to the creation of this Thesis. Additionally, I would like to sincerely thank Dr Nicola Dobelin for his valuable collaboration and for sharing his expertise with me.

Deepest gratitude to my supervisors, Senior Researcher Dr. sc. ing. Līga Stīpniece for her support, scientific ideas and Professor Dr. sc. ing Jānis Ločs, for the mentorship and knowledge provided!

In conclusion, I want to acknowledge myself for not giving up, moving through fears, challenges and self-doubt. This Thesis is not only about obtaining a degree but also about resilience and unwavering commitment to success.

"There is nothing to fear, because you cannot fail – only learn, grow, and become better than you've ever been before."

Hal Elrod

DOCTORAL THESIS PROPOSED TO RIGA TECHNICAL UNIVERSITY FOR PROMOTION TO THE SCIENTIFIC DEGREE OF DOCTOR OF SCIENCE

To be granted the scientific degree of Doctor of Science (PhD), the present Doctoral Thesis has been submitted for defence at the open meeting of RTU Promotion Council on April 24, 2026, at the Faculty of Natural Sciences and Technology of Riga Technical University, Paula Valdena street 3/7, room 272.

OFFICIAL REVIEWERS

Docent Dr. sc. ing. Gerda Gaidukova
Riga Technical University

Docent Dr. sc. ing. Agnese Brangule
Riga Stradiņš University, Latvia

Professor PhD Anna Tampieri
Institute of Science, Technology and Sustainability for Ceramics, Italy

DECLARATION OF ACADEMIC INTEGRITY

I hereby declare that the Doctoral Thesis submitted for review to Riga Technical University for promotion to the scientific degree of Doctor of Science is my own. I confirm that this Doctoral Thesis has not been submitted to any other university for promotion to a scientific degree.

Marika Ščeglova …… (signature)
Date: ……

The Doctoral Thesis has been prepared as a collection of thematically related scientific publications, completed by summaries in Latvian and English. The Doctoral Thesis unites four scientific publications. The scientific publications have been written in English, totaling 92 pages, including supplementary data.

TABLE OF CONTENTS

LIST OF ABBREVIATIONS

ACP – amorphous calcium phosphate
BET – Brunauer–Emmett–Teller method
CaP – calcium phosphate
CDHAp – calcium-deficient hydroxyapatite
DI – deionized
DMEM – Dulbecco's modified Eagle's medium
DSC – differential scanning calorimetry
FTIR – Fourier transform infrared spectroscopy
GaACP – gallium containing amorphous calcium phosphate
GaCaP – gallium containing calcium phosphate
GaHAp – gallium containing hydroxyapatite
HAp – hydroxyapatite
hTERT BJ1 – telomerase-immortalised human foreskin fibroblasts
ICDD – International Centre for Diffraction Data
OD_x – optical density (x – the wavelength at which the OD was measured, nm)
PBS – phosphate buffer saline
SCI – Science Citation Index
SEM/STEM – scanning electron microscopy/scanning transmission electron microscopy
SSA – specific surface area
TCP (α, β) – tricalcium phosphate (α, β)
TGA – thermogravimetric analysis
TSB – tryptic soy broth
XRD – X-ray diffraction

GENERAL OVERVIEW OF THE THESIS

Introduction

Bone is a composite material with a heterogeneous, anisotropic, and hierarchical structure. Its extracellular matrix consists of organic components (~ 30 %, mainly collagen fibril arrays) and an inorganic component (~ 70 %, composed primarily of nonstoichiometric hydroxyapatite (HAp) or biological apatite nanocrystals arranged within the collagen fibrils) [1]–[4]. The pathways of biological apatite formation are still unclear. One of the leading hypotheses proposes that the process begins with the amorphous calcium phosphate (ACP) *Posner* clusters, which transform into low-crystalline apatite [5]–[7]. Bone can regenerate itself. Namely, when bone gets damaged, it can naturally remodel through the coordinated actions of osteoclasts, osteoblasts, and osteocytes. However, defects that are critical in size (> 2 cm [8]) require additional treatment. Nevertheless, injuries, illnesses, or long-standing conditions such as osteoporosis and diabetes can hinder the healing process.

Regenerative medicine and bone tissue engineering offer a promising approach to enhance natural healing or replace damaged tissues using biomaterial implants and devices. One of the strategies involves using calcium phosphate (CaP) biomaterials, which are osteoconductive, biocompatible, and have high osseointegration ability [9]. Furthermore, CaP bioceramics can provide controlled biodegradation through the dissolution-precipitation process, allowing integration and replacement of the implant material with the new bone tissue [10], [11]. They can be produced in various forms, including powders, pellets, and scaffolds [12], [13]. Moreover, their versatility in composition, porosity, and mechanical properties allows customisation to meet specific application requirements [14], [15].

HAp is the most widely used CaP phase in the biomaterial field due to its chemical and structural similarity to the native bone tissues [16], [17]. Its chemical formula is $Ca_{10}(PO_4)_6(OH)_2$, and Ca/P molar ratio is 1.67 [18]. HAp possesses high thermodynamic stability and low solubility (pKsp 117.3 (at 37 °C) [19]). On the other hand, ACP is a metastable phase characterised by a short-range atomic order structure with chemical formula $Ca_xH_y(PO_4)_z{\cdot}nH_2O$ (Ca/P molar ratio 1.5) [20], [21]. Besides, it serves as a precursor phase in the precipitation process of other CaPs [21]. ACP offers advantages over HAp, such as higher solubility and faster resorption rate attributed to its hydrated layer and lack of crystallinity [22], [23].

Nowadays, tissue regeneration has become more predictable, addressing and satisfying the diverse needs of patients due to the advancement of the biomaterial field. However, any biomaterial possesses a risk of infection, as the properties that make them suitable for use in living organisms also create favourable conditions for bacteria. In orthopaedic surgeries, the primary complication is biomaterial-associated infections, especially in hip and knee replacements [24]. For instance, the rate of periprosthetic joint infections ranges from 0.7 % to 4 %, but after revision surgery, this rate can rise up to 20 % [25]–[31]. The predominant pathogens involved are gram-positive bacteria, with *Staphylococcus aureu*s (*S. aureus*) causing 33–43 % of infections and *Staphylococcus epidermidis* (*S. epidermidis*) being responsible for

17–21 % of cases [30], [32], [33]. Gram-negative bacteria, such as *Pseudomonas aeruginosa (P. aeruginosa)*, are less frequent and account for approximately 6 % of cases [34]. Systematic antibiotic administration is the traditional approach to treating biomaterial-associated infections. Still, it often results in systemic toxicity, low drug accumulation in the target site, and contributes to antibiotic resistance, especially in the case of *P. aeruginosa*. Consequently, antibiotics are ineffective against biofilms, which are a major cause of implant failure [33].

Before the discovery of antibiotics, different metals and their ions were used as antibacterial agents [35], [36]. It has paved the way for modern strategies, including modifying biomaterials with metal ions to enable long-term local ion release, providing antibacterial action at the defect site [37]. Commonly used metal ions for these modifications include silver (Ag^{+}), zinc (Zn^{2+}), strontium (Sr^{2+}), sodium (Na^{+}), and copper (Cu^{2+}), among others, which have demonstrated antibacterial activity against various pathogens [38]. Additionally, biologically relevant metal ions such as calcium (Ca^{2+}), iron (Fe^{2+}), magnesium (Mg^{2+}), and manganese (Mn^{2+}) play a crucial role in bacterial protein metabolism and overall physiological functions [39], [40].

Literature Review (Paper 1)

Gallium (Ga) and its compounds have been studied since the 1970s and have recently gained interest as therapeutic agents due to their antibacterial [41], [42], antitumor [43], and anti-inflammatory [44] properties. Unlike conventional antibiotics, Ga^{3+} ions can target tumours and infectious sites without inducing drug resistance [45]. Ga^{3+} ion has demonstrated antibacterial efficacy against both gram-positive and gram-negative bacteria, primarily due to its ability to mimic Fe^{3+} in bacterial metabolism (Fig. 1) [46], [47]. This "*Trojan horse*" strategy involves Ga^{3+} being "mistakenly" incorporated into bacterial iron-dependent processes, such as transferrin, heme-containing proteins, and siderophores [48]–[50]. As a result, bacterial metabolism is disrupted, leading to impaired DNA synthesis, respiration, and oxidative stress responses.

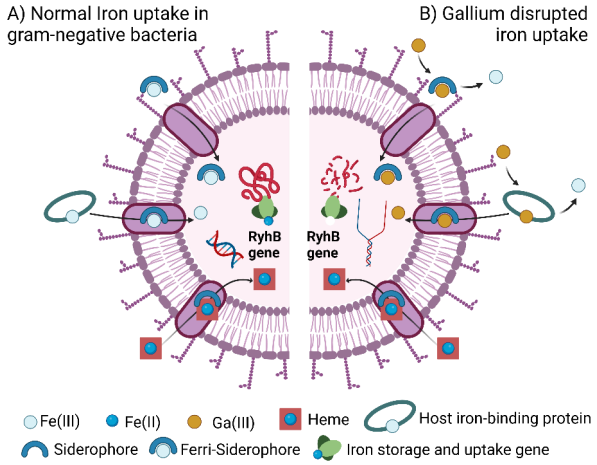

Fig. 1. A – Normal iron uptake metabolism in gram-negative bacteria; B – gallium disrupted iron uptake metabolism in gram-negative bacteria (adapted from [51], created with *Biorender.com*) [52].

A suitable carrier is required to deliver Ga^{3+} ions directly into the surgical site. Accordingly, Ga-containing CaPs (GaCaPs) can serve as controlled-release carriers for localised therapeutic action. Of the wide range of CaPs, only a few representatives have been modified with Ga, i.e., ACP, HAp, and β-tricalcium phosphate (β-TCP).

Up to now, only one study had documented Ga-containing ACP (GaACP) produced through the sol-gel method, showing antibacterial activity against *P. aeruginosa* as the (Ca + Ga)/P molar ratio increased [53]. However, this study did not cover an investigation into the stability of GaACP and antibacterial activity against other bacterial species. Regarding Ga-containing HAp (GaHAp), several studies have been reported in scientific literature. Usually, the low-crystallinity HAp with Ga content ranging from 0.33 wt% to 13 wt% has been synthesised using various synthesis methods. It has been reported that GaHAp exhibits antibacterial properties against *P. aeruginosa*, *Pseudomonas fluorescens* (*P. fluorescens*) [54]–[56]. Nonetheless, the existing literature does not address high-temperature GaHAp bioceramics, and the comprehension of Ga substitution remains limited [53].

From the literature review, it was concluded that the synthesis method and processing of the precipitates significantly influence the incorporation of Ga into the CaPs' crystalline structure, impacting the Ga^{3+} ion release profile and biological performance of CaPs. Thus, the Thesis concentrated on conducting systematic research regarding the influence of Ga on the properties of CaPs, highlighting the scarcity of studies concerning the stability of GaACP and the GaHAp bioceramics produced at various sintering temperatures. In the Thesis, the stability and antibacterial properties of GaACP were assessed, the *in vitro* antibacterial activity and cytotoxicity of GaHAp were examined, and high-temperature GaHAp bioceramics were prepared and characterised.

Aim and Objectives

The Thesis aimed to investigate the influence of gallium ions on the physicochemical properties of amorphous calcium phosphate and hydroxyapatite and to explore *in vitro* biological properties of the obtained materials. To achieve this aim, the following objectives were set.

1. To study the influence of gallium on amorphous calcium phosphate physicochemical properties, thermal stability, stability in aqueous solution of different compositions, and to investigate antibacterial activity.
2. To evaluate the influence of gallium on the hydroxyapatite physicochemical properties and to determine the optimal gallium concentration in hydroxyapatite to achieve antibacterial properties without causing toxic effects on cells.
3. To investigate the impact of gallium on the thermal stability of hydroxyapatite and to locate possible gallium position in the hydroxyapatite crystal lattice after sintering at different temperatures.

Theses to Defend

1. The addition of gallium delays the crystallisation of amorphous calcium phosphate in various aqueous media and thermally induced crystallisation.
2. Optimal gallium content in the hydroxyapatite can ensure the balance of antibacterial activity and cytocompatibility.
3. Gallium substitutes calcium in the hydroxyapatite lattice, leading to an increase in lattice unit cell volume, affecting the thermal stability and phase composition of hydroxyapatite bioceramics at different sintering temperatures.

Scientific Novelty

The scientific novelty was recognised in the following aspects.

1. For the first time, the influence of gallium on the amorphous calcium phosphate's stability in various aqueous media was studied.
2. The antibacterial activity of gallium containing amorphous calcium phosphate against *S. aureus* was studied.
3. For the first time, the theoretical substitutional structure model of gallium containing hydroxyapatite was developed using *Profex* software and electron density maps.

Practical Significance

The obtained calcium phosphates with enhanced properties such as improved stability, bioactivity, and antibacterial properties could find wide clinical applications, including bone regeneration, implant coatings, and antibacterial biomaterials. Furthermore, understanding the stability of amorphous calcium phosphate will enhance the reliability and longevity of the application. Antibacterial properties provided by gallium addition to the calcium phosphate

biomaterials can reduce antibiotic usage in the bone regeneration field. By reducing the risk of infections in the early stage, improved healing and regeneration will be achieved.

Structure and Volume of the Thesis

This Doctoral Thesis was prepared as a collection of thematically related scientific publications dedicated to gallium containing calcium phosphates. This Thesis unites three original publications and one review article published in international, peer-reviewed, open-access scientific journals indexed in the Science Citation Index (SCI).

Publications and Approbation of the Thesis

The results of the Thesis were published in four SCI scientific publications.

Paper 1: Mosina, M., Kovrlija, I., Stipniece, L., Locs, J. Gallium containing calcium phosphates: Potential antibacterial agents or fictitious truth. *Acta Biomaterialia*, **2022**, *150*, 48–57. https://doi.org/10.1016/j.actbio.2022.07.063 (pen Access, IF 9.6, Q1, CiteScore 17.8).

- The author contributed to the publication by conceptualisation, investigation, visualisation, writing the original draft, reviewing and editing (in total 80/100 %).

Paper 2: Vasiljevs, R., Sceglova, M., Stipniece, L., Locs, J. Insights into physicochemical properties, stability in various aqueous media, and antibacterial activity of gallium-containing amorphous calcium phosphates. *Scientific Reports*, **2025**, *15*, 26976. https://doi.org/10.1038/s41598-025-12906-7 (Open Access, IF 3.9, Q1, CiteScore 6.7).

- The author contributed to the publication through conceptualisation, data curation, formal analysis, reviewing and editing (in total 45/100 %).

Paper 3: Mosina, M., Siverino, C., Stipniece, L., Sceglovs, A., Vasiljevs, R., Moriarty, T. F., Locs, J. Gallium-doped hydroxyapatite shows antibacterial activity against *Pseudomonas aeruginosa* without affecting cell metabolic activity. *J. Funct. Biomater.* **2023**, *14*, 51. https://doi.org/10.3390/jfb14020051 (Open Access, IF 5.2, Q2, CiteScore 6.8).

- The author contributed to the publication through conceptualisation, investigation, data curation, formal analysis, visualisation, writing the original draft, reviewing and editing (in total 70/100 %).

Paper 4: Sceglova, M., Döbelin, N., Vasiljevs, R., Stipniece, L., Locs, J. Influence of gallium doping on the thermal stability and microstructure of sintered hydroxyapatite bioceramics. *Ceramics International* **2025**, *51*(14), 41150–42261. https://doi.org/10.1016/j.ceramint.2025.06.440 (Open Access, IF 5.6, Q1, CiteScore 9.1).

- The author contributed to the publication through conceptualisation, investigation, data curation, formal analysis, visualisation, writing the original draft, reviewing and editing (in total 80/100 %).

The results of the Thesis were presented at 11 scientific conferences.

1. **Mosina, M**., Siverino, C., Stipniece, L., Sceglovs, A., Vasiljevs, R., Moriarty, T. F., Locs, J. Biocompatible gallium doped hydroxyapatite. *Scandinavian Society for Biomaterials*, Jurmala, Latvia, June 2021, online (oral presentation).
2. **Mosina, M**., Siverino, C., Stipniece, L., Sceglovs, A., Vasiljevs, R., Moriarty, T. F., Locs, J. Biocompatible gallium doped hydroxyapatite. *Scandinavian Society for Biomaterials*, Jurmala, Latvia, June 2022 (oral presentation).
3. **Mosina, M**., Siverino, C., Stipniece, L., Sceglovs, A., Vasiljevs, R., Moriarty, T. F., Locs, J. Effect of gallium doped hydroxyapatite on *P.aeruginosa* bacteria growth. *Tissue Engineering and Regenerative Medicine International Society (TERMIS) European Chapter Conference*, Krakow, Poland, July 2022 (oral and poster presentation).
4. **Mosina, M**., Vasiljevs, R., Stipniece, L., Locs, J. Gallium ion effect on calcium phosphate ceramic phase composition. *Bioceramics32*, Venice, Italy, September 2022 (poster presentation).
5. Stipniece, L., **Mosina, M.**, Locs, L., Effect of Gallium on physicochemical characteristics of hydroxyapatite, *3rd Biennial Conference Biomaterials and Novel Technologies for Healthcare* (*BioMaH 2022*), Rome, Italy, October 2022 (poster presentation).
6. Vasiljevs, R., **Mosina, M.**, Crystallization kinetics of gallium-containing amorphous calcium phosphate in different media, *Riga Technical University Student Scientific and Technical Conference*, Riga, Latvia, April 2023 (oral presentation).
7. Vasiljevs, R., **Sceglova, M.**, Stīpniece, L., Ločs, J. Gallium containing amorphous calcium phosphate crystallization kinetics in different media. *Materials Science and Applied Chemistry conference of RTU* (*MSAC 2023*), Riga, Latvia, October 2023 (poster presentation).
8. Vasiljevs, R., **Sceglova, M.**, Stīpniece, L., Ločs, J. Effect of gallium content on crystallization and sinterability of amorphous calcium phosphate. *Riga Technical University Student Scientific and Technical Conference*, Riga, Latvia, April 2024 (oral presentation).
9. Vasiljevs, R., **Sceglova, M**., Stīpniece, L., Ločs, J. Synthesis, characterization and sintering of gallium containing amorphous calcium phosphate. *Riga Technical University Student Scientific and Technical Conference,* Riga, Latvia, April 2025 (oral presentation).
10. **Sceglova, M**., Döbelin, N., Vasiljevs, R., Stipniece, L., Locs, J., Gallium-doped hydroxyapatite and its properties, *The XIXth Conference of the European Ceramic Society* (*ECerS 2025*), Dresden, Germany, September 2025 (poster presentation).
11. Vasiljevs, R., **Sceglova, M**., Stipniece, L., Locs, J. Effect of gallium content on stability and sinterability of amorphous calcium phosphate. *The XIXth Conference of the European Ceramic Society* (*ECerS 2025*), Dresden, Germany, September 2025 (oral and poster presentations).

Other scientific publications published during the development of the Thesis.

1. Stipniece, L., Skadins, I., **Mosina, M**. Silver- and/or titanium-doped β-tricalcium phosphate bioceramic with antibacterial activity against *Staphylococcus aureus*. *Ceramics International*, **2022**, 48(7), 10195–10201. https://doi.org/10.1016/j.ceramint.2021.12.232.
2. Irtiseva, K., **Mosina, M**., Tumilovica, A., Lapkovskis, V., Mironovs, V., Ozolins, J., Stepanova, V., Shishkin, A. Application of granular biocomposites based on homogenised peat for absorption of oil products. *Materials,* **2022**, *15*, 1306. https://doi.org/10.3390/ma15041306.
3. Rezevska, D., Stipniece, L., Rubene, L., **Sceglova, M.**, Maurins, S., Vasiljevs, R., Racenis, K., Kroica, J. Zinc-substituted hydroxyapatite-bacteriophage complexes for complementary antibacterial properties. *Colloids Surf. A*, **2025***, 720*, 137114. https://doi.org/10.1016/j.colsurfa.2025.137114.
4. Sceglovs, A., Siverino, C., Skadins, I., Pirsko, V., Sceglova, M., Kroica, J., Moriarty, F. T., Salma-Ancane, K. Injectable ε-polylysine/hyaluronic acid hydrogels with resistance preventing antibacterial activity for treating wound infections. *ACS Applied Bio Materials,* **2025**, https://doi.org/10.1021/acsabm.5c01252.

MAIN RESULTS OF THE THESIS

GaACP and its Properties (Paper 2)

Syntheses of the ACP powders were performed using a modified wet chemical precipitation method at ambient temperature (20 ± 2 °C). Precipitation of the ACP was induced by the rapid addition of 3M NaOH aqueous solution to an acidic solution containing Ca^{2+} (from $CaCl_2 \cdot 2H_2O$), Ga^{3+} (from $Ga(NO_3)_3 \cdot 9.5H_2O$), and PO_4^{3-} (from H_3PO_4) ions, reaching pH 10.3 ± 0.2. To achieve different Ga contents in the synthesis products, various amounts of $Ga(NO_3)_3 \cdot 9.5H_2O$ were added in the synthesis medium, while the (Ca + Ga)/P (Ca/P for Ga-free ACP) molar ratio of the raw materials was kept constant at 1.67. The sample series were labelled Ref-ACP, 2GaACP, 4GaACP, 6GaACP, and 12GaACP, considering the theoretical Ga content 0 wt%, 2 wt%, 4 wt%, 6 wt%, and 12 wt%, respectively.

The as-synthesised and heat-treated powders were analysed using comprehensive characterisation methods. The phase composition was studied using the X-ray diffraction technique (XRD, *PANalytical Aeris*, The Netherlands), and the crystalline phase identification was done using the PDF-2 database from the International Centre for Diffraction Data (ICDD). The functional groups were analysed using a Fourier transform infrared spectrometer (FTIR, *Nicolet iS 50*, *Thermo Scientific*, USA). The morphology was characterised using a scanning electron microscope (SEM, *Verios 5 UC*, *Thermo Fisher Scientific*, USA) coupled with a scanning transmission electron microscopy (STEM) detector. Specific surface area (SSA_{BET}) of the as-synthesised powders was determined using the *Brunnauer–Emmet–Teller* method (BET) and a QUADRASORB SI instrument (Quantachrome Instruments, USA). True density was determined using a He pycnometer (PYC, *Micro UltraPyc 1200e*, *Quantachrome Instruments*, USA). To evaluate the thermal stability of the as-synthesised powders, thermogravimetric analysis (TGA) combined with differential scanning calorimetry (DSC) was performed using a simultaneous TGA/DSC instrument (TGA/DSC 3+, *Mettler Toledo*, Switzerland).

Regardless of Ga content, all as-synthesised powders were X-ray amorphous, exhibiting a broad diffraction maximum at 30° 2θ, characteristic of ACP (Fig. 2A) [57]–[59].

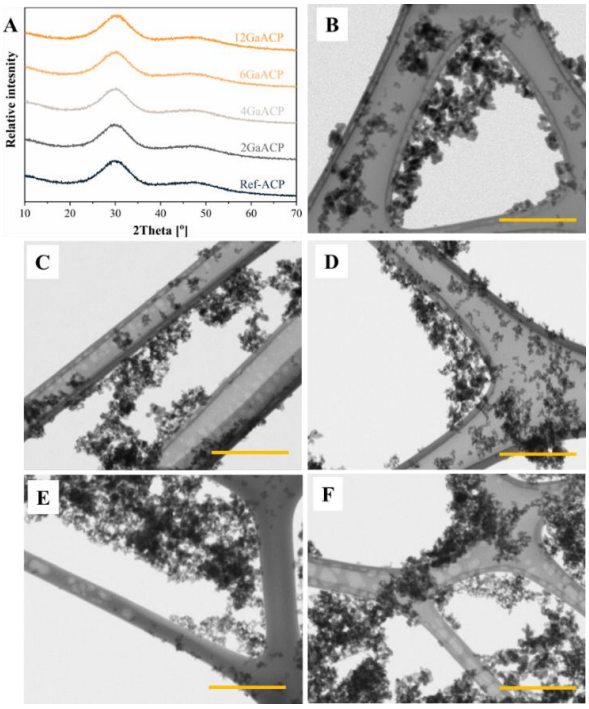

Fig. 2. A – XRD patterns of the Ref-ACP and GaACP powders; STEM microphotographs of B – Ref-ACP, C – 2GaACP, D – 4GaACP, E – 6GaACP, and F –12GaACP powders. Scale bar – 300 nm.

Both the Ref-ACP and GaACP powders had high SSA_{BET} (Table 1), which correlates with available data in the literature [60].

Table 1

Ga content and morphological characteristics of the as-synthesised ACP powders

Sample	Nominal Ga content [wt%]	Measured Ga content [wt%]	SSA_{BET} [m^2/g]	**ρ** [g/cm^3]	d_{BET} [nm]
Ref-ACP	-	-	167 ± 4	2.50 ± 0.02	14 ± 1
2GaACP	2	0.6 ± 0.1	159 ± 5	2.54 ± 0.06	15 ± 1
4GaACP	4	1.3 ± 0.2	151 ± 7	2.49 ± 0.05	16 ± 1
6GaACP	6	1.7 ± 0.1	163 ± 1	2.47 ± 0.02	15 ± 1
12GaACP	12	2.2 ± 0.1	165 ± 18	2.47 ± 0.04	15 ± 2

There is a threshold for Ga incorporation into the ACP structure. The measured content of Ga was significantly lower than nominal values and did not exceed 2 wt% even for samples with the nominal Ga concentration of 6 wt% and 12 wt% (Table 1). ACP exhibits a disordered structure characterised by the absence of long-range crystalline order. ACP particles are composed of randomly arranged *Posner* clusters with an average size of approximately 0.95 nm, which are surrounded by a hydrated layer (up to 25 %) filling in the intercluster space

[61]. The hydrated layer hinders the incorporation of foreign ions, which can explain the limited incorporation of Ga in the ACP. Alternatively, the Ga^{3+} ions that dissociated during the initial synthesis solution may hydrolyse into insoluble hydroxide ($Ga(OH)_3$), which has low bioavailability [46] and does not contribute to the precipitation of GaACP. STEM microphotographs revealed that the Ref-ACP and GaACP powders are composed of nano-sized spheroidal particles (Fig. 2 B–F). The results suggest that Ga does not significantly influence the morphological characteristics of the ACP.

DSC curves show similar thermal effects for both the ACP and the GaACP samples (Fig. 3 A).

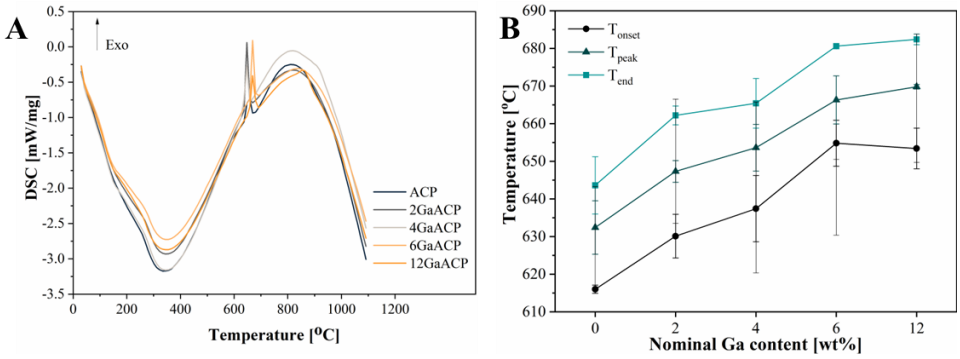

Fig. 3. A – DSC curves of the Ref-ACP and GaACP powders; B – the characteristic phase transition temperatures [unpublished data].

The endothermic peak up to 350 °C corresponds to the release of the free and chemically bonded water and CO_2. This process does not cause the crystallisation of ACP and GaACP. Somrani et al. concluded that water molecules do not directly interact with phosphate groups, and their loss does not change the structure of ACP [62]. An exothermic peak between 615 °C and 680 °C (Fig. 3 A) corresponds to ACP crystallisation into a more stable CaP phase, accompanied by heat release [22], [63]. The addition of Ga improved the thermal stability of ACP; i.e., with increasing Ga content, the crystallisation temperature increased (Fig. 3 B). This observation agrees with the scientific literature, suggesting that the thermal stability of ACP depends on the presence of impurities, namely, stabilising agents (ions or molecules of other metals or non-metals), which contribute to the shift of the phase transition or crystallisation point towards higher temperatures [22], [64]. An additional exothermic effect was observed at 861 °C for the sample with the highest Ga concentration (12GaACP), which could be associated with the crystallisation of the $Ga_x(OH)_yO_z$ cluster. The presence of those clusters was observed by Yang et. al. using NMR analysis [53].

To investigate the thermal stability of the GaACP powders, they were heat-treated at temperatures ranging from 300 °C to 1200 °C, and the phase composition of the heat-treated powders was analysed using XRD patterns (Fig. 4).

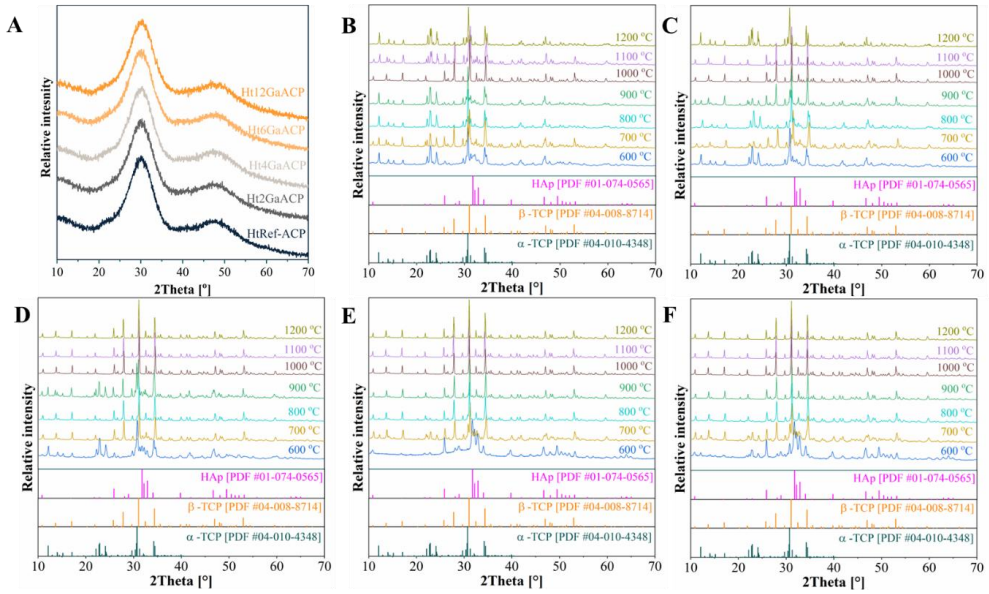

Fig. 4. XRD patterns of the heat-treated powders: A – ACP and GaACP at 300 °C; B – Ref-ACP; C – 2GaACP; D – 4GaACP; E – 6GaACP; F – 12GaACP at 600–1200 °C [unpublished data].

Table 2

Phase composition of the ACP and GaACP powders heat-treated at different temperatures (in each mixture, the phase written first is the major component, i.e., it is present in a higher amount than other phases) [unpublished data]

Temp. [°C]	**Sample series**				
	Ref-ACP	**2GaACP**	**4GaACP**	**6GaACP**	**12GaACP**
300	amorphous	amorphous	amorphous	amorphous	amorphous
600	α-TCP/HAp	α-TCP/HAp/ β-TCP	α-TCP/HAp/ β-TCP	HAp/β-TCP	HAp/α-TCP
700	β-TCP/α-TCP/ HAp	β-TCP/α-TCP/ HAp	β-TCP/HAp/ α-TCP/	β-TCP/α-TCP/ HAp	β-TCP/α-TCP/ HAp
800	α-TCP/β-TCP/ HAp	α-TCP/β-TCP/HAp	β-TCP/α-TCP/ HAp	β-TCP/α-TCP/ HAp	β-TCP/α-TCP/ HAp
900	β-TCP/α-TCP/ HAp	β-TCP/α-TCP/ HAp	α-TCP/β-TCP/HAp	β-TCP/HAp/α-TCP/	β-TCP/HAp
1000	β-TCP/α-TCP/ HAp	β-TCP/α-TCP/ HAp	β-TCP/α-TCP/ HAp	β-TCP/α-TCP/ HAp	β-TCP/α-TCP/ HAp
1100	β-TCP/α-TCP/ HAp	β-TCP/α-TCP	β-TCP/α-TCP/ HAp	β-TCP/HAp	β-TCP/HAp
1200	α-TCP/β-TCP	α-TCP/β-TCP	β-TCP/α-TCP	β-TCP/α-TCP	β-TCP/α-TCP

Regardless of Ga content, the ACP powders remained X-ray amorphous after heat treatment at 300 °C (Fig. 4 A). However, increasing the heat treatment temperature to 600 °C and above induced the formation of various CaP phases (Fig. 4 B–F). The phase composition of the heat-

treated powders was a mixture of two or three phases compromising α-TCP, β-TCP, and HAp in different ratios (Table 2).

Usually, α-TCP or β-TCP is formed from ACP after heat treatment at temperatures above 600 °C, as the ACP Ca/P molar ratio is 1.5, which corresponds to TCP [65]. However, in our study, we observed the formation of the HAp phase. This is explained by the synthesis conditions, namely, a higher Ca/P molar ratio (Ca + Ga/P = 1.67 and Ca/P = 1.67) in the synthesis medium, and the possible presence of carbonate ions (incorporating or substituting phosphate groups) into the structure of the as-synthesised Ref-ACP and GaACP. The carbonate ions leave the ACP structure during heat treatment, increasing the Ca/P molar ratio, thus promoting the formation of HAp [66]. Nevertheless, there is no correlation between Ga content, temperature and phase composition of the final products after heat treatment. ACP atomic arrangement is inherently disordered and non-uniform, resulting in unpredictable phase composition after heat treatment.

Due to the metastable nature of ACP in aqueous media, it is important to evaluate its behaviour under *in vitro* experimental conditions. Different factors, such as pH, ionic doping, and additives, affect ACP stability in aqueous media. The elucidation of stability will help to understand material behaviours and optimise material formulations for specific biomedical environments and applications.

Ga's influence on the stability of ACP in aqueous media

The stability of GaACP powder was evaluated in deionised water (DI H_2O), phosphate buffer solution (PBS), Dulbecco's modified Eagle's medium (DMEM) and tryptic soy broth (TSB). The powder and liquid media ratio was 6 mg/L. Samples were incubated at 37 °C with orbital shaking at 80 rpm for 20 min, 40 min, 60 min, and 90 min, and 4 h, 24 h, and 48 h. The stability time of powders in different aqueous media is summarised in Fig. 5 A.

In vitro stability of the powders was evaluated by XRD, where the formation and narrowing of diffraction maxima characteristic of the apatitic CaP phase at 26^o and 32^o 2θ was observed (Fig. 5B-F) [67]. Rapid crystallisation of ACP in PBS regardless of Ga content was observed. It is related to the presence of phosphate ions in the media, which accelerates the nucleation and precipitation of new particles following a dissolution-recrystallisation mechanism [68]–[70]. The significant effect of Ga on the ACP stability was observed in DI H_2O, DMEM (Fig. 5 B–F), and TSB. In DMEM, the stability of the ACP increased gradually with the Ga content. DMEM was buffered with $NaHCO_3$, thus supplementing the media with carbonate ions or causing precipitation of calcite, which, in turn, can contribute to the stabilisation of ACP [22], [64], [71], [72].

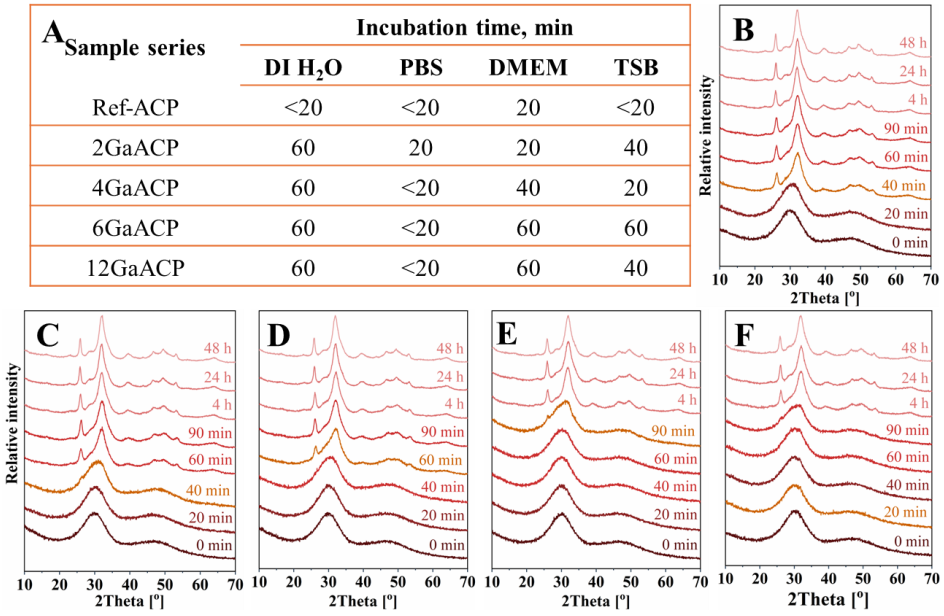

A Sample series	Incubation time, min			
	DI H_2O	PBS	DMEM	TSB
Ref-ACP	<20	<20	20	<20
2GaACP	60	20	20	40
4GaACP	60	<20	40	20
6GaACP	60	<20	60	60
12GaACP	60	<20	60	40

Fig. 5. A – Stability time of the Ref-ACP and GaACP powders in different aqueous media. XRD patterns after incubation in DMEM: B – Ref-ACP, C – 2GaACP, D – 4GaACP, E – 6GaACP, and F – 12GaACP [Paper 2].

Additionally, in the literature, there is evidence that organic molecules stabilise the ACP phase. Still, it depends on the type of organic molecules and their concentration [73]–[75]. Both TSB and DMEM contain amino acids, vitamins and proteins, which can be adsorbed onto the surface of the ACP nanoparticle, thereby stabilising them. The stability tests revealed that not only does Ga ion influence the stability, but also the composition of the media.

After understanding ACP performance in the *in vitro* media, the next step is to evaluate antibacterial activity. It is known that Ga possesses antibacterial properties. Moreover, Yang et al. revealed that GaACP has an inhibitory effect on the growth of *P. aeruginosa* [53]. However, it is important to evaluate the potential inhibition effect also against *S. aureus*, as it is a major contributor to infections associated with biomaterials, especially in orthopaedic surgeries.

Evaluation of GaACP antibacterial activity

Antibacterial properties were assessed against *P. aeruginosa* (ATCC 23863) and *S. aureus* (ATCC 25923) by measuring optical density at 620 nm (OD_{620}) of bacterial growth for 20 h at 37 °C in TSB by using a spectrophotometer (*MultiskanFC, Thermo Scientific*, USA) (Fig. 6).

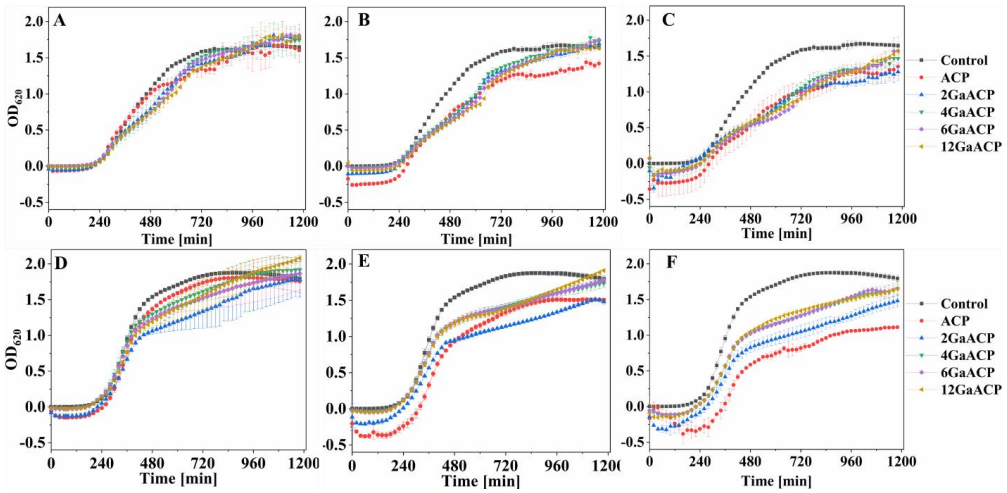

Fig. 6. *P. aeruginosa* growth kinetic curves in the presence of the GaACP powder suspensions in TSB at: A – 1 mg/mL, B – 2 mg/mL, and C – 4 mg/mL. *S. aureus* growth kinetic curves in the presence of the GaACP powder suspensions in TSB media at: D – 1 mg/mL, E – 2 mg/mL, and F – 4 mg/mL. The represented OD_{620} values were obtained by subtracting the initial $OD_{620\text{-}0\_h}$ (starting time = 0 h) from the measured $OD_{620\text{-}x\_h}$ at specific time points, i.e., x h.

No significant differences in the *P. aueruginosa* and *S. aureus* bacteria growth curves were observed for the ACP and GaACP powders at 1 mg/mL concentration in TSB. By increasing powder concentration to 2 mg/mL, the delayed exponential growth (log phase) compared to the control was observed against both bacterial strains. At the powder concentration of 4 mg/mL, the inhibitory effect became more pronounced and differed between bacterial strains. In the case of *S. aureus*, at a powder concentration of 4 mg/mL, the ACP and GaACP showed similar bacterial growth inhibition effects. A more pronounced impact of Ga content was noted in the *P. aeruginosa* culture, which lacked a distinct log phase (exponential) and could not achieve a stationary phase. Thus, the bacteriostatic effect of Ga was indirectly revealed. However, this effect can also be related to the nanosized ACP and GaACP particles, which can adversely affect bacteria by damaging cell membranes, hindering DNA synthesis, and interfering with metabolic functions [76]–[78]. Additionally, bacteria grow exponentially in the presence of other CaP phases, non-amorphous, as from stability studies (Fig. 5 A). After 40 min, all samples converted to a more stable CaP phase, Ca-deficient HAp (CDHAp). It is still unclear whether Ga^{3+} ions are being released into the solution during this process or are incorporated into the crystal structure of CDHAp.

The first objective of the research was successfully achieved, demonstrating that Ga does not influence the physicochemical properties of the ACP powder, while the presence of Ga affected the stability of ACP. The GaACP powders did not show sufficient antibacterial activity for potential use in treating infection. Accordingly, research was conducted to determine how Ga affects HAp, where potentially higher Ga incorporation levels and antibacterial activity could be achieved.

GaHAp and its Properties (Paper 3)

The HAp powders with different Ga content (Fig. 7 A) and (Ca + Ga)/P (Ca/P for Ga-free HAp) molar ratio of 1.67 were synthesised via the wet chemical precipitation method from calcium oxide (CaO), gallium nitrate hydrate ($Ga(NO_3)_3 \cdot 9.5H_2O$) and phosphoric acid (H_3PO_4). 2M H_3PO_4 aqueous solution was added to the Ca^{2+} and Ga^{3+} ions containing suspension with a 1 mL/min addition rate, continuous stirring at 150 rmp until the pH 6.90 ± 0.05 at 45 °C was reached. The obtained precipitates were aged overnight in the mother liquors, vacuum-filtered and dried at 105 °C (overnight). The as-synthesised samples were labelled as HAp, 2GaHAp, 4GaHAp, 6.3GaHAp, and 8GaHAp and characterised with multiple analysis techniques (XRD, FTIR, BET) described above in section "GaACP and its Properties (Paper 2)". *In vitro* Ga^{3+} ion release tests were performed in DMEM for GaHAp paste (non-dried sample, filtered precipitates) for up to 30 days.

Low-intensity maxima characteristic of low-crystalline apatite were detected in the XRD patterns of all samples (Fig. 7 B). The addition of Ga reduced particle size and increased SSA_{BET} compared to Ga-free HAp (Fig. 7 A), suggesting that Ga inhibits HAp crystal growth. The adsorption of smaller ions, such as Ga^{3+} (0.62 Å [79]) compared to Ca^{2+} (1.00 Å [79]), on the HAp crystal surface results in the inhibition of crystallisation and crystal growth as suggested in the literature [54], [55], [80], [81].

A Sample	Theoretical Ga content [wt%]	Gallium content [wt%]	SSA_{BET} [m^2/g]	ρ [g/cm^3]	d_{BET} [nm]
HAp	-	-	71 ± 7	2.77 ± 0.04	31 ± 3
2GaHAp	2	1.6 ± 0.1	95 ± 5	2.85 ± 0.06	22 ± 1
4GaHAp	4	3.3 ± 0.4	117 ± 4	2.80 ± 0.06	18 ± 1
6.3GaHAp	6.3	5.5 ± 0.1	109 ± 2	2.83 ± 0.01	20 ± 1
8GaHAp	8	6.9 ± 0.5	102 ± 5	2.79 ± 0.03	21 ± 1

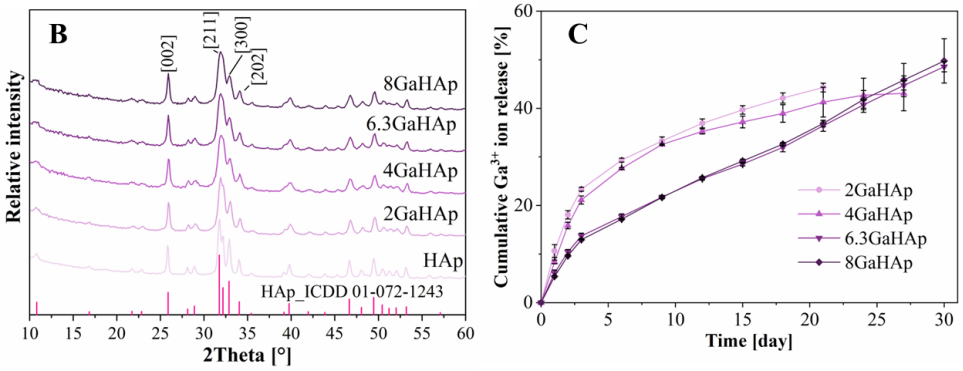

Fig. 7. A – Physicochemical parameters of the as-synthesised HAp and GaHAp powders; B – XRD patterns of the as-synthesised HAp and GaHAp powders; C – cumulative Ga^{3+} ion release in DMEM media at 37 °C (n = 3 ± SD) [82].

Due to this effect, it cannot be ruled out that the synthesised HAp powders may contain amorphous phase impurities. Furthermore, increasing of the Ga content resulted in a decrease

in the Ca/P molar ratio in the final products. Thus, it can be claimed that the obtained products are non-stoichiometric HAp or CDHAp. The results of *in vitro* Ga^{3+} ion release tests (Fig. 7 C) demonstrated the potential for long-term antibacterial ion delivery, with up to 43 % of Ga released into the media over 27 days.

***In vitro* evaluation of GaHAp**

The antibacterial properties of the GaHAp powders were analysed by assessing the growth of five different bacterial cultures – *P. aeruginosa* (Paer09), *E. coli* (ATCC 25922), *S. epidermidis* (ATCC 35984), *S. aureus* (JAR 06013), and *Streptococcus pyogenes (S. pyogenes*, ATCC 19615) at 37 °C for 18 h by measuring the optical density at 600 nm (OD_{600}) using a spectrophotometer (*MultiskanGo; Thermo Scientific*, USA).

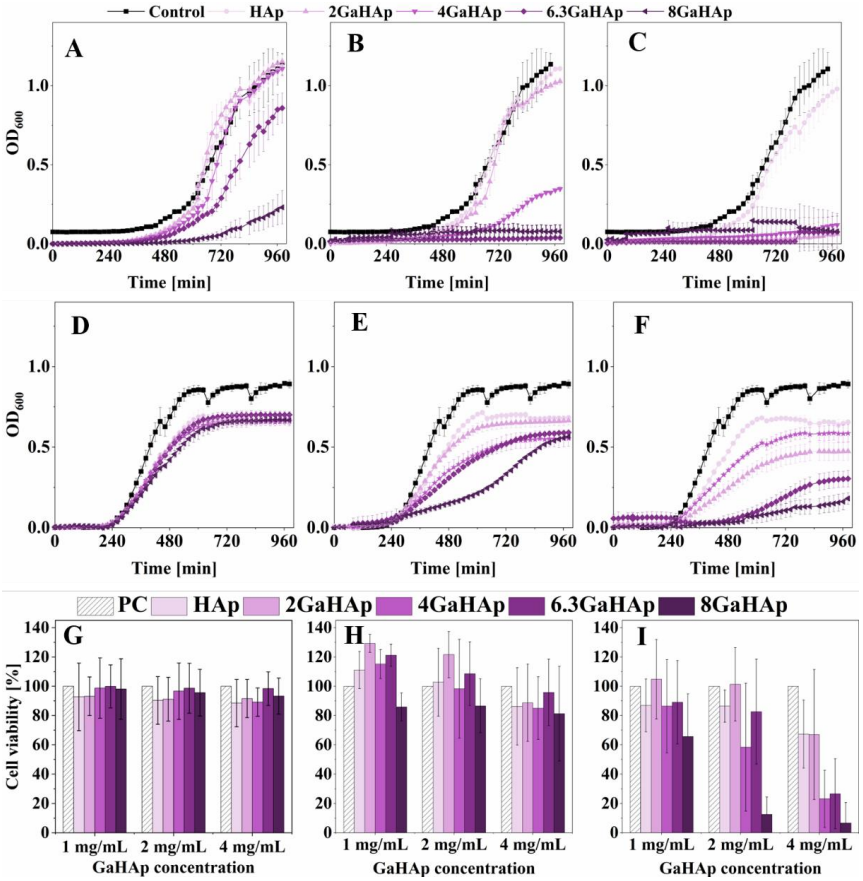

Fig. 8. The GaHAp powder suspension induced growth inhibition of *P. aeruginosa* at concentrations of: A – 1 mg/mL, B – 2 mg/mL, C – 4 mg/mL, and *S. aureus* at concentrations of: D – 1 mg/mL, E – 2 mg/mL, F – 4 mg/mL. Metabolic activity of human fibroblasts (hTERT-BJ1) exposed to the GaHAp powder suspensions at different concentrations (1 mg/mL, 2 mg/mL, and 4 mg/mL) obtained using the direct test: G – day 1, H – day 3, and C – day 7 (PC – positive control).

The bacterial growth kinetics in the GaHAp powders' suspensions at concentrations of 1 mg/mL, 2 mg/mL, and 4 mg/mL were investigated in TSB. Cytotoxicity of the GaHAp powders was tested on telomerase-immortalised human foreskin fibroblasts (hTERT BJ1) cultivated in DMEM via direct tests of the GaHAp powders (at concentrations of 1 mg/mL, 2 mg/mL, and 4 mg/mL in DMEM) and indirect tests of the GaHAp pastes (250 ± 50 mg) up to 7 days [82].

The GaHAp powders exhibited bacteriostatic effect against all five tested bacteria; however, the most pronounced inhibition was observed against *P. aeruginosa* (Fig. 8 A–C), as *P. aeruginosa* has an iron-dependent metabolism, which is disrupted by Ga^{3+} ions [51].

The *P. aeruginosa* growth inhibition was observed at 1 mg/mL concentration for the 6.3GaHAp and 8GaHAp powders, which was not observed for *S. aureus* (Fig. 8 D–F). Whereas inhibition of orthopaedic infection-related bacteria, *S. aureus* and *S. epidermidis*, was detected at 2 mg/mL and 4 mg/mL concentrations of the 4GaHAp, 6.3GaHAp, and 8GaHAp powders. Notably, this bacterial inhibition occurred at higher GaHAp powder concentrations than reported in the literature. For instance, Kurtjak et al. observed inhibition of *P. aeruginosa* growth with 0.9 g/mL GaHAp containing 3 wt% of Ga [54]. In addition, Ballardini et al. showed the antibacterial effect of the GaHAp with Ga content 1 wt%, where bacterial reduction of *P. aeruginosa* and *S. aureus* after 24 h was above 80 % [83]. Even though in all the mentioned studies, the analysed substance was GaHAp, the findings indicate that the synthesis method and parameters significantly influences the incorporation of Ga and key properties of the final material.

To evaluate cytotoxicity, hTERT-BJ1 fibroblast cells were directly exposed to the GaHAp powder suspensions in DMEM at the same concentrations as in the antibacterial tests (1 mg/mL, 2 mg/mL, and 4 mg/mL) (Fig. 8 G–I). After three days, metabolic activity remained above 80 %. However, by day 7, cell viability sharply reduced below 40 % for all the Ga-containing samples at 2 mg/mL and 4 mg/mL, highlighting the importance of optimising Ga^{3+} concentration for biocompatibility. The indirect tests assessed the impact of ions released from the GaHAp paste into the cell media on the chosen cell line (Fig. 9 A).

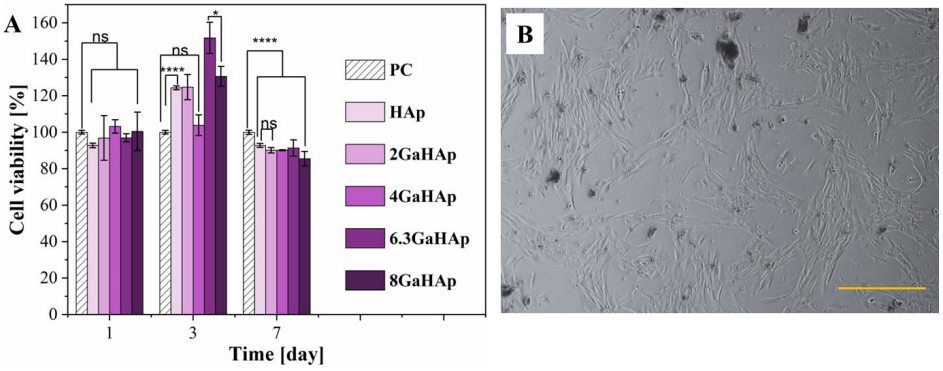

Fig. 9. A – Metabolic activity of human fibroblasts exposed to the GaHAp pastes via indirect test; B – microscope images of human fibroblasts after the indirect test on day 3. Scale bar 200 μm.

Results indicated no cytotoxic effects, as cell viability remained around 90 %. Notably, samples with Ga content of 5.5 ± 0.1 wt% and 6.9 ± 0.5 wt% significantly enhanced metabolic activity on day 3 and day 7, suggesting that both Ga^{3+} and Ca^{2+} ions have a stimulatory effect on the cells.

The results of the research show the importance of evaluating the influence of Ga on the as-synthesised HAp and the interactions between the developed biomaterial and cells. Obtained GaHAp powders showed advantageous properties for the early-stage treatment of bone defects compared to the studied GaACP powders. Moreover, regarding the toxicity evaluation of the GaHAp powders, an adverse effect towards human fibroblasts was not observed. It was concluded that the GaHAp could prevent the development of chronic and acute infections due to the bacteriostatic effect on both gram-positive and gram-negative bacterial species. Accordingly, in the next study, the bioceramics were developed using the 2GaHAp (1.6 ± 0.1 wt% of Ga) and 4GaHAp (3.3 ± 0.4 wt% of Ga) powders. The compositions were chosen since the respective Ga concentrations provided both antibacterial activity and did not show a toxic effect on the cells.

GaHAp Bioceramics (Paper 4)

GaHAp bioceramics were prepared by uniaxially compacting the as-synthesised GaHAp precursor powders at 100 MPa for 1 min, followed by high-temperature sintering in the range from 600 °C to 1200 °C. The phase composition and the theoretical Ga substitution position in the HAp structure of heat-treated powders were analysed using XRD and Rietveld refinement by *Profex* software. The apparent density of the sintered bioceramics was determined using Archimedes principle and a density determination kit (*YDK 01*, *Sartorius AG*, Germany). The microstructure of the bioceramics was characterised using SEM.

Phase composition analysis revealed the formation of a secondary α-TCP phase above 800 °C (Fig. 10 A–C). The content of the secondary phase increased with increasing Ga concentration (Fig. 10 D).

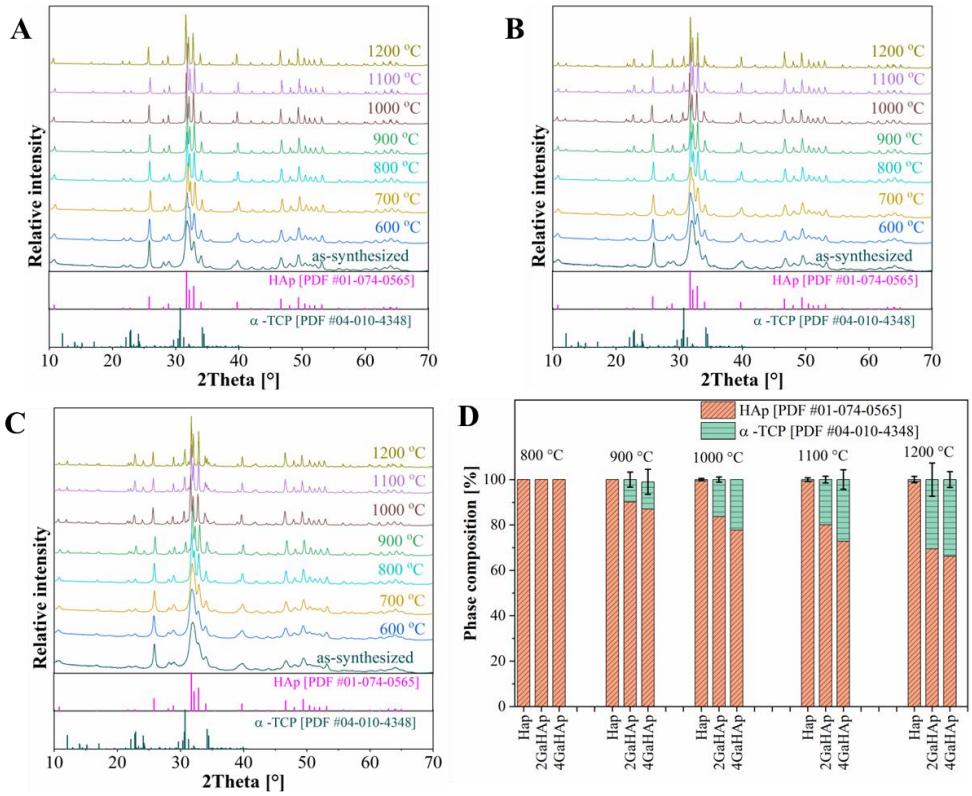

Fig. 10. XRD patterns of the heat-treated A – HAp, B – 2GaHAp, and C – 4GaHAp powders. D – Phase compositions of the samples.

As discussed previously, the as-synthesised powders were CDHAp with Ca/P < 1.67 and with the impurities of an amorphous phase. A combination of these two main characteristics of precursor powder leads to the formation of low-temperature α-TCP at ≥ 900 °C, even though the stability of α-TCP is reported to be in the range of 1120–1430 °C [84], [85]. The presence of the secondary phase (α-TCP) can potentially improve the biodegradability of HAp

bioceramics. Namely, the presence of more soluble α-TCP phase could increase the solubility of the bioceramics, providing improved ion release and bioactivity [42].

The ATR-FTIR spectra (Fig. 11 A–C) exhibited characteristic CaPs' PO_4^{3-}, OH^-, CO_3^{2-}, and HPO_4^{2-} groups' absorbance bands.

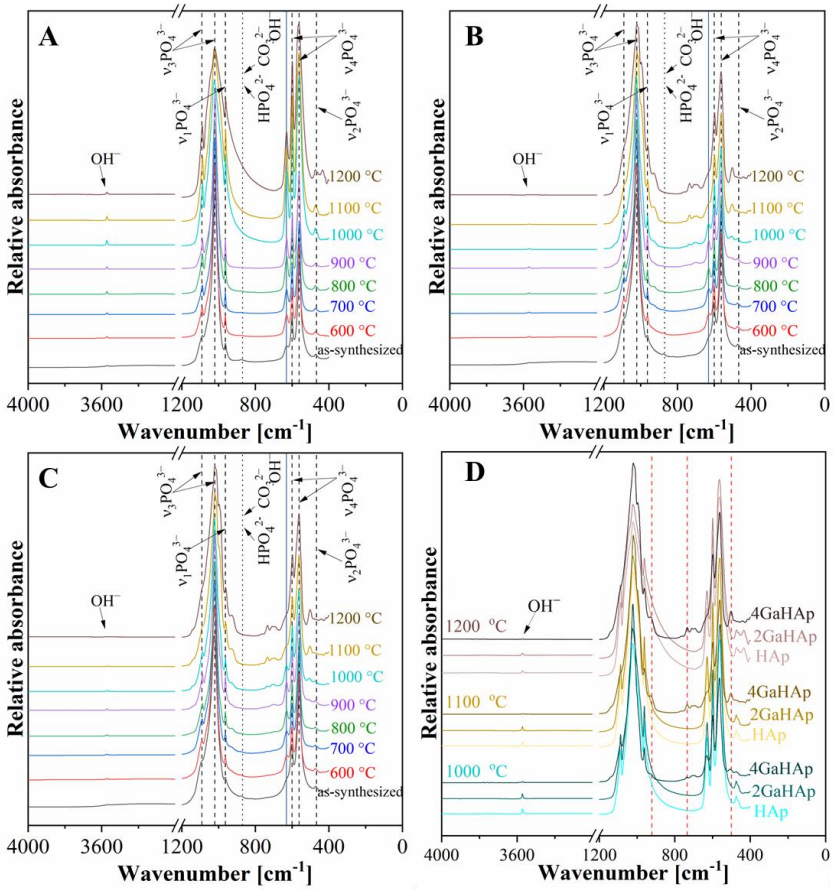

Fig. 11. ATR-FTIR spectra of A – HAp, B – 2GaHAp, and C – 4GaHAp powders heat-treated at temperatures ranging from 600 °C to 1200 ºC. D – extra functional group maxima (marked with red lines) for samples heat-treated at 1000 °C, 1100 °C and 1200 ºC.

Due to cationic deficiency, charge compensation was maintained by substituting HPO_4^{2-} for PO_4^{3-}. Absorbance bands of CO_3^{2-} and HPO_4^{2-} disappeared after heat treatment [87]. Furthermore, a decrease in the absorbance of OH^- groups approximately at 3600 cm^{-1} was observed, which is related to the presence of the secondary phase. The presence of secondary phase also affected PO_4^{3-} groups after heat treatment at 900–1000 °C. Additional absorbance bands were detected as "shoulders", which became more pronounced as the heat treatment temperature increased. In the case of 2GaHAp and 4GaHAp powders heat-treated above 1000 °C, extra absorbance bands at 502 cm^{-1}, 734 cm^{-1}, and 928 cm^{-1} were detected, and the intensity of these bands increased with increasing Ga content. It is difficult to reach definitive

conclusions about forming new functional groups due to the overlapping of the absorbance bands from various phases and impurities in the same spectral area. However, the identified absorbance bands could be related to the potential development of Ga-O bonds. According to existing literature, Ga_2O_3 heat-treated at 1000 °C exhibits bands (duplicates) within the 400–850 cm^{-1} range [46], which aligns with the area indicating the formation of the detected new groups.

Theoretical Ga substitution in the HAp crystal lattice

To locate Ga substitution in the HAp crystal lattice and observe lattice changes prompted by substitution, a complete structure Rietveld refinement of the sample was performed. From the refinement results, the refined unit cell volume of the HAp and GaHAp heat-treated at 1000 °C, 1100 °C, and 1200 °C was calculated and displayed in Fig. 12 A. The results showed that the unit cell volumes of HAp increased with increasing Ga content, suggesting that Ga^{3+} ions are incorporated into the HAp crystal lattice.

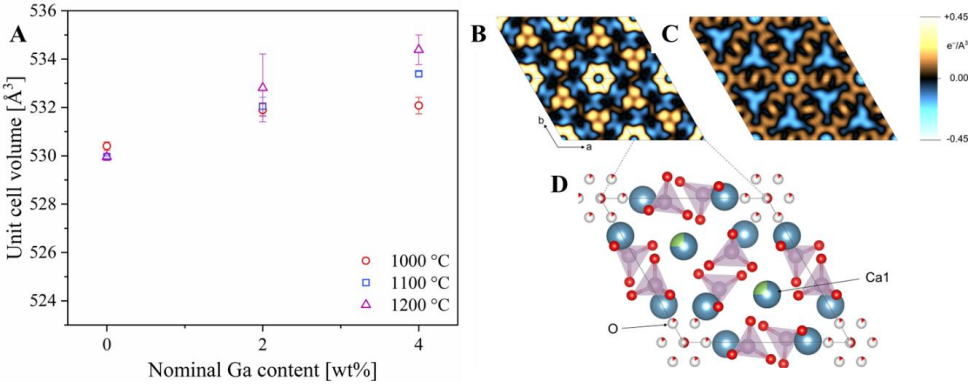

Fig. 12. A – Refined unit cell volume of the HAp and GaHAp heat-treated at 1000 °C, 1100 °C, and 1200 °C as a function of the nominal Ga concentration; F_{obs}–F_{calc} Fourier synthesis maps at z = 0.0 of the 4GaHAp heat-treated at 1100 °C refined B – without and C – with the substitution model for Ga. The model is depicted schematically in D – "O" marks the additional oxygen ion compensating the charge imbalance introduced by Ga incorporation on "Ca1".

The theoretical substitution model was created based on the full structural refinement of the 4GaHAp heat-treated at 1100 °C, including refinement of Ca site occupancy factors, fractional coordinates, and thermal displacement parameters. Firstly, different Fourier maps of the refined structure were created with the Electron Density Map module in *Profex*. Structure refinement of the hexagonal HAp phase in the dataset 4GaHAp heat-treated at 1100 °C with a Ga-free hexagonal structure model, showed residual unfitted electron densities at the Ca1 position (Fig. 12 B). In addition, along the *c*-axis hosting the OH^- groups, formation of the excess electron densities in the form of a hexagonal "flower" was observed (Fig. 12 B). By suggesting and creating a structural model where Ca1 was a partial substitution for Ga^{3+} and charge imbalance was compensated by an additional O^{2-} ion in the OH^- channels, the F_{obs}–F_{calc} Fourier synthesis maps revealed no excess or residual electrons, and the structure remained neutral

(Fig. 12 C). This explains the expansion of the crystalline unit cell volume, where additional incorporation of oxygen ions in the channel compensates for the additional positive charge introduced by Ga^{3+} substitution in the Ca1 site. The substitution model reveals the formation of a defect in the lattice that further affects the microstructure of the bioceramic.

Microstructure of GaHAp bioceramics

Lattice structural and phase composition changes induced by Ga incorporation significantly influenced HAp bioceramics' sinterability, causing a notable decrease in apparent density (Fig. 13 A) and the shrinkage (Fig. 13 B). Additionally, SEM micrographs (Fig. 14 A–I) showed micropore formation, as a formation of secondary phase occurred during sintering, which inhibits densification of bioceramics. It can be explained by the effect of secondary phase particles on grain boundary motion, as at intermediate temperatures during the sintering process, CDHAp converts to α-TCP, which limits grain boundary motion. At the same time, HAp continues to function as the matrix, and secondary phases generate dispersed particles at the grain boundaries that hinder grain growth [88].

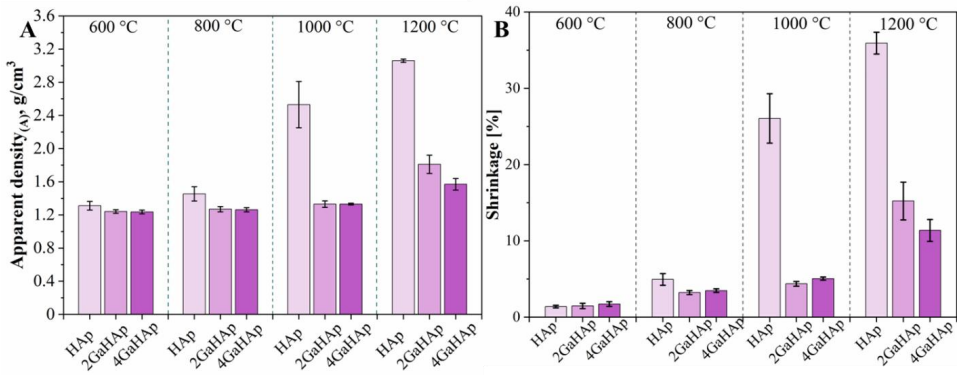

Fig. 13. A – Apparent density and B – shrinkage of the HAp and GaHAp bioceramics after sintering at 600 °C, 800 °C, 1000 °C, and 1200 °C.

SEM micrographs revealed that increasing the sintering temperature led to increased grain sizes. Ga incorporation promoted the formation of smaller grains. In the case of the HAp bioceramics, characteristic hexagonal grains formed above 1000 ºC (Fig. 14 G, J, M). However, for the GaHAp bioceramics, formation of characteristic hexagonal grains was observed at a 1200 ºC sintering temperature.

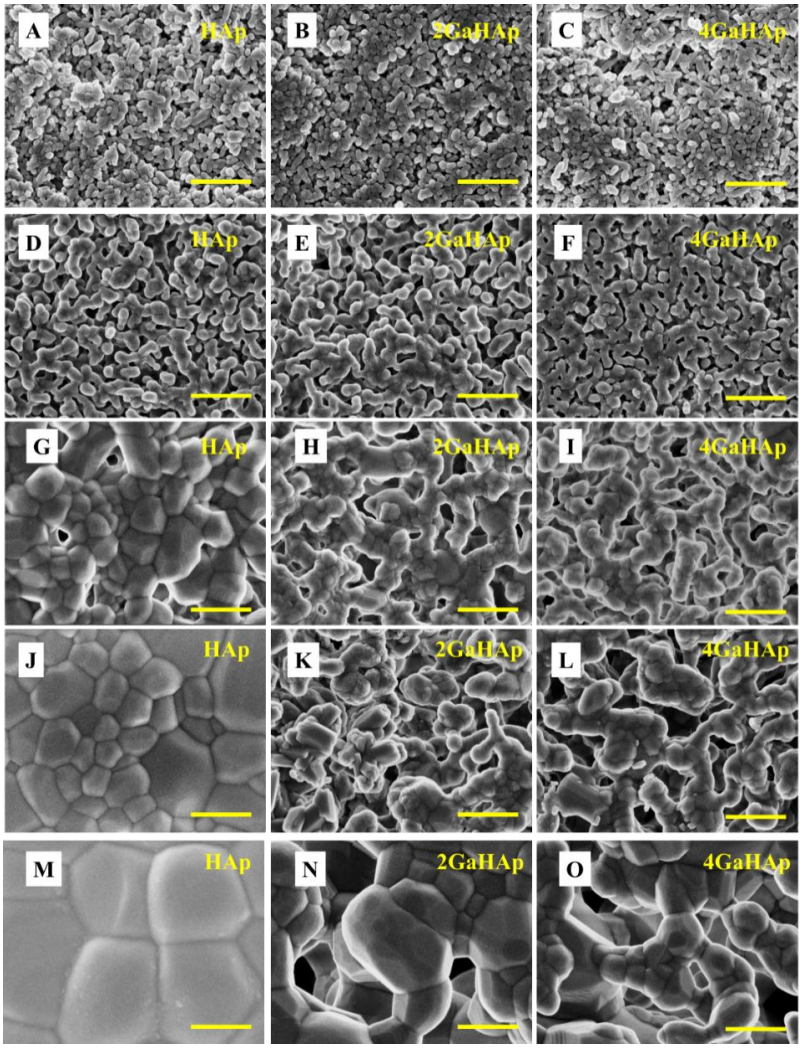

Fig. 14. SEM microphotographs of the A – HAp, B – 2GaHAp, and C – 4GaHAp bioceramic pellets sintered at 600 ^{o}C, the D – HAp, E – 2GaHAp, F – 4GaHAp bioceramic pellets sintered at 800 ^{o}C, the G – HAp, H – 2GaHAp, and I – 4GaHAp bioceramic pellets sintered at 1000 ^{o}C, the J – HAp, K – 2GaHAp, L– 4GaHAp bioceramic pellets sintered at 1100 ^{o}C, and the M – HAp, N – 2GaHAp, and O – 4GaHAp bioceramic pellets sintered at 1200 ^{o}C. Scale bar – 500 nm [89].

The in-depth substitution behaviour of Ga in the HAp crystal lattice was explored to gain deeper insight into the properties of GaHAp bioceramics. The results demonstrated that partial Ca substitution with Ga can significantly change the HAp thermal behaviour.

CONCLUSIONS

1. Incorporation of gallium in amorphous calcium phosphate is limited to 2.2 ± 0.1 wt% and does not have a significant effect on its physicochemical properties. However, gallium improves the stability of amorphous calcium phosphate in deionised H_2O and in biologically relevant media, i.e., Dulbecco's modified Eagle's medium and tryptic soy broth.
2. Amorphous calcium phosphate and gallium-containing amorphous calcium phosphate powders at a concentration of 4 mg/mL show bacteriostatic effect against *Pseudomonas aeruginosa* and *Staphylococcus aureus*.
3. Gallium inhibits the crystal growth of hydroxyapatite, resulting in a decrease in crystallinity and the formation of smaller particles. The low-crystalline gallium-containing hydroxyapatite provides long-term gallium ion release up to 28 days.
4. The optimal gallium content in hydroxyapatite is in the range from 2 wt% to 5.5 ± 0.1 wt%, providing bacteriostatic effect against *Pseudomonas aeruginosa* and *Staphylococcus aureus* without substantial toxicity towards human fibroblasts.
5. The addition of gallium affects the physicochemical properties of hydroxyapatite precursor powders, leading to the formation of biphasic bioceramics consisting of hydroxyapatite and tricalcium phosphate after heat treatment of hydroxyapatite at temperatures above 900 °C. The secondary phase and lattice defects promote the formation of a microporous structure of the bioceramics and decrease shrinkage.
6. Gallium in the hydroxyapatite crystal lattice occupies the Ca1 position and creates vacancies in the OH^- channels. Charge compensation is achieved by an uptake of O^-, which leads to unit cell volume expansion.

REFERENCES

1. J. M. Wallace, Skeletal Hard Tissue Biomechanics. In D. B. Burr, M. R. Allen, editors. Basic and Applied Bone Biology. Academic Press; 2019, 125–140. https://doi.org/10.1016/B978-0-12-813259-3.00007-5.

2. D. L. Stocum, Regeneration of Musculoskeletal Tissues. In D. L. Stocum, editor. Regenerative Biology and Medicine. Academic Press, 2012, 127–160. https://doi.org/10.1016/B978-0-12-384860-4.00006-X.

3. W. Jiang, H. Liu, Nanocomposites for bone repair and osteointegration with soft tissues. In H. Lui, editor. Nanocomposites for Musculoskeletal Tissue Regeneration. Woodhead Publishing, 2016, 241–257. https://doi.org/10.1016/B978-1-78242-452-9.00011-X.

4. A. H. Hoveidaei, M. Sadat-Shojai, S. Mosalamiaghili, S. R. Salarikia, H. Roghani-shahraki, R. Ghaderpanah, M. H. Ersi, J. D. Conway, Nano-hydroxyapatite structures for bone regenerative medicine: Cell-material interaction. Bone. 179 (2024) 116956. https://doi.org/10.1016/j.bone.2023.116956.

5. I. Roohani, S. Cheong, A. Wang, How to build a bone? – Hydroxyapatite or Posner's clusters as bone minerals. Open Ceramics. 6 (2021) 100092. https://doi.org/10.1016/J.OCERAM.2021.100092.

6. A. Lotsari, A. K. Rajasekharan, M. Halvarsson, M. Andersson, Transformation of amorphous calcium phosphate to bone-like apatite. Nat. Commun. 9 (2018) 4170. https://doi.org/10.1038/s41467-018-06570-x.

7. F. Nudelman, P. H. H. Bomans, A. George, G. de With, N. A. J. M. Sommerdijk, The role of the amorphous phase on the biomimetic mineralization of collagen, Faraday Discuss. 159 (2012) 357-370. https://doi.org/10.1039/c2fd20062g.

8. S. T. J. Tsang, A. J. van Rensburg, J. van Heerden, G. Z. Epstein, R. Venter, N. Ferreira, The management of critical bone defects: outcomes of a systematic approach, European Journal of Orthopaedic Surgery and Traumatology. 34 (2024) 3225–3231. https://doi.org/10.1007/S00590-024-04050-1.

9. A. Díaz-Cuenca, D. Rabadjieva, K. Sezanova, R. Gergulova, R. Ilieva, S. Tepavitcharova, Biocompatible calcium phosphate-based ceramics and composites, Mater Today Proc. 61 (2022) 1217–1225. https://doi.org/10.1016/J.MATPR.2022.01.329.

10. M. C. Schulz, S. Holtzhausen, B. Nies, S. Heinemann, D. Muallah, L. Kroschwald, K. Paetzold-Byhain, G. Lauer, P. Sembdner, Three-Dimensional Plotted Calcium Phosphate Scaffolds for Bone Defect Augmentation – A New Method for Regeneration, Journal of Personalized Medicine. (2023) 13(3) 464. https://doi.org/10.3390/JPM13030464.

11. A. B. G. de Carvalho, M. Rahimnejad, R. L. M. S. Oliveira, P. Sikder, G. S. F. A. Saavedra, S. B. Bhaduri, D. Gawlitta, J. Malda, D. Kaigler, E. S. Trichês, M. C. Bottino, Personalized bioceramic grafts for craniomaxillofacial bone regeneration, International Journal of Oral Science 16 (2024) 63. https://doi.org/10.1038/s41368-024-00327-7.

12. M. Bohner, Resorbable biomaterials as bone graft substitutes, Materials Today. 13(1–2) (2010) 24–30. https://doi.org/10.1016/S1369-7021(10)70014-6.

13. M. Bohner, Calcium orthophosphates in medicine: from ceramics to calcium phosphate cements, Injury. 31 (2000) D37–D47. https://doi.org/10.1016/S0020-1383(00)80022-4.

14. T. Lu, L. Zhang, X. Yuan, J. Ye, A novel calcium phosphate-based ceramic scaffolds with unexpected high osteogenic activity by strontium doping, Mater Today Chem. 36 (2024) 101931. https://doi.org/10.1016/J.MTCHEM.2024.101931.

15. J. A. da Cruz, R. R. Pezarini, A. J. M. Sales, S. R. Benjamin, P. M. de Oliveira Silva, M. P. F. Graça, Study of biphasic calcium phosphate (BCP) ceramics of tilapia fish bones by age, Spectrochim., Acta A Mol. Biomol. Spectrosc. 316 (2024) 124289. https://doi.org/10.1016/J.SAA.2024.124289.

16. A. K. Rajendran, M. S. J. Anthraper, N. S. Hwang, J. Rangasamy, Osteogenesis and angiogenesis promoting bioactive ceramics, Materials Science and Engineering: R: Reports. 159 (2024) 100801. https://doi.org/10.1016/J.MSER.2024.100801.

17. V. I. dos Santos, J. Chevalier, M. C. Fredel, B. Henriques, L. Gremillard, Ceramics and ceramic composites for biomedical engineering applications via Direct Ink Writing: Overall scenario, advances in the improvement of mechanical and biological properties and innovations, Materials Science and Engineering: R: Reports. 161 (2024) 100841. https://doi.org/10.1016/J.MSER.2024.100841.

18. C. Liu, C. Shao, L. Zhang, Q. Huang, Biomaterials and MSCs composites in regenerative medicine, Mesenchymal Stem Cells: Biological Concepts, Current Advances, Opportunities and Challenges. (2023) 69–99. https://doi.org/10.1016/B978-0-323-95346-7.00004-X.

19. S. Thomas, B. S. P. Harshita, P. Mishra, S. Talegaonkar, Ceramic Nanoparticles: Fabrication Methods and Applications in Drug Delivery, Curr. Pharm. Des. 21(42) (2015) 6165–6188. https://doi.org/10.2174/1381612821666151027153246.

20. S. V. Dorozhkin, Synthetic amorphous calcium phosphates (ACPs): preparation, structure, properties, and biomedical applications, Biomater. Sci. 9 (2021) 7748–7798. https://doi.org/10.1039/D1BM01239H.

21. X. Hou, L. Zhang, Z. Zhou, X. Luo, T. Wang, X. Zhao, B. Lu, F. Chen, L. Zheng, Calcium Phosphate-Based Biomaterials for Bone Repair, Journal of Functional Biomaterials. 13 (2022) 187. https://doi.org/10.3390/JFB13040187.

22. C. Combes, C. Rey, Amorphous calcium phosphates: Synthesis, properties and uses in biomaterials, Acta Biomater. 6(9) (2010) 3362–3378. https://doi.org/10.1016/j.actbio.2010.02.017.

23. E. Eanes, Amorphous Calcium Phosphate, in: Octacalcium Phosphate, (2001) 130–147. https://doi.org/10.1159/000061652.

24. M. Vallet-Regí, D. Lozano, B. González, I. Izquierdo-Barba, Biomaterials against Bone Infection, Adv. Healthc. Mater. 9(13) (2020). https://doi.org/10.1002/adhm.202000310.

25. H. Tabaja, O. M. Abu Saleh, D. R. Osmon, Periprosthetic Joint Infection: What's New? Infect. Dis. Clin. North. Am. 38(4) (2024) 731–756. https://doi.org/10.1016/J.IDC.2024.07.007.

26. L. Pulido, E. Ghanem, A. Joshi, J. J. Purtill, J. Parvizi, Periprosthetic Joint Infection: The Incidence, Timing, and Predisposing Factors, Clin. Orthop. Relat. Res. 466(7) (2008) 1710–1715. https://doi.org/10.1007/S11999-008-0209-4.

27. V. Boddapati, M. C. Fu, D. J. Mayman, E. P. Su, P. K. Sculco, A. S. McLawhorn, Revision Total Knee Arthroplasty for Periprosthetic Joint Infection Is Associated with Increased Postoperative Morbidity and Mortality Relative to Noninfectious Revisions, J. Arthroplasty. 33(2) (2018) 521–526. https://doi.org/10.1016/J.ARTH.2017.09.021.

28. F. Der Wang, Y. P. Wang, C. F. Chen, H. P. Chen, The incidence rate, trend and microbiological aetiology of prosthetic joint infection after total knee arthroplasty: A 13 years' experience from a tertiary medical center in Taiwan, Journal of Microbiology, Immunology and Infection. 51(6) (2018) 717–722. https://doi.org/10.1016/J.JMII.2018.08.011.

29. O. F. Egerci, A. Yapar, F. Dogruoz, H. Selcuk, O. Kose, Preventive strategies to reduce the rate of periprosthetic infections in total joint arthroplasty; a comprehensive review, Archives of Orthopaedic and Trauma Surgery. 144 (2024) 5131–5146. https://doi.org/10.1007/S00402-024-05301-W.

30. M. Riool, S. A. J. Zaat, Biomaterial-Associated Infection: Pathogenesis and Prevention, In: Soria, F., Rako, D., de Graaf, P. (eds) Urinary Stents. Springer (2022) 245–257. https://doi.org/10.1007/978-3-031-04484-7_20.

31. D. Y. Wang, L. Su, K. Poelstra, D. W. Grainger, H. C. van der Mei, L. Shi, H. J. Busscher, Beyond surface modification strategies to control infections associated with implanted biomaterials and devices – Addressing the opportunities offered by nanotechnology, Biomaterials. 308 (2024) 122576. https://doi.org/10.1016/J.BIOMATERIALS.2024.122576.

32. J. Barros, F. J. Monteiro, M. P. Ferraz, Bioengineering Approaches to Fight against Orthopedic Biomaterials Related-Infections, Int. J. Mol. Sci. 23(19) (2022) 11658. https://doi.org/10.3390/ijms231911658.

33. W. Shuaishuai, Z. Tongtong, W. Dapeng, Z. Mingran, W. Xukai, Y. Yue, D. Hengliang, W. Guangzhi, Z. Minglei, Implantable biomedical materials for treatment of bone infection, Front. Bioeng. Biotechnol. 11 (2023). https://doi.org/10.3389/fbioe.2023.1081446.

34. M. Cerioli, C. Batailler, A. Conrad, S. Roux, T. Perpoint, A. Becker, C. Triffault-Fillit, S. Lustig, M.-H. Fessy, F. Laurent, F. Valour, C. Chidiac, T. Ferry, Pseudomonas aeruginosa Implant-Associated Bone and Joint Infections: Experience in a Regional Reference Center in France, Front Med. 7 (2020). https://doi.org/10.3389/fmed.2020.513242.

35. A. Frei, A. D. Verderosa, A. G. Elliott, J. Zuegg, M. A. T. Blaskovich, Metals to combat antimicrobial resistance, Nature Reviews Chemistry. 7 (2023) 202–224. https://doi.org/10.1038/s41570-023-00463-4.

36. M. Godoy-Gallardo, U. Eckhard, L. M. Delgado, Y. J. D. de Roo Puente, M. Hoyos-Nogués, F. J. Gil, R. A. Perez, Antibacterial approaches in tissue engineering using metal ions and nanoparticles: From mechanisms to applications, Bioact. Mater. 6(12) (2021) 4470. https://doi.org/10.1016/J.BIOACTMAT.2021.04.033.

37. J. A. Lemire, J. J. Harrison, R. J. Turner, Antimicrobial activity of metals: Mechanisms, molecular targets and applications, Nat. Rev. Microbiol. 11 (2013) 371–384. https://doi.org/10.1038/nrmicro3028.

38. S. Mittapally, R. Taranum, S. Parveen, Metal ions as antibacterial agents, Journal of Drug Delivery and Therapeutics. 8(6) (2018) 411–419. https://doi.org/10.22270/JDDT.V8I6-S.2063.

39. M. A. Zoroddu, J. Aaseth, G. Crisponi, S. Medici, M. Peana, V. M. Nurchi, The essential metals for humans: a brief overview, J. Inorg. 195 (2019) 120–129. https://doi.org/10.1016/j.jinorgbio.2019.03.013.

40. A. B. Kelson, M. Carnevali, V. Truong-Le, Gallium-based anti-infectives: Targeting microbial iron-uptake mechanisms, Curr. Opin. Pharmacol. 5(13) (2013) 707–716. https://doi.org/10.1016/j.coph.2013.07.001.

41. F. Kurtuldu, N. Mutlu, A. R. Boccaccini, D. Galusek, Gallium containing bioactive materials: A review of anticancer, antibacterial, and osteogenic properties, Bioact. Mater. 17 (2022) 125–146. https://doi.org/10.1016/j.bioactmat.2021.12.034.

42. V. Vitali, S. Zineddu, L. Messori, Metal compounds as antimicrobial agents: ‘smart’ approaches for discovering new effective treatments, RSC Adv. 15 (2025) 748–753. https://doi.org/10.1039/D4RA07449A.

43. P. Collery, B. Keppler, C. Madoulet, B. Desoize, Gallium in cancer treatment, Crit. Rev. Oncol. Hematol. 42(3) (2002) 283–296. https://doi.org/10.1016/S1040-8428(01)00225-6.

44. V. de A. W. Sales, T. R. R. Timóteo, N. M. da Silva, C. G. de Melo, A. S. Ferreira, M. V. G. de Oliveira, E. de O. Silva, L. M. dos S. Mendes, L. A. Rolim, P. J. R. Neto, A Systematic Review of the Anti-inflammatory Effects of Gallium Compounds, Curr. Med. Chem. 28(10) (2020) 2062–2076. https://doi.org/10.2174/0929867327666200525160556.

45. W. Sun, M. Qi, S. Cheng, C. Li, B. Dong, L. Wang, Gallium and gallium compounds: New insights into the “Trojan horse” strategy in medical applications, Mater. Des. 227 (2023) 111704. https://doi.org/10.1016/J.MATDES.2023.111704.

46. F. Li, F. Liu, K. Huang, S. Yang, Advancement of Gallium and Gallium-Based Compounds as Antimicrobial Agents, Front. Bioeng. Biotechnol. 10 (2022) 827960. https://doi.org/10.3389/FBIOE.2022.827960.

47. F. Shi, S. S. Ma, S. Liu, R. Xin, B. Chen, W. Ye, J. Sun, A novel antimicrobial strategy for bacterial infections: Gallium-based materials, Colloid Interface Sci. Commun. 56 (2023) 100735. https://doi.org/10.1016/J.COLCOM.2023.100735.

48. B. R. Wilson, A. R. Bogdan, M. Miyazawa, K. Hashimoto, Y. Tsuji, Siderophores in Iron Metabolism: From Mechanism to Therapy Potential, Trends Mol Med. 22(12) (2016) 1077–1090. https://doi.org/10.1016/j.molmed.2016.10.005.

49. N. Kircheva, T. Dudev, Gallium as an Antibacterial Agent: A DFT/SMD Study of the Ga3+/Fe3+ Competition for Binding Bacterial Siderophores, Inorg. Chem. 59(9) (2020) 6242–6254. https://doi.org/10.1021/acs.inorgchem.0c00367.

50. A. Müller, C. Fessele, F. Zuber, M. Rottmar, K. Maniura-Weber, Q. Ren, A. G. Guex, Gallium Complex-Functionalized P4HB Fibers: A Trojan Horse to Fight Bacterial Infection, ACS Appl. Bio. Mater. 4(1) (2021) 682–691. https://doi.org/10.1021/acsabm.0c01221.

51. F. Minandri, C. Bonchi, E. Frangipani, F. Imperi, P. Visca, Promises and failures of gallium as an antibacterial agent, Future Microbiol. 9(3) (2014) 379–397. https://doi.org/10.2217/fmb.14.3.

52. M. Mosina, I. Kovrlija, L. Stipniece, J. Locs, Gallium containing calcium phosphates: Potential antibacterial agents or fictitious truth, Acta Biomater. 150 (2022) 48–57. https://doi.org/10.1016/j.actbio.2022.07.063.

53. M. Yang, J. Ren, R. Zhang, Novel gallium-doped amorphous calcium phosphate nanoparticles: Preparation, application and structure study, J. Non-Cryst. Solids. 466–467 (2017) 15–20. https://doi.org/10.1016/j.jnoncrysol.2017.03.034.

54. M. Kurtjak, M. Vukomanović, A. Krajnc, L. Kramer, B. Turk, D. Suvorov, Designing Ga(III)-containing hydroxyapatite with antibacterial activity, RSC Adv. 6 (2016) 112839–112852. https://doi.org/10.1039/c6ra23424k.

55. K. Pajor, Ł. Pajchel, A. Zgadzaj, U. Piotrowska, J. Kolmas, Modifications of hydroxyapatite by gallium and silver ions—physicochemical characterization, cytotoxicity and antibacterial evaluation, Int. J. Mol. Sci. 21(14) (2020) 5006. https://doi.org/10.3390/ijms21145006.

56. M. Kurtjak, M. Vukomanović, D. Suvorov, Antibacterial nanocomposite of functionalized nanogold and gallium-doped hydroxyapatite, Mater. Lett. 193 (2017) 126–129. https://doi.org/10.1016/j.matlet.2017.01.092.

57. C. Combes, C. Rey, Amorphous calcium phosphates: Synthesis, properties and uses in biomaterials, Acta Biomater. 6(9) (2010) 3362–3378. https://doi.org/https://doi.org/10.1016/j.actbio.2010.02.017.

58. S. V. Dorozhkin, Synthetic amorphous calcium phosphates (ACPs): Preparation, structure, properties, and biomedical applications, Biomater. Sci. 9 (2021) 7748–7798. https://doi.org/https://doi.org/10.1039/d1bm01239h.

59. M. Mosina, J. Locs, Synthesis of Amorphous Calcium Phosphate: A Review, Key Eng. Mater. 850 (2020) 199–206. https://doi.org/10.4028/www.scientific.net/KEM.850.199.

60. J. Vecstaudza, J. Locs, Novel preparation route of stable amorphous calcium phosphate nanoparticles with high specific surface area, J. Alloys Compd. 700 (2017) 215–222. https://doi.org/http://dx.doi.org/10.1016/j.jallcom.2017.01.038.

61. G. Mancardi, C. E. Hernandez Tamargo, D. Di Tommaso, N. H. De Leeuw, Detection of Posner's clusters during calcium phosphate nucleation: a molecular dynamics study, J. Mater. Chem. B. 5 (2017) 7274–7284. https://doi.org/10.1039/C7TB01199G.

62. S. Somrani, C. Rey, M. Jemal, Thermal evolution of amorphous tricalcium phosphate, J. Mater. Chem. 13 (2003) 888–892. https://doi.org/10.1039/B210900J.

63. L. Degli Esposti, M. Fosca, A. Canizares, L. Del Campo, M. Ortenzi, A. Adamiano, J. V. Rau, M. Iafisco, An in situ study of thermal crystallization of amorphous calcium phosphates, Physical Chemistry Chemical Physics. 24 (2022) 24514–24523. https://doi.org/10.1039/D2CP02352K.

64. L. Degli Esposti, S. Markovic, N. Ignjatovic, S. Panseri, M. Montesi, A. Adamiano, M. Fosca, J. V. Rau, V. Uskoković, M. Iafisco, Thermal crystallization of amorphous calcium phosphate combined with citrate and fluoride doping: a novel route to produce hydroxyapatite bioceramics, J. Mater. Chem. B. 9 (2021) 4832–4845. https://doi.org/10.1039/D1TB00601K.

65. Z. Z. Zyman, A. V. Goncharenko, D. V. Rokhmistrov, Phase evolution during heat treatment of amorphous calcium phosphate derived from fast nitrate synthesis, Processing and Application of Ceramics. 11(2) (2017) 147–153. https://doi.org/10.2298/PAC1702147Z.

66. J. Vecstaudza, M. Gasik, J. Locs, Amorphous calcium phosphate materials: Formation, structure and thermal behaviour, J. Eur. Ceram. Soc. 39(4) (2019) 1642–1649. https://doi.org/10.1016/J.JEURCERAMSOC.2018.11.003.

67. W. Jin, S. Jiang, H. Pan, R. Tang, Amorphous Phase Mediated Crystallization: Fundamentals of Biomineralization, Crystals. 8(1) (2018) 48. https://doi.org/10.3390/CRYST8010048.

68. E. D. Eanes, J. D. Termine, M. U. Nylen, An electron microscopic study of the formation of amorphous calcium phosphate and its transformation to crystalline apatite, Calcif Tissue Res. 12 (1973) 143–158. https://doi.org/10.1007/BF02013730.

69. B. Jin, Z. Liu, C. Shao, J. Chen, L. Liu, R. Tang, J. J. De Yoreo, Phase Transformation Mechanism of Amorphous Calcium Phosphate to Hydroxyapatite Investigated by Liquid-Cell Transmission Electron Microscopy, Cryst. Growth Des. 21(9) (2021) 5126–5134. https://doi.org/10.1021/acs.cgd.1c00503.

70. K. Chatzipanagis, M. Iafisco, T. Roncal-Herrero, M. Bilton, A. Tampieri, R. Kröger, J. M. Delgado-López, Crystallization of citrate-stabilized amorphous calcium phosphate to nanocrystalline apatite: a surface-mediated transformation, Cryst. Eng. Comm. 18 (2016) 3170–3173. https://doi.org/10.1039/C6CE00521G.

71. H. Saito, Y. Araki, H. Katsuno, T. Nakada, Phase transition of amorphous calcium phosphate to calcium hydrogen phosphate dihydrate in simulated body fluid, J. Cryst. Growth. 553 (2021) 125937. https://doi.org/10.1016/J.JCRYSGRO.2020.125937.

72. M. Edén, Structure and formation of amorphous calcium phosphate and its role as surface layer of nanocrystalline apatite: Implications for bone mineralization, Materialia (Oxf) 17 (2021) 101107. https://doi.org/10.1016/j.mtla.2021.101107.

73. A. Indurkar, P. Kudale, V. Rjabovs, I. Heinmaa, Ö. Demir, M. Kirejevs, K. Rubenis, G. Chaturbhuj, M. Turks, J. Locs, Small organic molecules containing amorphous calcium phosphate: synthesis, characterization and transformation, Front. Bioeng. Biotechnol. 11 (2023) 1329752. https://doi.org/10.3389/FBIOE.2023.1329752.

74. R. Gelli, F. Ridi, P. Baglioni, The importance of being amorphous: calcium and magnesium phosphates in the human body, Adv. Colloid. Interface Sci. 269 (2019) 219–235. https://doi.org/10.1016/j.cis.2019.04.011.

75. S. Jiang, Y. Cao, S. Li, Y. Pang, Z. Sun, Dual function of poly(acrylic acid) on controlling amorphous mediated hydroxyapatite crystallization, J. Cryst. Growth. 557 (2021) 125991. https://doi.org/10.1016/J.JCRYSGRO.2020.125991.

76. V. M. Wu, E. Huynh, S. Tang, V. Uskoković, Calcium phosphate nanoparticles as intrinsic inorganic antimicrobials: Mechanism of action, Biomedical Materials (Bristol) 16 (2021) 015018. https://doi.org/10.1088/1748-605X/ABA281.

77. I. I. Grynyuk, O. M. Vasyliuk, S. V. Prylutska, N. Y. Strutynska, O. V. Livitska, M. S. Slobodyanik, Influence of nanoscale-modified apatite-type calcium phosphates on the biofilm formation by pathogenic microorganisms, Open Chem. 19 (2021) 39–48. https://doi.org/10.1515/CHEM-2021-0199.

78. V. Uskoković, S. Tang, M. G. Nikolić, S. Marković, V. M. Wu, Calcium phosphate nanoparticles as intrinsic inorganic antimicrobials: In search of the key particle property, Biointerphases. 14 (2019) 031001. https://doi.org/10.1116/1.5090396.

79. A. Bondi, Van der Waals volumes and radii, Journal of Physical Chemistry. 68 (1964) 441–451. https://doi.org/10.1021/J100785A001.

80. N. C. Blumenthal, V. Cosma, S. Levine, Effect of gallium on the in vitro formation, growth, and solubility of hydroxyapatite, Calcif Tissue Int. 45 (1989) 81–87. https://doi.org/10.1007/BF02561406.

81. Y. In, U. Amornkitbamrung, M. H. Hong, H. Shin, On the crystallization of hydroxyapatite under hydrothermal conditions: Role of sebacic acid as an additive, ACS Omega. 5(42) (2020) 27204–27210. https://doi.org/10.1021/acsomega.0c03297.

82. M. Mosina, C. Siverino, L. Stipniece, A. Sceglovs, R. Vasiljevs, T. F. Moriarty, J. Locs, Gallium-Doped Hydroxyapatite Shows Antibacterial Activity against Pseudomonas aeruginosa without Affecting Cell Metabolic Activity, J. Funct. Biomater. 14(2) (2023) 51. https://doi.org/10.3390/jfb14020051.

83. A. Ballardini, M. Montesi, S. Panseri, A. Vandini, P.G. Balboni, A. Tampieri, S. Sprio, New hydroxyapatite nanophases with enhanced osteogenic and anti-bacterial activity, J. Biomed. Mater. Res. A. 106(2) (2017) 521–530. https://doi.org/10.1002/jbm.a.36249.

84. F. He, Y. Tian, Improvements in phase stability and densification of β-tricalcium phosphate bioceramics by strontium-containing phosphate-based glass additive, Ceram. Int. 44(10) (2018) 11622–11627. https://doi.org/10.1016/j.ceramint.2018.03.236.

85. J. Liu, L. Zhao, L. Ni, C. Qiao, D. Li, H. Sun, Z. Zhang, The effect of synthetic α-tricalcium phosphate on osteogenic differentiation of rat bone mesenchymal stem cells, Am. J. Transl. Res. 7(9) (2015) 1588–1601. https://www.ncbi.nlm.nih.gov/pmc/articles/PMC4626420/.

86. M. Trzaskowska, V. Vivcharenko, A. Przekora, The Impact of Hydroxyapatite Sintering Temperature on Its Microstructural, Mechanical, and Biological Properties, Int. J. Mol. Sci. 24(6) (2023) 5083. https://doi.org/10.3390/ijms24065083.

87. K. Salma, N. Borodajenko, A. Plata, L. Berzina-Cimdina, A. Stunda, Fourier Transform Infrared Spectra of Technologically Modified Calcium Phosphates, in 14th Nordic-Baltic Conference on Biomedical Engineering and Medical Physics, IFMBE Proceedings, 20 (2008) 68–71. https://doi.org/10.1007/978-3-540-69367-3_19.

88. D. Fan, L. Q. Chen, S. P. P. Chen, Numerical simulation of Zener pinning with growing second-phase particles, Journal of the American Ceramic Society. 81(3) (2005) 526–532. https://doi.org/10.1111/j.1151-2916.1998.tb02370.x.

89. M. Sceglova, N. Döbelin, R. Vasiljevs, L. Stipniece, J. Locs. Influence of gallium doping on the thermal stability and microstructure of sintered hydroxyapatite bioceramics, Ceram. Int. 51(14) (2025) 41150-42261. https://doi.org/10.1016/j.ceramint.2025.06.440

APPENDICES

Appendix I

Gallium containing calcium phosphates: Potential antibacterial agents or fictitious truth

Marika Mosina, Ilijana Kovrlija, Liga Stipniece, Janis Locs

Acta Biomaterialia, **2022**, 150, 48-57. doi: 10.1016/j.actbio.2022.07.063

M.S. input: conceptualization, investigation, visualization, writing the original draft, reviewing and editing.

Acta Biomaterialia 150 (2022) 48–57

Contents lists available at ScienceDirect

Acta Biomaterialia

journal homepage: www.elsevier.com/locate/actbio

Review article

Gallium containing calcium phosphates: Potential antibacterial agents or fictitious truth

Marika Mosina[a,b,*], Ilijana Kovrlija[a], Liga Stipniece[a,b], Janis Locs[a,b]

[a] Rudolfs Cimdins Riga Biomaterials Innovation and Development Centre, Institute of General Chemical Engineering, Faculty of Materials Science and Applied Chemistry, Riga Technical University, Pulka 3, Riga LV-1007, Latvia
[b] Baltic Biomaterials Centre of Excellence, Headquarters at Riga Technical University, Riga, Latvia

ARTICLE INFO

Article history:
Received 17 May 2022
Revised 30 June 2022
Accepted 29 July 2022
Available online 3 August 2022

Keywords:
Gallium
Calcium phosphates
Antibacterial
Biocompatibility
Hydroxyapatite

ABSTRACT

Amidst an ever-increasing demand for the enhancement of the lifestyle and the modulation of modern diseases, the functionalization of biomaterials is of utmost importance. One of the leading materials for the aforementioned purpose have been calcium phosphates (CaPs). They have been widely used in bone regeneration displaying favourable regenerative potential and biological properties. Many studies have placed their entire focus on facilitating the osteogenic differentiation of stem cells and bone progenitor cells, while the aspect of antibacterial properties has been surmounted. Nevertheless, increasing antibiotic resistance of bacteria requires the development of new materials and the usage of alternative approaches such as ion doping. Gallium (Ga) has been the potential star on the rise among the ions. However, the obstacle that accompanies gallium is the scarcity of research performed and the variety of amalgamations. The question that imposes itself is how a growing field of therapeutics can be further entwined with advances in material science, and how will the incorporation of gallium bring a new outlook. The present study offers a comprehensive overview of state-of-the-art gallium containing calcium phosphates (GaCaPs), their synthesis methods, antibacterial properties, and biocompatibility. Considering their vast potential as antibacterial agents, the need for a methodical perspective is highly necessary to determine if it is a direction on the brink of recognition or a fruitless endeavour.

Statement of significance

Although several studies have been published on various metal ions-containing calcium phosphates, to this date there is no systematic overview pointing out the properties and benefits of gallium containing calcium phosphates. Here we offer a critical overview, including synthesis, structure and biological properties of gallium containing calcium phosphates.

1. Introduction

Bone remodelling encompasses a myriad of interconnected pathways that uninterruptedly unravel during the entire lifetime, while at the same time being subjected to the constantly varying laws of biomechanical forces. The end goal of this process is to have a functional model, which has to possess appropriate mechanical strength. Nonetheless, due to chronic bone diseases such as cancer, hypercalcemia, osteoporosis, or trauma, bone defects are being formed, lacking the ability to be healed or remodelled on their own [1]. In order to overcome this tremendous burden, clinicians and researchers are continuously developing new bone graft materials for bone defect repair, thus creating a high demand for further amelioration of biomaterials [2].

To come as close as possible to the creation of a suitable bone graft model, primarily the composition of bone must be considered. Bone consists of the organic part (30 wt% of mineralized collagen) [3] and inorganic part (60 wt%) - mineral phase, known as hydroxyapatite (HAp) [3,4]. The remaining 10 wt% of the bone composition is water [4]. Considering that HAp is probably the

* Corresponding author at: Rudolfs Cimdins Riga Biomaterials Innovation and Development Centre, Institute of General Chemical Engineering, Faculty of Materials Science and Applied Chemistry, Riga Technical University, Pulka 3, Riga LV-1007, Latvia.
E-mail addresses: marika.mosina@rtu.lv (M. Mosina), ilijana.kovrlija@rtu.lv (I. Kovrlija), liga.stipniece@rtu.lv (L. Stipniece), janis.locs@rtu.lv (J. Locs).

https://doi.org/10.1016/j.actbio.2022.07.063

most recognized member of the calcium orthophosphate family, the rationale for using calcium phosphates (CaPs) imposed itself quite easily. Furthermore, extensive studies have shown that different CaPs showed promising results as bone graft materials and their outstanding track record has been verified throughout the last few decades. The most commonly used CaPs, to date, are HAp ($Ca_{10}(PO_4)_6(OH)_2$) and tricalcium phosphate (TCP; $Ca_3(PO_4)_2$), followed by an abundance of various derivatives [5,6]. In addition to their well-suited composition, they have shown exceptional bioactivity and biocompatibility with cell lines, which are the main participants of the bone microenvironment [7–11]. On the other hand, while the CaPs have been characterized in terms of their osteoconductive properties, the material still is not as competent as the natural apatite [12,13]. A hindrance to the otherwise noteworthy case history of CaPs has been their poor mechanical strength under continuous stress circumstances, most probably connected with challenges associated with the sintering process and their low surface area (typical 2–5 m^2/g) [14].

An additional important aspect of the clinical application of biomaterials is their antibacterial potential. The lack of antibacterial properties of CaPs could cause a risk of infection after the implantation of biomaterial. Infection is related to bacteria adhesion and colonization on implant or material surface. Additionally, the formation of biofilm can be a potential source of systematic infection [15]. Infection is an outcome of bacterial contamination, which can occur in a dry state or under wet conditions. Dry state contamination commonly appears before implantation, and it may be transmitted in the surgical room or due to the unsterile supplies that are being used. By using adequate sterilization this contamination can be controlled [15]. Wet condition contamination is related to bacteria adhesion on the biomaterial surface in an aqueous solution. This type of contamination is affected by different parameters of material, physiological environment and pathogens. In particular, surface morphology, physicochemical properties of material, environment pH, temperature and electrolytes [15,16]. The traditional approach for treating these infections is based on the use of systemic administration of the antibiotics (vancomycin, rifampicin, fluoroquinolone, etc.) for up to six weeks [17]. This approach has several drawbacks, including systemic toxicity, uneven distribution throughout the body and low accumulation in the target site [18,19]. Therefore, methods are being sought to ensure local delivery of antibiotics at the site of implantation. Additionally, the World Health Organisation (WHO) data shows that antibiotic resistance is becoming a global health threat. Successful treatment of infections in modern medicine would be at an even greater risk without developing alternatives. New antibiotic development is a time-consuming procedure, and in the report submitted in 2019, the WHO identified 32 antibiotics in clinical development, of which only six were classified as innovative [20].

Nevertheless, pure antibiotics are not the only answer to modern perils. Different metal ions had shown antibacterial properties and were used a long time before antibiotics were discovered [21–23]. Copper (Cu) and silver (Ag), for example, have been mentioned as far back as ancient Egypt, as components used for water disinfection. Due to their characteristics, non-essential metal ions, Ag or tellurium (Te) being one of them, can be toxic to the biological system, if they are admitted in abundant concentrations [24,25]. However, using metal ions in small concentrations can provide a desired antibacterial effect.

Antibacterial properties of metal ions depend on the charge and electronegativity. In the biological system, metal ion chemistry could enforce different reactions and diverse bindings to the proteins, causing a beneficial after effect [21,26]. The exact mechanism of metal ion interaction with bacteria has not been fully determined and understood. However, several antibacterial activity mechanisms of metal ions or nanoparticles have been proposed and outlined below (Fig. 1):

1) Ion fixation – due to electrostatic forces fixation could occur, leading to the membrane damage. It affects the free transport of protons, and other molecules passing in and out of the bacteria cell, resulting in the loss of membrane potential [21,27].
2) Metal ion has the potential to interact with the bacteria cell membrane and to take action in regulating the production of adenosine triphosphate (ATP), as well as the replication process, which causes the deoxyribonucleic acid (DNA) damage [21,27].
3) Formation of the free radicals (reactive oxygen species: ROS) – in this step, oxygen stress starts to form, resulting in the damage of bacteria membrane, DNA and mitochondria, leading lastly to bacteria death [5,21,28,29].
4) Protein dysfunction and loss of enzyme activity [21].

Biomaterials, containing different metal ions, empower long-term local ion release, providing antibacterial action at the surgical site [30,31]. Such metal ions for doping or substituting have been used: silver (Ag^+), zinc (Zn^{2+}), strontium (Sr^{2+}), sodium (Na^+), copper (Cu^{2+}) and others [2,32]. Additionally, metal ions, for instance calcium (Ca^{2+}), iron (Fe^{2+}), magnesium (Mg^{2+}), manganese (Mn^{2+}) and others are essential elements in our body, found primarily in protein metabolism [33,34].

2. Gallium

Gallium (Ga) is a semi-metallic III group element [35] and a non-essential element in the human body [36]. Its ionic radius of 0.620 Å, rendered as octahedral, is very close to the radius of ferric ion (Fe^{3+}) – 0.645 Å [5]. In addition, the tetrahedral ionic radii of both ions are also very close, 0.47 Å for Ga^{3+} and 0.49 Å Fe^{3+}.

From the 1970s gallium compounds were investigated as therapeutic agents, while simultaneously they were exhibiting different behaviours, including the inhibition of bone resorption [37,38] and promotion of bone growth. Even more, they were involved in the effective treatments of autoimmune diseases – cancer, osteoporosis [39] and copious infectious diseases. Gallium compounds play an important role in the bone-tumour imaging and they have shown antimicrobial and antibacterial properties [35,40,41]. Gallium nitrate is used as a drug to treat hypercalcemia in humans, while gallium maltolate showed toxic influence on lymphoma cells, which accordingly inhibit the growth of the cancer cells [42,43]. Additionally, the aforementioned gallium salts such as gallium maltolate, nitrate and citrate, along with the complex siderophores and hemes are being used as carriers. They deliver Ga^{3+} to a wide range of bacteria, making it a perspective treatment for bacterial infections [6,35,41,44].

When the inhibitory, immunomodulating, anti-hypercalcemic and analgesic operations of Ga^{3+} are in question, the importance falls on the capability to mimic iron species and act as a competitor for tumour cells that require positively charged ion to grow and survive [5]. These actions are supported by the fact that gallium and ferric ions have the same oxidation state (+3) and a similar ionic radius. Gallium starts its therapeutic effect by disrupting the “native” ferric iron’s binding in the enzyme active site. As it is redox inactive it impels the enzyme’s activity in question [45,46]. The metalloprotein that is pivotal for anticancer therapy is ribonucleotide reductase, which is Fe^{3+} dependent and indispensable for the DNA synthesis in living cells. The mechanism transpires through two parallel actions. The first one is the uptake of gallium ion instead of ferric ion, thus inhibiting the proliferation of the cancer cell, which requires a greater amount of ferric ions to function properly. The second process incorporates the redox inactive Ga^{3+} in the active site, stopping the production of DNA and causing the apoptosis of the cancer cell [45].

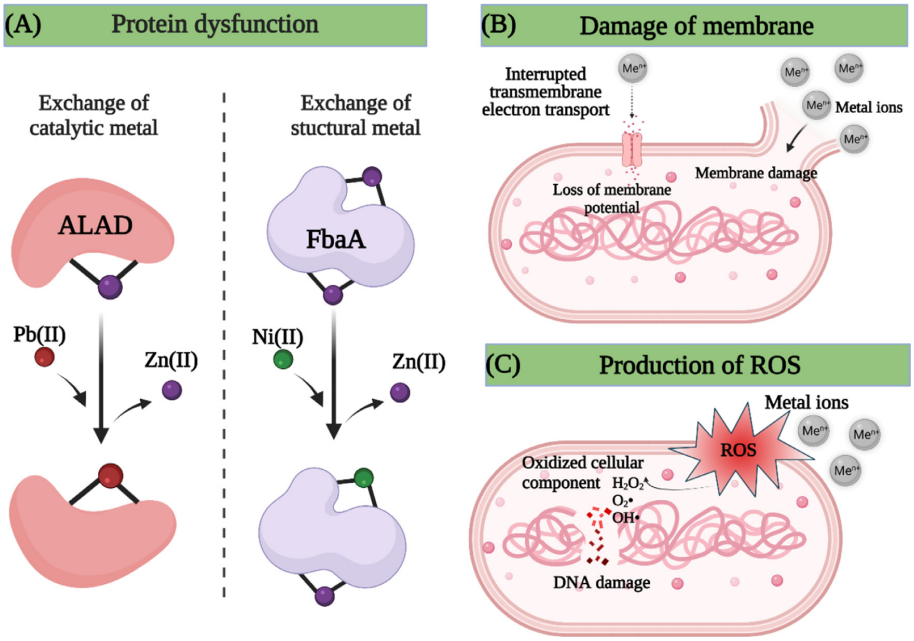

Fig. 1. Mechanism of metal ion interaction with bacteria (A) Metals leading to protein dysfunction by enzyme metal exchange; (B) Metal ion fixation leading to the membrane damage; (C) Production of reactive oxygen species (ROS); ALAD - δ-aminolevulinic acid dehydratase; FbaA - fructose-1,6-bisphosphate aldolase; ROS - reactive oxygen species (created with BioRender.com; adapted from [21,27]).

Despite it being known for decades, it is still unclear what effect gallium has on the bone and its related processes [47]. Data from several studies detected deposition of Ga^{3+} in the bone tissue, presumably related to its linkage with bone remodelling on active metaphyseal growth plates and healing fractures [31,40]. Additionally, Bernstein et al., have introduced Ga^{3+} ion as the inhibitor for the SARS-CoV-2 virus [48].

3. Antibacterial activity of gallium

Due to the above-mentioned similarity between Ga and Fe ions, it is possible to replace Fe^{3+} with Ga^{3+} in the metabolism of the protein, thus interfering with the functioning of bacterial cells [49]. As a result, Ga^{3+} exhibited a less toxic outcome, compared to silver ions [5,35,49]. Extensive research has shown that Ga^{3+} has antibacterial activity against iron-dependent bacteria, such as *P. aeruginosa* [50,51]. Approaches of bacterial iron uptake and metabolism have been shown in the Fig. 2. Fe^{3+} has low bioavailability, so its uptake and transport relays on the iron-binding proteins, transferrin or lactoferrin, heme or heme-containing proteins and siderophores [21,50,51]. Bacteria synthesize siderophores (Greek for “iron” and “bearer”), which are low-molecular-weight compounds that scavenge iron (in the Fe^{3+} oxidation state) from the environment, hence making it important for bacterial growth and survival [52].

During the infection, the place of siderophore-mediated iron uptake plays an important role in the colonization, growth and survival of the bacteria [21,50–52]. The properties that Ga^{3+} shares with Fe^{3+} permit it to bind with high avidity to these iron-binding proteins. Ga^{3+} antibacterial activity is based on “*Trojan horse*” strategy (Fig. 2) [21,53]. This mechanism pathway rests on “tricking” the bacteria to take up the toxic Ga^{3+} that mimics Fe^{3+} ions. Gallium interrelates with the siderophores and lowers

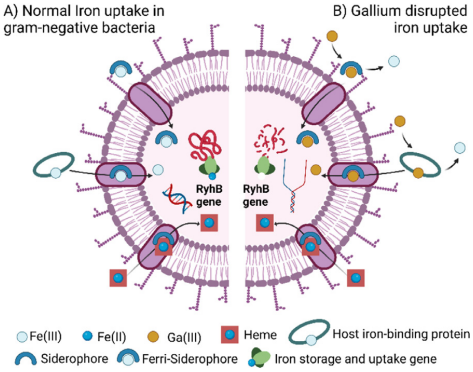

Fig. 2. Iron uptake metabolism approach of the iron-dependent bacteria A) in normal conditions; B) in presence of gallium (adapted from [50], created with Biorender.com).

the number of chelators in the environment designated for providing the ferric ion needed for bacteria. The host cell takes in the newly created gallium-siderophore complex, supplying itself with the redox-inactive cation, ultimately hampering the bacterial metabolism [45,54].

By disrupting the bacteria metabolism, the essential actions needed for them to survive are being destroyed: DNA synthesis and repair, respiration and oxidative stress response. The entire process, combined with several subsequent actions that have been described in the literature, finally results in the bacteria death [50,55]. Several studies have shown that Ga^{3+} has an antibacterial

Table 1
Synthesis routes of CaPs.

Product	Methods	Ref.
Ga-doped HAp	Ultrasound-assisted ion exchange	[63]
HAp modified by gallium	Wet chemical precipitation	[47,49]
Ga-containing HAp	Hydrolysis of urea	[41]
HAp modified by gallium	Solid-state reaction	[49]
Ga-containing HAp	Hydrothermal synthesis	[64]
Ga-containing β-TCP	Solid-state reaction	[40,65–67]
Ga-doped ACP	Wet chemical precipitation	[68]

influence on Gram-negative and Gram-positive bacteria (e.g. *M. tuberculosis* and *M. avium, S. aureus, E. coli* [56], as well as *P. aeruginosa*, which is multidrug-resistant bacteria) [21,57].

As shown, the different activity mechanisms of Ga^{3+} have the ability to separate it from the other metal ions, especially when being used for therapeutic and antibacterial purposes. Furthermore, gallium has the possibility to be incorporated in different CaPs, giving an extended possibility for a controlled and local ion release. Given the growing field of therapeutics, in the next section localized spatiotemporal release effects will be described in more detail.

4. Gallium containing calcium phosphates (GaCaPs)

Being recognized as the most suitable substitute for biological apatite, HAp has undergone the research on different ion incorporations, stemming from monovalent to divalent ions [58–60]. However, even with the wide array of tested ions, the lack of research on using Ga^{3+} for HAp, but also for the other members of the orthophosphate family is evident in the literature [2,61,62]. In order to understand properly the mechanism of Ga^{3+} incorporation and the outcome it elucidates, the synthesis route and the structure of the CaPs have to be taken into account. Furthermore, the range of concentrations of the Ga^{3+} ion must be carefully monitored. In the following subsections synthesis methods of GaCaPs, more specifically amorphous calcium phosphate (ACP), HAp and β-tricalcium phosphate (β-TCP) will be conferred in more detail.

The process of doping encompasses interstitial incorporation of the ion or its placing between atom layers. However, substituted refers to the atom (element) exchange in a certain atomic position – crystallographic term. The impact of whether Ga^{3+} ions are doped or substituted in conventional CaPs is yet to be understood and current state of the art will be presented in the following sections.

4.1. Synthesis routes

The two main principles being used in obtaining GaCaPs are synthesis in aqueous media and solid-state reaction. The most popular method, however, is the wet precipitation route, while sol-gel and hydrolysis methods are not being used as often (Table 1).

4.1.1. Hydrolysis method

Hydrolysis is a water ionization process that results in the diffusion of hydrogen and hydroxide ions. According to Mohd Pu'ad et al. it is the least used wet synthesis method [69]. In the hydrolysis process it is possible to transform the calcium and phosphate precursors to HAp [69]. For example, α-TCP can be transformed to HAp by mixing it with different solvents, succeeded by hydrolysis for 2–120 h at 70 °C. The time needed for completing hydrolysation is dependent on chosen solvent. Hence, using 1-octanol as a solvent would take more than 24 h to completely hydrolyse α-TCP to HAp [69,70]. As one of the most common sources of calcium and phosphorous ions, calcium nitrate tetrahydrate ($Ca(NO_3)_2{}^*4H_2O$) and diammonium hydrogen phosphate ($(NH_4)_2HPO_4$) are being used. Once urea has been added into the synthesis media, the suspension is heated in the temperature range of 80-90°C [41,71]. Kurtjak et al. used the same approach with an additional step of sonication of the mixture, to obtain Ga-containing HAp [41]. Nonetheless, the hydrolysis synthesis of CaP requires temperatures higher than the room temperature, which is the main reason why this method is unlikely to be used.

4.1.2. Sol-gel method

During the sol-gel method, calcium and phosphorus precursors are mixed in the presence of a solvent thereby forming "sol". Subsequently, the solvent is removed and "gel" is formed by heating. In this method organic solvents, such as ethanol, butanol and others are being used [72,73]. Alkoxides are frequently used as calcium and phosphorus precursors, for instance, calcium acetate, calcium diethoxide, triethyl phosphate or phosphite are some of the representatives [72–74]. This method is suitable for the production of thin-film coatings [72,73]. Additionally, when CaP sol-gel is formed a porous scaffold can be produced by using the foam replica technique [75]. However, so far this method has not been used for obtaining Ga-doped CaPs.

4.1.3. Wet chemical precipitation method

One of the most extensively used synthesis routes, in aqueous media, is wet chemical precipitation. HAp or ACP are commonly obtained by this method. The wet chemical precipitation method is based on the mixing of two salts, where one serves as the source of Ca^{2+} ions and the other as $PO_4{}^{3-}$ ion precursor. Salts which are diversely used for the precipitation are calcium nitrate tetrahydrate ($Ca(NO_3)_2{\cdot}4H_2O$) and diammonium hydrogen phosphate ($(NH_4)_2HPO_4$) [49,68]. The wet precipitation method consists of two synthesis steps: precipitation of two different ion precursors and ageing of obtained suspension, during which the HAp phase is being formed [69].

Kurjak et al. studied the influence of Ga^{3+} addition in different steps of the synthesis (Fig. 3). Introducing Ga^{3+} precursor at the beginning of the synthesis, together with initial raw materials, is known as co-precipitation of GaHAp(CP) (Fig. 3A). When Ga^{3+} precursor is introduced before the ageing, GaHAp(TR) is obtained by transformation in the wet chemical precipitation method (Fig. 3B). Eventually, if Ga^{3+} is added at the end of the synthesis, together with the final HAp crystals, the ion-exchange approach follows and GaHAp (IE) is obtained (Fig. 3C) [41]. It was found that the various approaches affect the capability of ion release from the material, resulting in diverse antibacterial properties. As there are multiple ways of Ga^{3+} incorporation in CaPs, it can be found in the structure or adsorbed on the surface [41].

Throughout the literature, various combinations of wet chemical precipitation and other methods (i.e., ultrasound-assisted ion exchange, hydrolysis, hydrothermal synthesis) can be found. For instance, Kurtjak et al. combined the wet precipitation method with sonication and hydrolysis [41]. Additionally, the wet chemical precipitation method has different synthesis variables – Ca/P molar ratio, pH, temperature and ageing time, where all of the aforementioned variables can influence the final properties of HAp [69,76]. As gallium sources $Ga(NO_3)_3{}^*xH_2O$ [41,49,64,65,77], gallium trichloride ($GaCl_3$) [47] and gallium(III) trioxide (Ga_2O_3) [40,66,67] were used.

For obtaining pure HAp, without the presence of other CaP phases, synthesis pH was maintained from 9 to 10 [49,68]. Once Ga^{3+} ions were present in the equation, the hard acidic nature of Ga^{3+} itself in the aqueous media should be taken into account. If the synthesis conditions are maintained at a wide pH range, hydrolysation can transpire, leading to the formation of hydroxylate species, predominantly gallium gallate $[Ga(OH)_4]^-$. The resulting formation of the hydronium ion (H_3O^+) in aqueous media leaves

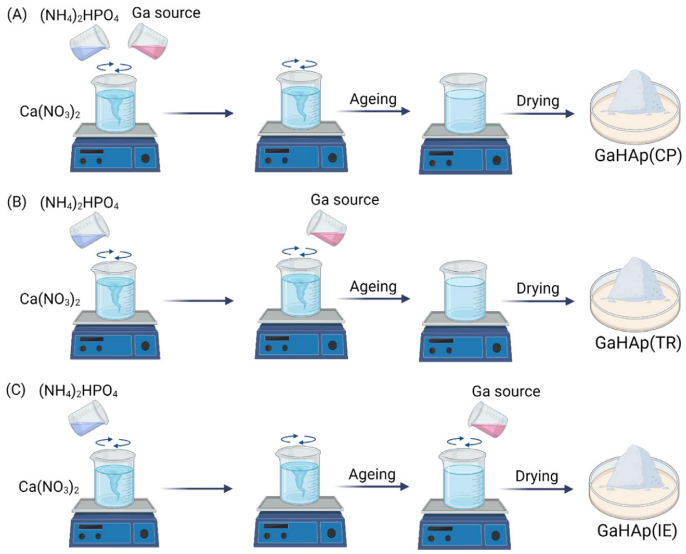

Fig. 3. Wet precipitation method of GaHAp (A) co-precipitation; (B) transformation and (C) ion-exchange (created with BioRender, inspired from [41]).

the synthesis solution highly acidic [45,78,79], leading to a difference in the final synthesis pH, which ultimately affects obtaining of the pure HAp in the presence of Ga^{3+}.

4.1.4. Solid-state reaction

The solid-state reaction is known as a dry method and it requires the use of high-energy processing or high temperatures. This method has been primarily used to obtain Ga-β-TCP ceramics or cements [40,65–67]. The crucial point of the solid-state reaction is the heat treatment temperature, and since TCP has two polymorph forms, α and β (which have different thermal stability), it requires a careful consideration [80,81]. Mellier et al. sintered anhydrous calcium phosphate, calcium carbonate, and gallium oxide mixture at 1000 °C for 24 h and obtained Ga-β-TCP [31,66,82]. Qiu et al. sintered Ga-TCP at 1000 °C for two hours and in order to obtain bioceramics, the attained Ga-TCP was mixed with paraffin, then moulded and sintered at 1250 °C for an additional 2 h. This resulted in TCP bioceramics with different compositions and diverse Ga^{3+} rates in the final product. Products synthesized without Ga^{3+} exhibited the α-TCP structure, whereas the products with up to 1.25 wt% of Ga^{3+} revealed the biphasic TCP, comprised of α- and-β-TCP. When Ga^{3+} was used in the range from 2.5 wt% to 7.5 wt%, pure β-TCP was formed [40]. By applying high temperatures, transformations between TCP polymorph forms occurs. Nevertheless, the reconversion of phases depends on the cooling rate [80].

4.2. Incorporation of the gallium ion in calcium phosphates

Antibacterial properties of various CaPs have been summarized in Table 2, while the biocompatibility has been described in the Table 3.

4.2.1. Gallium doped amorphous calcium phosphate (GaACP)

Yang et al. doped ACP with gallium ions, with initial (Ca+Ga)/P molar ratio being in the range from 1.8 to 3.0. XRD pattern revealed the characteristic wide bump around 30° 2Theta, indicating the formation of CaP with an amorphous structure. From ^{31}P and ^{71}Ga solid-state nuclear magnetic resonance (ssNMR) analysis, it was concluded that formed ACP, consisted of calcium phosphate clusters and gallium hydroxide oxide $Ga_x(OH)_yO_z$ clusters. Rapid Ga^{3+} ion release was observed in 24 h, while the further ion release stayed constant up to 96 h. Inhibition zone against *P.aeruginosa*, when in presence of GaACP, increased with increasing (Ca+Ga)/P molar ratio [68].

4.2.2. Gallium containing hydroxyapatite (GaHAp)

Another intrinsic approach has been the modification of HAp structure with Ga^{3+}. Possible interchange in the HAp structure, secures it from the resorption process and enhances the overall biomechanical properties of the skeletal system [64,77].

Being a member of CaPs that has the most resemblance to the apatite phase of human bone, HAp has been heavily utilized in multiple research areas, stemming from bone tissue engineering to the cell-targeting [83]. HAp ($Ca_{10}(PO_4)_6(OH)_2$) displays hexagonal crystal structure (Fig. 4.), with $P6_3/m$ space group symmetry and lattice parameters of γ=120 °, a=b=9.432 Å and c=6.881 Å [83–85]. However, HAp can be found also in the monoclinic form encompassing the $P2_1/b$ space group, with unit cell parameters of a=9.421 Å, b=2a and c=6.881 Å, while γ is 120° [85]. The Ca/P molar ratio of stoichiometric HAp is 1.67, which differs from the biological apatite, due to the diversion substitutions [84]. Depending on the type of the ion (electric charge, size etc.), different segments (PO_4^{3-}, Ca^{2+} or OH^-) of the crystal lattice have been substituted. An additional influence on the place of substitution in HAp was the net charge of crystal planes. In this instance, the a and b planes are positively charged hence they adsorb negatively-charged molecules, while the c plane is vice versa [74].

As a trivalent ion, Ga^{3+} is incorporated in the crystalline lattice either through heterovalent substitutions or through intercalations [64]. Depending on whether Ga^{3+} is introduced through gallium nitrate [41,87], gallium chloride [88] or sodium gallate [64], the total sum of the ionic radii can steer the mechanism of incorporation. When gallium nitrate is used, ion radii is larger (2.69 Å) than that of the Ca^{2+} (1.98 Å) and gallium forms a solid solution of intercalation. If it is in the form of gallate, the ionic radius is

Table 2
Antibacterial properties of GaCaPs.

Material	The obtained concentration of Ga^{3+}	Experimental material	Method	Result	Ref
GaHAp	13wt%	*E. coli, P. aeruginosa, S. epidermis*	Disk diffusion	*E. coli, S. epidermis* exhibited no inhibition zone; *P.aeruginosa* expressed the inhibition zone	[63]
		P. aeruginosa,	Microdilution antibiogram	Complete inhibition of bacteria growth for concentrations ranging from 0.1 g/L^{-1} g/L	
	3 wt% Co-precipitation 4 wt% Transformation 8 wt%; 15 wt% Ion Exchange	*P. aeruginosa*	Disk diffusion (24 h)	Inhibition zone increase in the order HAp(Ga)Co-Precicpitation < HAp(Ga) IonExchange < HAp(Ga)Transformation	[41]
			Microdilution antibiogram (1 day)	Inhibition of bacterial growth. The minimal inhibitory concentration (MIC): HAp(Ga)CP 0.9 g/L, HAp(Ga)TR 0.3 g/L, HAp(Ga)IE (8 wt% Ga) 0.1 g/L and HAp(Ga)IE (16 wt% Ga) 0.075 g/L	
	0.32 wt%	*P. fluorescen*	Disk diffusion (16–18 h)	Inhibition zone 17 mm, for Ga-HAp obtained with wet precipitation method, and 27 mm for Ga-HAp obtained with solid-state reaction. (HAp inhibition zone 13 mm)	[49]
GaACP	-	*P. aeruginosa*	Disk diffusion	An inhibition zone from 14 to 19 mm was observed. Increased with increasing (Ca+Ga)/P molar ratio.	[68]

Table 3
Biocompatibility of GaCaPs.

Material	Type of study	Experimental material	Result	Ref
GaHAp	*In vitro*	Mouse fibroblasts L929	Good cell survivability of HAp(Ga) materials: 80% for HAp(Ga)TR, 70% for HAp(Ga)IE (8 wt% Ga). Cytotoxic effect for HAp(Ga)IE (16 wt% Ga), cell viability less than 50%.	[41]
		Cercopithecus aetiops kidney cells VERO (ATCC)	No significant difference in cell growth between control and GaHap samples. Conclusion: inert, biologically compatible material.	[77]
		Mammalian cell line BALB/c 3T3 clone A31	Nontoxic effect of GaHap obtained with wet precipitation method. Toxic effect of GaHap obtained with solid-state reaction.	[49]
Ga-β-TCP ceramics	*In vitro*	Mouse bone mesenchymal stem cells	The proliferation of cells was not observed in the presence of β-TCP bioceramics containing Ga^{3+}ions.	[40]
		RAW264.7 murine monocyte cell line	Inhibition of osteoclastic-activity-related genes in presence of 2.5 wt% Ga-β-TCP ceramics.	
Ga-CaP cement (GaCPC)	*In vitro*	RAW264.7 murine monocyte cell line	Gallium ion release increased in presence of RAW263.7 cells.	[66]
	In vivo	Filing of cylinder defect in knee joint of New Zealand White rabbit	New bone formation was observed in close contact with cement surface after four weeks.	
	In vitro	Human osteoblasts and monocytes	Differentiation of human primary monocytes into osteoclasts when seeded alone on CPC or GaCPC was not observed.	
	In vivo	Lewis rats, Bilateral femoral	Higher amounts of fibrillar collagen were synthesized when the reconstruction occurred with Ga containing cements. Presences of Ga^{3+}induced a significant 23% increase in defect filling	[31]

1.64 Å, and it is possible to replace Ca^{2+} in the lattice, with no changes in crystallographic parameters [64]. As an alternative approach to doping, HAp nanorods can be coated with metallic Ga nanoparticles. Material obtained in this manner showed a characteristic crystalline structure of HAp and a non-crystalline layer of Ga particles with an oxide/hydroxide layer [89].

GaHAp revealed the characteristic hexagonal structure of HAp. Modification of Ga^{3+} did not cause a shift in the reflections of representative maxima of HAp. XRD pattern did not reveal additional reflection of new phases or changes in unit cell parameters [41,49,63,64,77,89]. However, different studies observed and described a decrease in crystallinity of GaHAp (Fig. 5), revealing the inhibition effect of Ga^{3+} on the formation of HAp crystals [41,47,49]. With the addition of Ga^{3+}, the amorphous surface layer of HAp in the form of gallium derivatives (e.g., gallium phosphates ($GaPO_4$)) can be observed [41,49,64,77]. The 3 wt% of water in GaHAp can be attributed to the mentioned disordered surface layer [64]. The amorphous structure of GaHAp surface layer was analysed with NMR and revealed that it has broader OH^- bands, compared to the pure HAp [41]. Theories assume that the surface layer, in the form of $GaPO_4$ is more toxic compared to $Ga(NO_3)_3$ [41]. The biological properties of Ga^{3+} are affected by its complexation with ligands in solution. For example, in water with neutral pH, precipitation of gallium hydroxide occurs. However, gallium ion remains in solution in presence of citrate. Additionally, its uptake by bacteria or cells is influenced by chemical speciation (the distribution of an element amongst chemical species in a system) of Ga^{3+} that occurs by ligand exchange [54].

GaHAp showed antibacterial properties against bacteria, e.g., *P.aeruginosa* and *P.fluorescen.* With the disc diffusion method, the inhibition zone was observed after 24 h against *P.aeruginosa* [41,63] and after 16-18 h against *P.fluorescen* [49]. HAp nanorods coated with Ga particles showed antibacterial activity against *P.aeruginosa* [89]. Inhibition concertation against *P.aeruginosa* for GaHAp was determined to be from 0.1 to 1 g/L of GaHAp suspension in Mueller Hinton broth [41,63]. Kurjak et al. observed inhibition for the gallium concentration even below 0.1 g/L [41,89]. The results were compared by the various incorporations of Ga^{3+} into the structure by using different synthesis methods. GaHAp produced by ion exchange (GaHAp(IE)) has sufficient antibacterial properties compared to the GaHAp obtained through transformation and co-precipitation method (GaHAp(TR)) mostly due to the fast ion release [41]. GaHAp(TR) and GaHAp(IE) showed superior antibacterial activity against *P.aeruginosa*, whereas GaHAp(IE) exhibited minimal inhibition concentration (MIC) of 0.075 g/L [41]. When GaHAp was functionalized with gold (Au) particles it showed antibacterial activity against *E.Coli, S.aureus* and *S.epidermidis,* whereas GaHAp alone did not have an antibacterial effect [63].

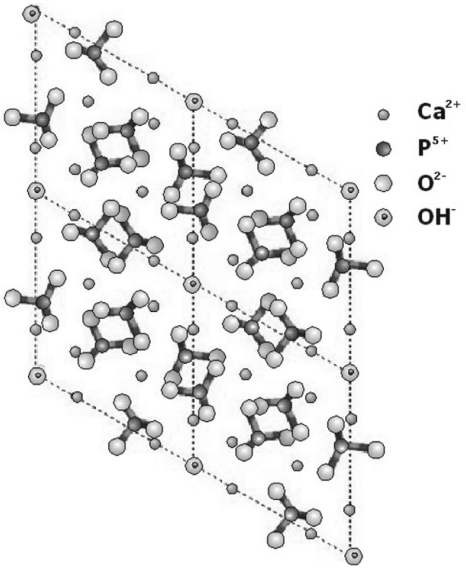

Fig. 4. Structure of hydroxyapatite (reprinted from [86] with permission).

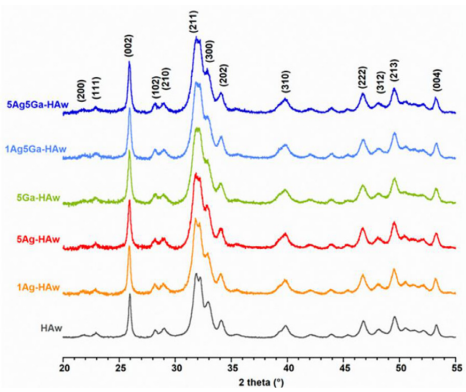

Fig. 5. XRD pattern of GaHAp samples synthesized by the wet chemical precipitation method (reprinted from the reference [49]).

Cytotoxicity of GaHAp *in vitro* was investigated with mammalian cells [49], human or animal fibroblasts [41,89] and monkey kidney cells VERO [77]. Furthermore, human osteoblasts and osteocytes were tested in the presence of gallium substituted calcium phosphate cement (CPC) [31]. At GaHAp concentration below and at minimal inhibition concentration (MIC) both human and mouse fibroblast cell viability showed good results of 80% [41,89]. However, in the values above MIC, human fibroblast viability decreased down to 50%. In contrast, mouse fibroblast viability in presence of 0.1 g/L GaHAp was 70% [89]. It should also be mentioned that GaHAp obtained with the ion-exchange method showed a toxic effect on mouse fibroblasts above MIC and cell viability was less than 50% [41,89]. A significant difference in the cell viability of African green monkey *Cercopithecus aetiops* kidney cells (Vero) was not observed both in the presence of HAp and GaHAp. Melnikov et al. showed in their study that GaHAp is a promising biocompatible material without toxic effect on monkey kidney cells VERO [77].

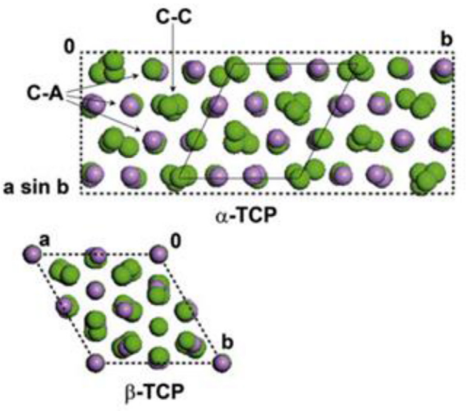

Fig. 6. Schematic structure of α-TCP and β-TCP unit cells along the [0 0 1] direction; C-C, cation–cation column; C-A, cation-anion column (reprinted from [91] Copyright (2011), with permission from Elsevier).

Furthermore, Pajor et al. observed the toxic effect of GaHAp obtained by the solid-state reaction at a concentration smaller than 12.5 mg/L. However, the toxic effect of GaHAp with a nominal Ga amount of 0.35 mass% obtained by the wet precipitation method was not observed [49]. The authors had no explanation for this observation; however, it can be related to the difference in solubility of the samples obtained by different synthesis methods.

4.2.3. Gallium containing β-tricalcium phosphate (Ga-β-TCP)

β-Tricalcium phosphate (β-TCP) is biocompatibile and has showed osteoconductive properties [67]. TCP exists in two polymorphs forms – α – and β – TCP, with a Ca/P molar ratio of 1.5 [40]. β-TCP displays rhombohedral structure (Fig. 6), with space group R3c symmetry and cell parameters of $a = b = 10.4$ Å, $c = 37.4$ and $\gamma = 120°$. The structure itself consists of 5 different Ca sites in which Ca atoms are distributed [90,91]. However, TCP can be found in α-TCP polymorph form as well, where it represents the monoclinic space group P21/a, with lattice constants being $a = 12.8$ Å, $b = 27.3$ Å, $c = 15.21$ Å, and $\gamma = 90°$ [91,92]. β-TCP has been found to exist in temperatures lower than 1125°C, whereas at a higher temperature it transformed into α-TCP [93].

Gallium incorporation affects β-TCP structure mainly because of the difference in ion radius of Ca^{2+} (0.99 Å) and Ga^{3+} (0.62 Å). Moreover, the electrovalence difference between Ga^{3+} and Ca^{2+} ions could lead to the formation of vacancy in the structure [40,67]. The theory says that gallium ions only occupy the octahedral M5 calcium site, while calcium occupation of the M4 site decreases in inverse proportion to the gallium content in the structure [66,82]. Possibly due to the different electrostatic repulsion between cation and phosphorous in M4 and M5 environments [94]. The XRD pattern displays the decrease in the unit cell parameters when in presence of Ga^{3+}. The shift of the characteristic peaks to the higher angles reveals the contraction of the cell unit. Ga-β-TCP dense ceramics have higher compressive strength compared to the pure β-TCP and it increases with increasing the Ga^{3+} content [66,82].

As in the case of GaHAp, the amorphous phase was also detected in Ga-β-TCP. Ga^{3+} prevented the transformation from β phase to α phase at Ga concentrations up to 2.5mol% [40]. Phase composition influences Ga^{3+} ion release in cell culture media, and since α-TCP is more soluble than β-TCP, it released higher concentrations of Ga^{3+}. Furthermore, bioceramics doped with Ga^{3+} at higher amounts of α-TCP phase have less porosity and higher com-

pressive strength [40]. Composite scaffolds with sintering agent phosphate-based glasses (PBG), with the composition of Ga-PBG and β-TCP, had increased compressive strength due to smaller macropore size. TCP-Ga-PBG scaffolds showed noticeably higher shrinkage, lower total porosity, smaller macropore size and denser microstructure [67]. *In vitro* studies reveal Ga-β-TCP did not affect the stem cells, however, inhibition of osteoclastic activity related genes was observed in the presence of Ga-β-TCP [40].

4.2.4. Gallium containing calcium phosphate cements (GaCPC)

Cement is ascribed with properties such as moldability and injectability, which after the injection into the bone, self-sets and hardens [31]. Calcium phosphate cement (CPC) is being used with different compositions that contain HAp, α-TCP and β-TCP, in different phase ratios. Ga^{3+} containing cement has been obtained by adding raw material, doped with Ga^{3+}. Cements with Ga-β-TCP showed higher setting time and cements containing gallium loaded calcium-deficient apatite (Ga-CDA) had higher compressive strength than cements without Ga^{3+} ion presence [65].

In vitro cell viability of human osteoblast decreased after 3 and 6 days in the presence of GaCPC, when compared to the pure CPC. However, in *in vivo* studies on Lewis, both CPC and Ga-CPC exhibited attributes of bone regeneration in the central area of the used implants, while the cortical regeneration transpired without the signs of inflammation or fibrous encapsulation [31].

Ga- cements in in vivo studies on New Zealand White rabbit femoral defects exhibited new bone formation on the surface of the implanted material after four weeks, compared to cements not containing gallium. [69]. Interestingly, gallium ion release increased in the presence of animal macrophages RAW264.7 cells [65], indicating phagocytic break down of particles.

5. Future directions and conclusions

In recent years, the possibility of gallium ion incorporation in multiple biomaterial strategies, by using calcium phosphates, has upheld the interest of the scientific community. Ga^{3+}-functionalized CaPs have proven to be effective antibacterial agents, while simultaneously promoting bone regeneration without inducing any immediate toxic effect. Even though gallium's similarity to iron exhibited an uncial antibacterial mechanism against bacterial infection and cancerous sites, it is still unclear how the differentiation, without a toxic effect on mammalian cells, occurs in biological processes (cell metabolism). It should also be taken into consideration that the biological properties of GaCaPs depend on the synthesis route of the material and the phase composition of CaPs. These variables have been found to influence the release of Ga^{3+} ions from the material, as well as ion incorporation in their structure. Furthermore, what was interesting to observe is that the addition of Ga^{3+} decreased crystallinity of HAp, but induced changes in unit cell parameters and shrinkage of the crystalline lattice of TCP.

From presented studies, GaCaP's showed promising inhibition of bacteria growth without noticeable toxic effect on human and animal cells. However, to date there is still a handful of reports on GaCaPs in the context of interfering with regenerative pathways or tissue engineering, particularly when compared to other well-examined ions in this field (e.g., Fe^{3+}). With an array of preliminary results indicating that the incorporation of gallium has promise in substituting Fe^{3+}, more materials favouring its properties should be considered as a step forward. For example, studies on Ga-β-TCP discuss material biocompatibility without data on antibacterial properties.

Additional hindrance, when it comes to the antibacterial properties of GaCaP, is related to the limited amount of data obtained from the investigations on a small number of bacteria strains. To fully cover the area of GaCaP antibacterial activity, a more comprehensive range of bacteria needs to be tested, for example, on anaerobic bacteria that is primarily present in the oral cavity. Nevertheless, the scarcity of research done on GaCaACP is evident. To the best of our knowledge, only one study was published so far. Considering that the results obtained were promising, further studies should be conducted to explore the potential of the GaACP combination. An added benefit to exploring the range and direction of the aforementioned combination is that ACP serves as a precursor for the formation of HAp [95–97]. Significant input can be done by investigating how Ga^{3+} ions influence the stability of ACP.

The so far presented results on the *in vitro* and *in vivo* cytotoxicity of GaCaP raise the question of what effect material has on bone remodelling related processes, especially on osteogenesis, osteoclast and osteoblast activity. Nevertheless, gallium, as the representative of the new, highly perspective ion is starting to be in the forefront of the research in the field of bone regeneration. The spectra of benefits, at this stage, can be easily challenged by the opulence of uncertainties. Given the many reported, but still understudied effects, we expect gallium to push its way to the forefront of research, as a part of materials tackling antimicrobial resistance and aiding in regeneration of tissues (Fig. 7).

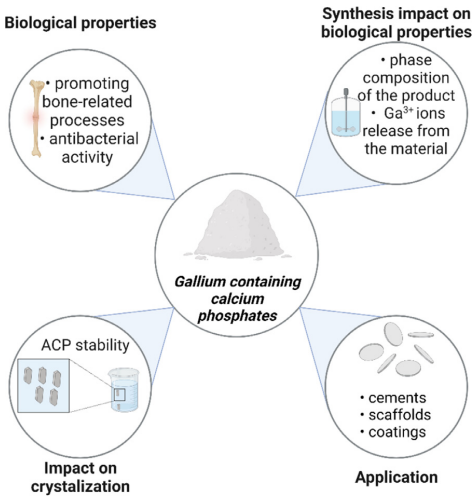

Fig. 7. Future perspectives and conclusions about gallium containing calcium phosphates (Created created with BioRender).

Funding

This work is funded by the EuroNanoMedIII project "NANO delivery system for one-shot regenerative therapy of peri-implantis" (ImlpantNano) and supported by the European Union's Horizon 2020 research and innovation programme under the Marie Skłodowska-Curie grant agreement [No 860462 (PREMUROSA)].

Declaration of Competing Interest

Authors do not have any conflicts of interest to declare.

Acknowledgement

The authors acknowledge support to the European Union's Horizon 2020 research and innovation programme under the grant agreement No. 857287.

References

[1] R. Owen, G.C. Reilly, In vitro models of bone remodelling and associated disorders, Front. Bioeng. Biotechnol. 6 (2018) 1–22, doi:10.3389/fbioe.2018.00134.

[2] J.T.B. Ratnayake, M. Mucalo, G.J. Dias, Substituted hydroxyapatites for bone regeneration: a review of current trends, J. Biomed. Mater. Res. - Part B Appl. Biomater. 105 (2017) 1285–1299, doi:10.1002/jbm.b.33651.

[3] M.F. Young, Bone matrix proteins: their function, regulation, and relationship to osteoporosis, Osteoporos. Int. 14 (3) (2003) 35–42 Suppl, doi:10.1007/s00198-002-1342-7.

[4] A.L. Boskey, Bone composition: relationship to bone fragility and antiosteoporotic drug effects, Bonekey Rep 2 (2013) 1–11, doi:10.1038/bonekey.2013.181.

[5] C.R. Chitambar, Gallium and its competing roles with iron in biological systems, Biochim. Biophys. Acta - Mol. Cell Res. 1863 (2016) 2044–2053, doi:10.1016/j.bbamcr.2016.04.027.

[6] S.P. Valappil, M. Coombes, L. Wright, G.J. Owens, R.J.M.M. Lynch, C.K. Hope, S.M. Higham, Role of gallium and silver from phosphate-based glasses on in vitro dual species oral biofilm models of Porphyromonas gingivalis and Streptococcus gordonii, Acta Biomater. 8 (2012) 1957–1965, doi:10.1016/j.actbio.2012.01.017.

[7] S. Saito, R. Hamai, Y. Shiwaku, T. Hasegawa, S. Sakai, K. Tsuchiya, Y. Sai, R. Iwama, N. Amizuka, T. Takahashi, O. Suzuki, Involvement of distant octacalcium phosphate scaffolds in enhancing early differentiation of osteocytes during bone regeneration, Acta Biomat 125 (2021) 309–322, doi:10.1016/j.actbio.2021.05.017.

[8] O.S. Yukari Shiwaku, K. Tsuchiya1, X. Linghao, Effect of calcium phosphate phases affecting the crosstalk between osteoblasts and osteoclasts in vitro, J. Biomed. Mater. Res. A 107 (2019) 1001–1013, doi:10.1002/jbm.a.36626.

[9] Y. Sai, Y. Shiwaku, T. Anada, K. Tsuchiya, T. Takahashi, O. Suzuki, Capacity of octacalcium phosphate to promote osteoblastic differentiation toward osteocytes in vitro, Acta Biomater. 69 (2018) 362–371, doi:10.1016/j.actbio.2018.01.026.

[10] J. Wang, Y. Chen, X. Zhu, T. Yuan, Y. Tan, Y. Fan, X. Zhang, Effect of phase composition on protein adsorption and osteoinduction of porous calcium phosphate ceramics in mice, J. Biomed. Mater. Res. - Part A 102 (12) (2014) 4234–4243, doi:10.1002/jbm.a.35102.

[11] S. Morimoto, T. Anada, Y. Honda, Comparative study on in vitro biocompatibility of synthetic octacalcium phosphate and calcium phosphate, Biomed. Mater. 7 (2012) 8, doi:10.1088/1748-6041/7/4/045020.

[12] R.Z. Legeros, G. Bonel, Types of "H20" in human enamel and in precipitated apatites, Calcif. Tissue Res. 118 (1978) 111–118.

[13] F.C.M. Driessens, J.W.E. Van Dijk, J.M.P.M. Borggreven, Biological calcium phosphates and their role in the physiology of bone and dental tissues I, Compos. Solub. Calcium Phosphates 137 (1978) 127–137.

[14] S.J. Kalita, A. Bhardwaj, H.A. Bhatt, Nanocrystalline calcium phosphate ceramics in biomedical engineering, Mater. Sci. Eng. C 27 (2007) 441–449, doi:10.1016/j.msec.2006.05.018.

[15] T. Mokabber, Electrochemically Deposited Antimicrobial Hydroxyapatite Coatings, University of Groningen, 2020, doi:10.33612/diss.132596200.

[16] D. Campoccia, L. Montanaro, C. Renata, A review of the biomaterials technologies for infection-resistant surfaces, Biomaterials 34 (2013) 8533–8554, doi:10.1016/j.biomaterials.2013.07.089.

[17] B.N. Kim, E.S. Kim, M.D. Oh, Oral antibiotic treatment of staphylococcal bone and joint infections in adults, J. Antimicrob. Chemother. 69 (2014) 309–322, doi:10.1093/jac/dkt374.

[18] G.R.P. Viswanathan, Y. Muralidaran, Chapter 7 - Challenges in Oral Drug Delivery: a Nano-based Strategy to Overcome, Elsevier Inc, 2017.

[19] J. Majumder, O. Taratula, T. Minko, Nanocarrier-based systems for targeted and site specific therapeutic delivery, Adv. Drug Deliv. Rev. 144 (2019) 57–77, doi:10.1016/j.addr.2019.07.010.

[20] W.H. Organization, Antimicrobial resistance, (2020). https://www.who.int/news-room/fact-sheets/detail/antimicrobial-resistance.

[21] J.A. Lemire, J.J. Harrison, R.J. Turner, Antimicrobial activity of metals: Mechanisms, molecular targets and applications, Nat. Rev. Microbiol. 11 (2013) 371–384, doi:10.1038/nrmicro3028.

[22] M.Y. Vaidya, A.J. McBain, J.A. Butler, C.E. Banks, K.A. Whitehead, Antimicrobial efficacy and synergy of metal ions against enterococcus faecium, klebsiella pneumoniae and acinetobacter baumannii in planktonic and biofilm phenotypes, Sci. Rep. 7 (2017) 1–9, doi:10.1038/s41598-017-05976-9.

[23] V. Stanić, S.B. Tanasković, Antibacterial Activity of Metal Oxide Nanoparticles, Elsevier B.V, 2020, doi:10.1016/b978-0-12-819943-5.00011-7.

[24] M. Simonin, A. Richaume, Impact of engineered nanoparticles on the activity, abundance, and diversity of soil microbial communities : a review, Environ. Sci. Pollut. Res. 22 (2015) 13710–13723, doi:10.1007/s11356-015-4171-x.

[25] L.A. Ba, D. Mandy, V. Jamier, C. Jacob, Tellurium : an element with great biological potency and potential, Org. Biomol. Chem. 8 (2010) 4203–4216, doi:10.1039/c0Ob00086h.

[26] A. Azam, A.S. Ahmed, M. Oves, M.S. Khan, S.S. Habib, A. Memic, Antimicrobial activity of metal oxide nanoparticles against Gram-positive and Gram-negative bacteria: a comparative study, Int. J. Nanomed. 7 (2012) 6003–6009, doi:10.2147/IJN.S35347.

[27] M.J. Hajipour, K.M. Fromm, A. Akbar Ashkarran, D. Jimenez de Aberasturi, I.R. de Larramendi, T. Rojo, V. Serpooshan, W.J. Parak, M. Mahmoudi, Antibacterial properties of nanoparticles, Trends Biotechnol. 30 (2012) 499–511, doi:10.1016/j.tibtech.2012.06.004.

[28] A. Jacobs, G. Renaudin, C. Forestier, J.M. Nedelec, S. Descamps, Biological properties of copper-doped biomaterials for orthopedic applications: a review of antibacterial, angiogenic and osteogenic aspects, Acta Biomater. 117 (2020) 21–39, doi:10.1016/j.actbio.2020.09.044.

[29] H. Alioui, O. Bouras, J.C. Bollinger, Toward an efficient antibacterial agent: Zn- and Mg-doped hydroxyapatite nanopowders, J. Environ. Sci. Heal. - Part A Toxic/Hazardous Subst. Environ. Eng. 54 (2019) 315–327, doi:10.1080/10934529.2018.1550292.

[30] S.P. Valappil, D. Ready, E.A. Abou Neel, D.M. Pickup, L.A. O'Dell, W. Chrzanowski, J. Pratten, R.J. Newport, M.E. Smith, M. Wilson, J.C. Knowles, Controlled delivery of antimicrobial gallium ions from phosphate-based glasses, Acta Biomater. 5 (2009) 1198–1210, doi:10.1016/j.actbio.2008.09.019.

[31] I. Strazic Geljic, N. Melis, F. Boukhechba, S. Schaub, C. Mellier, P. Janvier, J.P. Laugier, J.M. Bouler, E. Verron, J.C. Scimeca, Gallium enhances reconstructive properties of a calcium phosphate bone biomaterial, J. Tissue Eng. Regen. Med. 12 (2018) e854–e866, doi:10.1002/term.2396.

[32] J. Kolmas, E. Groszyk, D. Kwiatkowska-ró, Substituted hydroxyapatites with antibacterial properties, Biomed Res. Int. 2014 (2014) 15.

[33] A. Laskus, J. Kolmas, Ionic substitutions in non-apatitic calcium phosphates, Int. J. Mol. Sci. 18 (2017) 2542–2564, doi:10.3390/ijms18122542.

[34] M.A. Zoroddu, J. Aaseth, G. Crisponi, S. Medici, M. Peana, V.M. Nurchi, The essential metals for humans: a brief overview, J. Inorg. Biochem. 195 (2019) 120–129, doi:10.1016/j.jinorgbio.2019.03.013.

[35] A.B. Kelson, M. Carnevali, V. Truong-Le, Gallium-based anti-infectives: targeting microbial iron-uptake mechanisms, Curr. Opin. Pharmacol. 13 (2013) 707–716, doi:10.1016/j.coph.2013.07.001.

[36] American Elements, (2021). https://www.americanelements.com/gallium-iii-nitrate-hydrate-69365-72-6.

[37] E. Verron, M. Masson, S. Khoshniat, L. Duplomb, Y. Wittrant, M. Baud'Huin, Z. Badran, B. Bujoli, P. Janvier, J.C. Scimeca, J.M. Bouler, J. Guicheux, Gallium modulates osteoclastic bone resorption in vitro without affecting osteoblasts, Br. J. Pharmacol. 159 (2010) 1681–1692, doi:10.1111/j.1476-5381.2010.00665.x.

[38] E. Verron, A. Loubat, G.F. Carle, C. Vignes-Colombeix, I. Strazic, J. Guicheux, N. Rochet, J.M. Bouler, J.C. Scimeca, Molecular effects of gallium on osteoclastic differentiation of mouse and human monocytes, Biochem. Pharmacol. 83 (2012) 671–679, doi:10.1016/j.bcp.2011.12.015.

[39] E. Verron, J.M. Bouler, J.C. Scimeca, Gallium as a potential candidate for treatment of osteoporosis, Drug Discov. Today 17 (2012) 1127–1132, doi:10.1016/j.drudis.2012.06.007.

[40] C. Qiu, T. Lu, F. He, S. Feng, X. Fang, F. Zuo, Q. Jiang, X. Deng, J. Ye, Influences of gallium substitution on the phase stability, mechanical strength and cellular response of β-tricalcium phosphate bioceramics, Ceram. Int. 46 (2020) 16364–16371, doi:10.1016/j.ceramint.2020.03.195.

[41] M. Kurtjak, M. Vukomanović, A. Krajnc, L. Kramer, B. Turk, D. Suvorov, Designing Ga(iii)-containing hydroxyapatite with antibacterial activity, RSC Adv. 6 (2016) 112839–112852, doi:10.1039/c6ra23424k.

[42] C.R. Chitambar, M.M. Al-Gizawiy, H.S. Alhajala, K.R. Pechman, J.P. Wereley, R. Wujek, P.A. Clark, J.S. Kuo, W.E. Antholine, K.M. Schmainda, Gallium maltolate disrupts tumor iron metabolism and retards the growth of glioblastoma by inhibiting mitochondrial function and ribonucleotide reductase, Mol. Cancer Ther. 17 (2018) 1240–1250, doi:10.1158/1535-7163.MCT-17-1009.

[43] C.R. Chitambar, Medical applications and toxicities of gallium compounds, Int. J. Environ. Res. Public Health 7 (2010) 2337–2361, doi:10.3390/ijerph7052337.

[44] S.P. Valappil, G.J. Owens, E.J. Miles, N.L. Farmer, L. Cooper, G. Miller, R. Clowes, R.J.M. Lynch, S.M. Higham, Effect of gallium on growth of Streptococcus mutans NCTC 10449 and dental tissues, Caries Res. 48 (2014) 137–146, doi:10.1159/000354048.

[45] N. Kircheva, T. Dudev, Competition between abiogenic and biogenic metal cations in biological systems: mechanisms of gallium's anticancer and antibacterial effect, J. Inorg. Biochem. 214 (2021) 111309, doi:10.1016/J.JINORGBIO.2020.111309.

[46] V. Nikolova, S. Angelova, N. Markova, T. Dudev, Gallium as a therapeutic agent: a thermodynamic evaluation of the competition between Ga3+ and Fe3+ ions in metalloproteins, J. Phys. Chem. B 120 (2016) 2241–2248, doi:10.1021/acs.jpcb.6b01135.

[47] N.C. Blumenthal, V. Cosma, S. Levine, Effect of gallium on the in vitro formation, growth, and solubility of hydroxyapatite, Calcif. Tissue Int. 45 (1989) 81–87, doi:10.1007/BF02561406.

[48] L.R. Bernstein, L. Zhang, Gallium maltolate has in vitro antiviral activity against SARS-CoV-2 and is a potential treatment for COVID-19, Antivir. Chem. Chemother. 28 (2020) 1–4, doi:10.1177/2040206620983780.

[49] K. Pajor, Ł. Pajchel, A. Zgadzaj, U. Piotrowska, J. Kolmas, Modifications of hydroxyapatite by gallium and silver ions—physicochemical characterization, cytotoxicity and antibacterial evaluation, Int. J. Mol. Sci. 21 (2020) 1–15, doi:10.3390/ijms21145006.

[50] F. Minandri, C. Bonchi, E. Frangipani, F. Imperi, P. Visca, Promises and failures of gallium as an antibacterial agent, Future Microbiol 9 (2014) 379–397, doi:10.2217/fmb.14.3.

[51] B.R. Wilson, A.R. Bogdan, M. Miyazawa, K. Hashimoto, Y. Tsuji, Siderophores in iron metabolism: from mechanism to therapy potential, Trends Mol. Med. 22 (2016) 1077–1090, doi:10.1016/j.molmed.2016.10.005.

[52] N. Kircheva, T. Dudev, Gallium as an antibacterial agent: a DFT/SMD study of the Ga3+/Fe3+ competition for binding bacterial siderophores, Inorg. Chem. 59 (2020) 6242–6254, doi:10.1021/acs.inorgchem.0c00367.

[53] A. Müller, C. Fessele, F. Zuber, M. Rottmar, K. Maniura-Weber, Q. Ren, A.G. Guex, Gallium complex-functionalized P4HB fibers: a trojan horse to fight bacterial infection, ACS Appl. Bio Mater. 4 (2021) 682–691, doi:10.1021/acsabm.0c01221.

[54] O. Rzhepishevska, B. Ekstrand-Hammarström, M. Popp, E. Björn, A. Bucht, A. Sjöstedt, H. Antti, M. Ramstedt, The antibacterial activity of Ga3+ is influenced by ligand complexation as well as the bacterial carbon source, Antimicrob. Agents Chemother. 55 (2011) 5568–5580, doi:10.1128/AAC.00386-11.
[55] O. Olakanmi, B.E. Britigan, L.S. Schlesinger, Gallium disrupts iron metabolism of mycobacteria residing within human macrophages, Infect. Immun. 68 (2000) 5619–5627, doi:10.1128/IAI.68.10.5619-5627.2000.
[56] A.W. Wren, M.C. Jones, S.T. Misture, A. Coughlan, N.L. Keenan, M.R. Towler, M.M. Hall, A preliminary investigation into the structure, solubility and biocompatibility of solgel SiO2-CaO-Ga2O3 glass-ceramics, Mater. Chem. Phys. 148 (2014) 416–425, doi:10.1016/j.matchemphys.2014.08.006.
[57] Y. Kaneko, M. Thoendel, O. Olakanmi, B.E. Britigan, P.K. Singh, The transition metal gallium disrupts Pseudomonas aeruginosa iron metabolism and has antimicrobial and antibiofilm activity, J. Clin. Invest. 117 (2007) 877–888, doi:10.1172/JCI30783.
[58] A. Dubnika, D. Loca, V. Rudovica, M.B. Parekh, L. Berzina-Cimdina, Functionalized silver doped hydroxyapatite scaffolds for controlled simultaneous silver ion and drug delivery, Ceram. Int. 43 (2017) 3698–3705, doi:10.1016/j.ceramint.2016.11.214.
[59] H. Kim, S. Mondal, M.S. Moorthy, J. Oh, Optimized Zn-doped hydroxyapatite/Doxorubicin bioceramics system for efficient drug delivery and tissue engineering application, Ceram. Int. 44 (2018) 6062–6071, doi:10.1016/j.ceramint.2017.12.235.
[60] N. Strutynska, O. Livitska, S. Prylutska, Y. Yumyna, P. Zelena, L. Skivka, A. Malyshenko, L. Vovchenko, V. Strelchuk, Y. Prylutskyy, N. Slobodyanik, U. Ritter, New nanostructured apatite-type (Na+,Zn2+,CO3 2-)-doped calcium phosphates: preparation, mechanical properties and antibacterial activity, J. Mol. Struct. 1222 (2020) 128932, doi:10.1016/j.molstruc.2020.128932.
[61] V. Saxena, A. Hasan, L.M. Pandey, Effect of Zn/ZnO integration with hydroxyapatite: a review, Mater. Technol. 33 (2018) 79–92, doi:10.1080/10667857.2017.1377972.
[62] E. Boanini, M. Gazzano, A. Bigi, Ionic substitutions in calcium phosphates synthesized at low temperature, Acta Biomater. 6 (2010) 1882–1894, doi:10.1016/j.actbio.2009.12.041.
[63] M. Kurtjak, M. Vukomanović, D. Suvorov, Antibacterial nanocomposite of functionalized nanogold and gallium-doped hydroxyapatite, Mater. Lett. 193 (2017) 126–129, doi:10.1016/j.matlet.2017.01.092.
[64] P. Melnikov, A.R. Teixeira, A. Malzac, M. de B. Coelho, Gallium-containing hydroxyapatite for potential use in orthopedics, Mater. Chem. Phys. 117 (2009) 86–90, doi:10.1016/j.matchemphys.2009.05.046.
[65] C. Mellier, F. Fayon, F. Boukhechba, E. Verron, M. Leferrec, G. Montavon, J. Lesoeur, V. Schnitzler, D. Massiot, P. Janvier, O. Gauthier, J.M. Bouler, B. Bujoli, Design and properties of novel gallium-doped injectable apatitic cements, Acta Biomater. 24 (2015) 322–332, doi:10.1016/j.actbio.2015.05.027.
[66] C. Mellier, V. Schnitzler, P. Deniard, J.M. Bouler, B. Bujolic, P. Janvier, Gallium-doped β-tricalcium phosphate ceramics: characterization and properties, Key Eng. Mater. 493–494 (2012) 195–198, doi:10.4028/www.scientific.net/KEM.493-494.195.
[67] F. He, T. Lu, X. Fang, Y. Tian, Y. Li, F. Zuo, J. Ye, Modification of honeycomb bioceramic scaffolds for bone regeneration under the condition of excessive bone resorption, J. Biomed. Mater. Res. - Part A 107 (2019) 1314–1323, doi:10.1002/jbm.a.36644.
[68] M. Yang, J. Ren, R. Zhang, Novel gallium-doped amorphous calcium phosphate nanoparticles: preparation, application and structure study, J. Non. Cryst. Solids 466–467 (2017) 15–20, doi:10.1016/j.jnoncrysol.2017.03.034.
[69] N.A.S. Mohd Pu'ad, R.H. Abdul Haq, H. Mohd Noh, H.Z. Abdullah, M.I. Idris, T.C. Lee, Synthesis method of hydroxyapatite: a review, Mater. Today Proc. 29 (2019) 233–239, doi:10.1016/j.matpr.2020.05.536.
[70] K. Sakamoto, S. Yamaguchi, A. Nakahira, M. Kaneno, M. Okazaki, J. Ichihara, Y. Tsunawaki, J.C. Elliott, Shape-controlled synthesis of hydroxyapatite from α-tricalcium bis (orthophosphate) in organic-aqueous binary systems, J. Mater. Sci. 7 (2002) 1033–1041, doi:10.1023/A:1014316401945.
[71] Z. Hongquan, Y. Yuhua, W. Youfa, L. Shipu, Morphology and formation mechanism of hydroxyapatite whiskers from moderately acid solution, Mater. Res. 6 (2003) 111–115, doi:10.1590/s1516-14392003000100020.
[72] D.M. Liu, T. Troczynski, W.J. Tseng, Water-based sol-gel synthesis of hydroxyapatite: process development, Biomaterials 22 (2001) 1721–1730, doi:10.1016/S0142-9612(00)00332-X.
[73] K. Ishikawa, E. Garskaite, A. Kareiva, Sol–gel synthesis of calcium phosphate-based biomaterials—a review of environmentally benign, simple, and effective synthesis routes, J. Sol-Gel Sci. Technol. 94 (2020) 551–572, doi:10.1007/s10971-020-05245-8.
[74] V. Uskokovic, D.P. Uskokovic, Nanosized hydroxyapatite and other calcium phosphates: Chemistry of formation and application as drug and gene delivery agents, J. Biomed. Mater. Res. B Appl. Biomater. (2011) 96B, doi:10.1002/jbm.b.31746.
[75] L. Stipniece, A. Kondratjeva, K. Salma-Ancane, Influence of precursor characteristics on properties of porous calcium phosphate-titanium dioxide composite bioceramics, Ceram. Int. 46 (2020) 243–250, doi:10.1016/j.ceramint.2019.08.257.
[76] A. Szcześ, L. Hołysz, E. Chibowski, Synthesis of hydroxyapatite for biomedical applications, Adv. Colloid Interface Sci. 249 (2017) 321–330, doi:10.1016/j.cis.2017.04.007.
[77] P. Melnikov, M. de Fatima Cepa Matos, A. Malzac, A. Rainho Teixeira, D.M. de Albuquerque, Evaluation of in vitro toxicity of hydroxyapatite doped with gallium, Mater. Lett. 253 (2019) 343–345, doi:10.1016/j.matlet.2019.06.095.
[78] J.A. Lessa, G.L. Parrilha, H. Beraldo, Gallium complexes as new promising metallodrug candidates, Inorg. Chim. Acta 393 (2012) 53–63, doi:10.1016/j.ica.2012.06.003.
[79] N. Gómez-Cerezo, E. Verron, V. Montouillout, F. Fayon, P. Lagadec, J.M. Bouler, B. Bujoli, D. Arcos, M. Vallet-Regí, The response of pre-osteoblasts and osteoclasts to gallium containing mesoporous bioactive glasses, Acta Biomater. 76 (2018) 333–343, doi:10.1016/j.actbio.2018.06.036.
[80] D. Moreno, F. Vargas, J. Ruiz, M.E. López, Solid-state synthesis of alpha tricalcium phosphate for cements used in biomedical applications, Bol. La Soc. Esp. Ceram. y Vidr. 59 (2020) 193–200, doi:10.1016/j.bsecv.2019.11.004.
[81] I.E. Nifant, V.K. Besprozvannykh, A.V Shlyakhtin, A.N. Tavtorkin, M.P. Smirnova, S. Levin, P.V Ivchenko, Simple, efficient and reliable method for the preparation of b -tricalcium phosphate, Ital. Oral Surg. 31 (2021) 379–381, doi:10.1016/j.mencom.2021.04.032.
[82] C. Mellier, F. Fayon, V. Schnitzler, P. Deniard, M. Allix, S. Quillard, D. Massiot, J.M. Bouler, B. Bujoli, P. Janvier, Characterization and properties of novel gallium-doped calcium phosphate ceramics, Inorg. Chem. 50 (2011) 8252–8260, doi:10.1021/ic2007777.
[83] K. Lin, J. Chang, Structure and Properties of Hydroxyapatite for Biomedical Applications, Elsevier Ltd., 2015, doi:10.1016/b978-1-78242-033-0.00001-8.
[84] S.V Dorozhkin, Calcium orthophosphates (CaPO4): occurrence and properties, Prog. Biomater. 5 (2016) 9–70, doi:10.1007/s40204-015-0045-z.
[85] G. Ma, X.Y. Liu, Hydroxyapatite: Hexagonal or monoclinic? Cryst. Growth Des. 9 (2009) 2991–2994, doi:10.1021/cg900156w.
[86] E. Pramatarova, L. Pecheva, Modified inorganic surfaces as a model for hydroxyapatite growth, Trans Tech Publications Limited, Switzerland (2006) 122.
[87] R.S. Bockman, A.L. Boskey, N.C. Blumenthal, N.W. Alcock, R.P. Warrell, Gallium increases bone calcium and crystallite perfection of hydroxyapatite, Calcif. Tissue Int. 39 (1986) 376–381, doi:10.1007/BF02555174.
[88] R. Donnelly, A. Boskey, The effect of gallium on seeded hydroxyapatite growth, Calcif. Tissue Int. 44 (1989) 138–142, doi:10.1007/BF02556473.
[89] M. Kurtjak, M. Vukomanović, L. Kramer, D. Suvorov, Biocompatible nanogallium/hydroxyapatite nanocomposite with antimicrobial activity, J. Mater. Sci. Mater. Med. 27 (2016), doi:10.1007/s10856-016-5777-3.
[90] M. Bohner, B.L.G. Santoni, N. Döbelin, β-tricalcium phosphate for bone substitution: synthesis and properties, Acta Biomater. 113 (2020) 23–41, doi:10.1016/j.actbio.2020.06.022.
[91] R.G. Carrodeguas, S. De Aza, α-Tricalcium phosphate: synthesis, properties and biomedical applications, Acta Biomater. 7 (2011) 3536–3546, doi:10.1016/j.actbio.2011.06.019.
[92] X. Yin, M.J. Stott, A. Rubio, α- and β-tricalcium phosphate: a density functional study, Phys. Rev. B - Condens. Matter Mater. Phys. 68 (2003) 1–8, doi:10.1103/PhysRevB.68.205205.
[93] E. Boanini, M. Gazzano, C. Nervi, M.R. Chierotti, K. Rubini, R. Gobetto, A. Bigi, Strontium and zinc substitution in β-tricalcium phosphate: an X-ray diffraction, solid state NMR and ATR-FTIR study, J. Funct. Biomater. 10 (2019), doi:10.3390/jfb10020020.
[94] P.N. Kumar, S.K. Mishra, S. Kannan, Probing the limit of magnesium uptake by β-tricalcium phosphate in biphasic mixtures formed from calcium deficient apatites, J. Solid State Chem. 231 (2015) 13–19, doi:10.1016/j.jssc.2015.07.051.
[95] A.L. Boskey, A.S. Posner, Conversion of amorphous calcium phosphate to microcrystalline hydroxyapatite. A pH-dependent, solution-mediated, solid-solid conversion, J. Phys. Chem. 77 (1973) 2313–2317, doi:10.1021/j100638a011.
[96] D. Rabadjieva, R. Gergulova, R. Titorenkova, S. Tepavitcharova, E. Dyulgerova, C. Balarew, O. Petrov, Biomimetic transformations of amorphous calcium phosphate: kinetic and thermodynamic studies, J. Mater. Sci. Mater. Med. 21 (2010) 2501–2509, doi:10.1007/s10856-010-4103-8.
[97] S. Somrani, M. Banu, M. Jemal, C. Rey, Physico-chemical and thermochemical studies of the hydrolytic conversion of amorphous tricalcium phosphate into apatite, J. Solid State Chem. 178 (2005) 1337–1348, doi:10.1016/j.jssc.2004.11.029.

Appendix II

Insights into physicochemical properties, stability in various aqueous media, and antibacterial activity of gallium-containing amorphous calcium phosphates

Renats Vasiljevs, Marika Sceglova, Liga Stipniece, Janis Locs

Scientific Reports, **2025**, 15, 26976. Doi: 10.1038/s41598-025-12906-7

M.S. input: conceptualization, data curation, formal analysis, reviewing and editing.

scientific reports

Check for updates

OPEN

Insights into physicochemical properties, stability in various aqueous media, and antibacterial activity of gallium-containing amorphous calcium phosphates

Renats Vasiljevs[1,2], Marika Sceglova[1,2]✉, Liga Stipniece[1,2]✉ & Janis Locs[1,2]

Amorphous calcium phosphate (ACP) is a metastable phase that spontaneously crystallizes upon contact with aqueous media. Furthermore, modification of ACP with metal ions to confer specific biological functions may affect its stability. Crystallization of ACP is accompanied by physicochemical changes, which affect its biological properties. In this study, ACP powders with Ga content up to 2.2 ± 0.2 wt% were synthesized using a modified wet precipitation method. The synthesized powders' phase composition, functional groups, and morphology were analyzed. Overall, adding up to 2.2 ± 0.2 wt% of Ga had a negligible effect on the ACP physicochemical properties. The Ga-containing ACP (GaACP) stability was evaluated in deionized H_2O, phosphate buffer solution (PBS), Dulbecco's modified Eagle's medium (DMEM), and tryptone soya broth (TSB). The Ga content and the composition of the incubation media affected the stability of the GaACP powders. The most stable GaACP powders were in deionized H_2O (reached 90 min), but the least stable were in PBS. Moreover, increasing the Ga content in ACP improved the powder stability in DMEM and TSB. The antibacterial activity of the synthesized powders was assessed against *Pseudomonas aeruginosa* and *Staphylococcus aureus*. It was confirmed that incorporating Ga into ACP may confer inhibitory potential on bacterial growth.

Keywords Amorphous calcium phosphate, Gallium, Crystallization, Nanoparticles, Antibacterial properties

Bone tissue has the inherent ability to self-repair after injuries or traumas. However, critical-sized lesions combined with chronic diseases, such as osteoporosis, often suppress the ability of bone tissue to regenerate itself, leading to the necessity for additional treatment[1]. Various transplantation methods (autograft, allograft, and xenograft) are widely used to replace bone tissue. Still, their practical application is limited due to a confined amount of available material for transplantation, the need for secondary surgical operation (longer surgery time, greater blood loss, increased amount of pain for autograft), and a higher risk of bacterial infection and inflammation. Consequently, the development of various synthetic biomaterials and the possibilities of their application in bone tissue regeneration are increasingly being studied[2–7].

Among various synthetic biomaterials for bone regeneration, calcium phosphates (CaPs) are widely used due to their similarity to bone tissue's chemical composition and structure[2,4,6–8]. Amorphous calcium phosphate (ACP) has attracted significant interest as a promising third-generation biomaterial for bone regeneration due to its unique properties. It is characterized by high solubility, ensuring a higher rate of resorption in the body and a faster release of ions than more stable CaPs[9,10]. Despite ACP's excellent biological properties (e.g., osteoconductivity and biodegradability), its practical application is challenging. The most important complication is the tendency of ACP to crystallize spontaneously and transform into other CaP phases in an aqueous medium[11,12]. However, the properties of ACP can be modified with incorporated vicarious metal ions, which could improve its stability in contact with the body's internal environment, and whose release after implantation would inhibit the reproduction of bacteria at the implantation site[13]. Due to their antibacterial properties, the modification of CaPs' properties using gallium (III) (Ga^{3+}) ions has received increased attention in recent years[14–16]. Furthermore, Ga^{3+} has a specific biological effect on bones, namely, it exhibits a dose-

[1]Faculty of Natural Sciences and Technology, Institute of Biomaterials and Bioengineering, Riga Technical University, Paula Valdena Street 3-K1, Riga, Latvia. [2]Baltic Biomaterials Centre of Excellence, Headquarters at Riga Technical University, Riga, Latvia. ✉email: marika.sceglova@rtu.lv; liga.stipniece@rtu.lv

dependent antiosteoclastic effect by reducing osteoclast differentiation and formation, thus inhibiting bone resorption[17]. However, only a few studies that evaluate the effect of Ga^{3+} ion addition specifically on ACP are available in the scientific literature. *Yang et al.* have substituted ACP with Ga^{3+} ions (where the (Ca + Ga)/P molar ratio ranges from 1.8 to 3.0) using the sol-gel method. In this study, it was found that a rapid release of Ga^{3+} ions occurred during the first 24 h. Furthermore, increasing the molar ratio of (Ca + Ga)/P in the GaACP inhibited the growth of *P. aeruginosa* bacteria[18].

Given the metastable nature of ACP, any modification can significantly affect its properties. Therefore, it is essential to determine if and how the addition of Ga^{3+} ions will affect ACP's physicochemical properties, including stability. For the first time, this study evaluated the effect of Ga^{3+} ions and the composition of aqueous media on the stability of ACP. Biologically relevant media, such as cell culture media (*Dulbecco's* modified *Eagle* medium (DMEM)) and microbial culture media (tryptone soya broth (TSB)), were used to gain insight into the in vitro stability of the Ga-containing ACP (GaACP) when compared with dissolution in standard buffer solution, i.e., phosphate-buffered saline (PBS), or deionized (DI) H_2O. Additionally, the antibacterial activity of GaACP powders was tested against *Pseudomonas aeruginosa* (*P. aeruginosa)* and *Staphylococcus aureus (S. aureus)*.

Materials and methods

Synthesis of gallium-containing amorphous calcium phosphate powders

GaACP powders were synthesized via modified wet chemical precipitation method using $CaCl_2{\cdot}2H_2O$ (Ph Eur, BP, JP, USP grade, *Merck*, Germany), $Ga(NO_3)_3{\cdot}9.5H_2O$ (99.9% trace metal, *Sigma-Aldrich*, USA) and H_3PO_4 (75%, *Latvijas ķīmija*, Latvia) as Ca^{2+}, Ga^{3+} and PO_4^{3-} ion precursors, respectively, and NaOH (purity ≥ 98%, *Merck*, Germany) as pH adjuster as shown in Fig. 1(A).

The syntheses were carried out in glass beakers at ambient temperature (20 ± 2 °C) under continuous stirring with a laboratory electromechanical stirrer. First, 3 M $CaCl_2$, 0.4 M $Ga(NO_3)_3$, 2M H_3PO_4, and 3 M NaOH aqueous solutions were prepared from $CaCl_2{\cdot}2H_2O$, $Ga(NO_3)_3{\cdot}9.5H_2O$, H_3PO_4, and NaOH, respectively. Then, determined amounts (Table S1, Supplementary Information) of the 3 M $CaCl_2$, 0.4 M $Ga(NO_3)_3$, and 2M H_3PO_4 aqueous solutions were added to 300 mL of deionized water (DI H_2O), and, thus, the starting Ca^{2+}, Ga^{3+}, and PO_4^{3-} ions-containing solution was obtained. The (Ca + Ga)/P molar ratio of 1.67 of the reagents was the same for all syntheses. Next, 3 M NaOH was rapidly added to the Ca^{2+}, Ga^{3+}, and PO_4^{3-} ions-containing solution under vigorous stirring (500 rpm), which rapidly increased the pH and induced the precipitation of the GaACP. Finally, the pH of the reaction mixtures was adjusted by adding 3 M NaOH until the pH reached 10.3 ± 0.2. The amount of the 3 M NaOH solution used for each synthesis series is given in Table S1 (Supplementary Information). The obtained suspensions were processed as shown in Fig. 1(B). Briefly, the suspensions were centrifuged (3000 rpm, 3 min), and the precipitates were rinsed with DI H_2O (four times) until no NaCl was detected in the supernatant using 0.1 M $AgNO_3$. Finally, the NaCl-free precipitates were frozen in liquid nitrogen for 15 min and freeze-

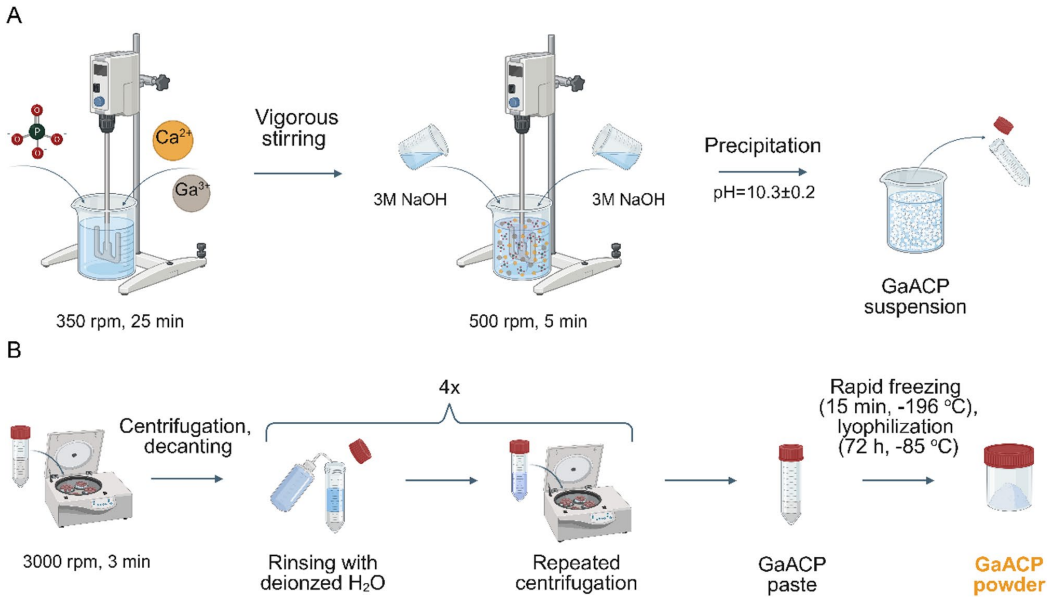

Fig. 1. Scheme of the synthesis procedure: (**A**) – wet chemical precipitation, (**B**) – precipitate processing (created using *BioRender.com*).

dried (-85 °C) for 72 h. At least three replicates of the synthesis were performed for each Ga content to ensure the reproducibility of the synthesis technology.

Physicochemical characterization

Inductively coupled plasma mass spectrometry

Ga content in the synthesized powders was measured using inductively coupled plasma mass spectrometry (ICP-MS; 7700X, *Agilent*, USA). The powders were dissolved in DI H_2O (*Synergy 185*, *Millipore*, MA, USA) and high-purity HNO_3 (65%, *ChemLab*, Belgium) solution. The resulting solutions were kept at room temperature for at least 20 min, then subjected to microwave exposure at 150 °C for 30 min (temperature raising rate 5 °C/min) to facilitate the complete dissolution of the solid particles. The obtained solutions were cooled and filtered through a filter with a pore size of 12–15 μm to eliminate solid phase impurities. Three replicates for each synthesis series were analyzed, and the average values and standard deviations were calculated.

Powder X-ray diffraction

Phase composition of the synthesized and incubated powders (i.e., the powders after stability tests) was analyzed using powder X-ray diffractometry (XRD; *Aeris*, *Malvern PANalytical*, the Netherlands). XRD patterns were acquired using Cu K_α X-rays produced at 40 kV and 15 mA. Diffraction data were recorded with a 2θ scan range from 10° to 70°; with a step size 0.0435° and time per step of 0.64 s. The phases present in the XRD patterns were identified using the *Profex* software[19].

Fourier-transform infrared spectroscopy

Fourier-transform infrared spectroscopy (FTIR; *Nicolet iS50*, *Thermo Fisher Scientific*, USA) in Attenuated Total Reflectance (ATR) mode was employed to analyze the functional groups of the synthesized powders. ATR-FTIR spectra were collected in the wavenumber range between 4000 and 400 cm^{-1} with a resolution of 4 cm^{-1} by co-adding 64 scans. Before each measurement, a background spectrum (64 scans) was collected and then subtracted from the sample spectrum.

N_2 gas adsorption (BET method)

The synthesized powders' specific surface area (SSA_{BET}) was determined from the N_2 adsorption isotherms produced at -196 °C using *QUADRASORB evo™* gas sorption analyzer (*Quantachrome Instruments*, USA). The Brunauer-Emmett-Teller (BET) mathematical model was applied to calculate SSA_{BET} in adsorbed gas relative pressure (P/P_0) range from 0.05 to 0.3. Before the analysis, the samples were degassed in an *AUTOSORB* degasser (*Quantachrome Instruments*, USA) at ambient temperature for 24 h to eliminate excess moisture and other volatile substances in the sample.

From the obtained SSA_{BET} values, the average particle sizes (d_{BET}, nm) were calculated according to Eq. 1 as described in ISO standard No. 13779-3 "Implants for surgery Hydroxyapatite Part 3: Chemical analysis and characterization of crystallinity and phase purity", assuming that all particles are non-porous and spherical:

$$d_{BET} = \frac{6}{\rho_{PYC} \cdot SSA_{BET}} \quad (1)$$

where ρ_{PYC} - a true density (g/cm³, determined by helium pycnometer as described in Sect. He pycnometry) of the synthesized powders.

He pycnometry

True density (ρ_{PYC}) of the synthesized powders was determined using He pycnometry (PYC; *Micro UltraPyc 1200e*, *Quantachrome Instruments*, USA). Before the measurements, the pycnometer was calibrated with stainless steel spheres of known volume. After the calibration, the volume of the sample was determined by pressurizing it with helium gas to a target pressure of 10 psig (30 pulses). Measurements were performed until the standard deviation of 5 consecutive measurements for one sample did not exceed 0.1%. The true density was calculated by dividing the sample's mass by the measured sample volume.

Scanning transmission electron microscopy

Morphology of the synthesized powders was analyzed using a scanning electron microscopy (SEM; *Verios 5 UC*, *Thermo Fisher Scientific*, USA) coupled with a scanning transmission electron microscopy (STEM) detector. Before STEM measurements, the synthesized powders were dispersed in absolute ethanol, transferred to a lacey carbon support film on a copper grid (22-1MLC20, *Micro to Nano*, the Netherlands), and dried at 40 °C overnight to evaporate the ethanol. Bright-field mode was used to acquire STEM images. Transmitted electrons generated at an acceleration voltage of 20 kV were detected.

Stability tests

Stability of the synthesized GaACP powders was evaluated in different aqueous media, i.e., DI H_2O, PBS, DMEM, and TSB. Stability studies included preparing incubation media, sample incubation, and characterization.

Incubation media Preparation

The DI H_2O with a conductivity of 0.055 μS was produced by *Adrona Crystal E* (Riga, Latvia) and used as produced.

The PBS solution was prepared according to the manufacturer's instructions by dissolving one PBS tablet (P4417, *Sigma-Aldrich*, USA) in 200 mL of DI H_2O.

To obtain 1 L of DMEM solution, 13.5 g of DMEM powder (without $NaHCO_3$, *Gibco*, USA) was dissolved in DI H_2O, then 13.5 g of $NaHCO_3$ (≥99,7%, *Sigma-Aldrich*, USA) and 0.63 g of preservative NaN_3 (≥99.5%, *Sigma-Aldrich*, USA) were added. The pH of the solution was adjusted to 7.1 ± 0.1 using 3 M NaOH solution.

The TSB solution was prepared by dissolving 30 g of TSB powder (*Oxoid*, Switzerland) in 1000 mL of DI H_2O. Detailed information on the chemical composition of all incubation media (PBS, DMEM, and TSB) is provided in Table S2 (Supplementary Information).

Sample incubation

The incubation of the samples is schematically shown in Fig. 2(A). Briefly, 0.15 g of the lyophilized GaACP powder was suspended in 25 mL of preheated media (37 °C) and placed in an incubator-shaker (*Biosan*, Latvia) at 37 °C and orbital shaking (80 rpm). The powder and the volume of liquid incubation media ratio of 6 mg/mL was constant for all variations. The incubation times of the samples were 20, 40, 60, 90 min, and 4, 24, 48 h.

After the respective incubation time, the samples were processed, as shown in Fig. 2(B). The samples were centrifuged at 3000 rpm for 1 min, decanted, sequentially rinsed with ethanol, centrifuged, rinsed with DI H_2O, centrifuged again, and decanted. After rinsing, the samples (sediments) were frozen in liquid nitrogen for 15 min and lyophilized (-85 °C, 72 h). The obtained powders were analyzed for phase composition using XRD.

Antibacterial tests

The antibacterial properties of the synthesized GaACP powders were determined against two bacterial species, i.e., Gram-negative *P. aeruginosa* (strain ATCC 23863) and Gram-positive *S. aureus* (strain ATCC 25923). Both bacterial species were recovered from frozen stocks (− 20 °C in 20% (v/v) glycerol) and cultured in TSB overnight in ambient air at 37 ∘C and agitation at 80 rpm. The overnight culture was then diluted with TSB to an optical density (OD) of 0.1 at 620 nm ($1{\cdot}10^6$ colony-forming units (CFU)/mL).

Before antibacterial experiments, the powders were disinfected in absolute ethanol for approximately 2 h (until ethanol fully evaporates). Afterwards, the GaACP powders were suspended in TSB at concentrations of 1, 2, and 4 mg/mL. A total of 300 µL of the suspension was transferred to a 96-well plate, and 5 µL (OD_{620} = 0.1) of bacteria was added to each well. Bacterial growth (OD_{620}) was measured for 20 h at 37 °C in a plate reader (*MultiskanGo*, *Thermo Scientific*, USA).

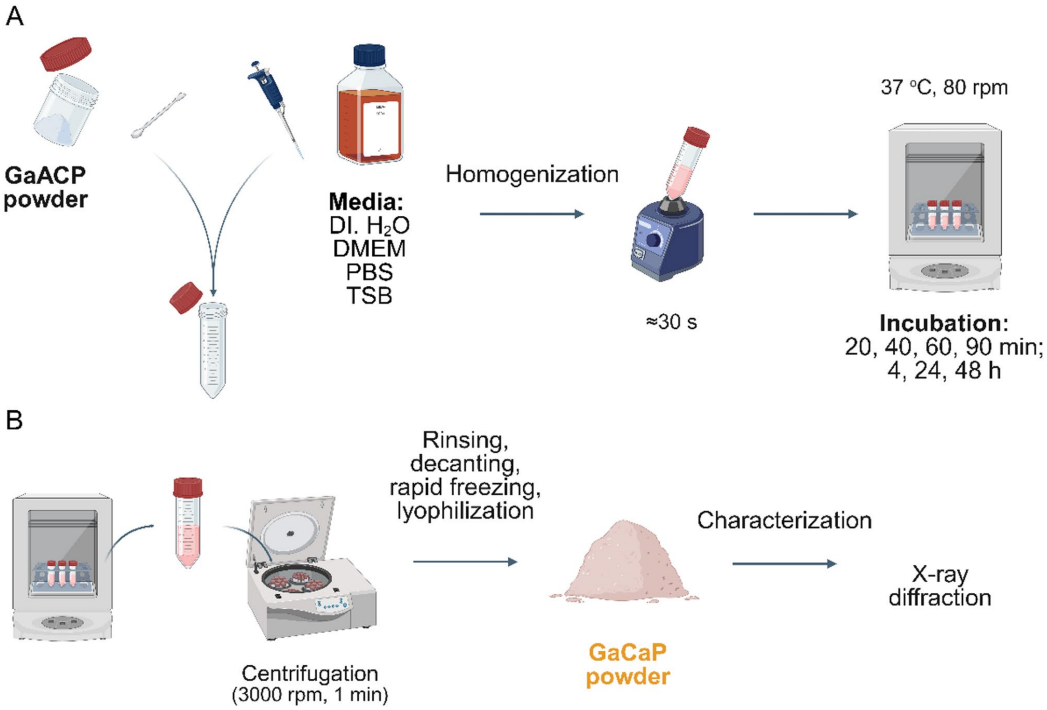

Fig. 2. Schematic diagram of stability tests: (**A**) – sample preparation for incubation and incubation conditions, (**B**) – processing of samples after incubation (created using *BioRender.com*).

Sample series	Ga content (wt% from the total product yield)		SSA_{BET}, m^2/g	d_{BET}, nm	ρ_{PYC}, g/cm^3
	Nominal	Measured			
Ref-ACP	0	-	167 ± 4	14 ± 1	2.50 ± 0.02
2GaACP	2	0.6 ± 0.1	159 ± 5	15 ± 1	2.54 ± 0.06
4GaACP	4	1.3 ± 0.2	151 ± 7	16 ± 1	2.49 ± 0.05
6GaACP	6	1.7 ± 0.1	163 ± 1	15 ± 1	2.47 ± 0.02
12GaACP	12	2.2 ± 0.1	165 ± 18	15 ± 2	2.48 ± 0.04

Table 1. Designation, nominal and measured (using ICP-MS) Ga content, and morphological characteristics of the synthesized powders.

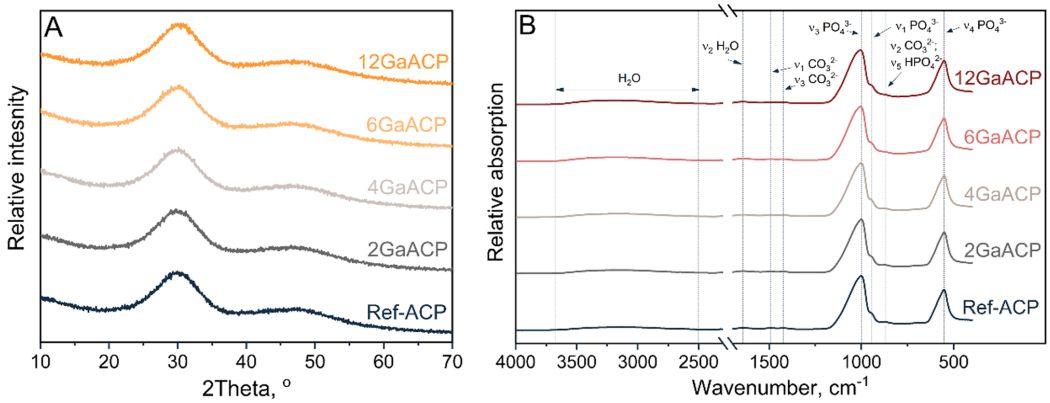

Fig. 3. (**A**) – XRD patterns and (**B**) – ATR-FTIR spectra of the synthesized powders.

Results and discussion

Physicochemical properties of gallium-containing amorphous calcium phosphate powders

The Ga content in the synthesized GaACP powders was determined using ICP-MS, and the results are summarized in Table 1.

The ICP-MS results showed that the Ga content in the synthesized powders increased with the amount of Ga precursor ($Ga(NO_3)_3 \cdot 9.5H_2O$) in the synthesis medium. However, the Ga content in the synthesized powders was significantly lower than the expected or nominal. This indicates that a large portion of in the synthesis media dissociated Ga^{3+} ions did not participate in the precipitation reaction and were decanted with the liquid synthesis medium during precipitate processing. Considering the above, it can be concluded that the Ga content of 2.2 ± 0.1 wt% obtained by increasing the nominal content of Ga in the synthesis medium to 12 wt% is close to the maximal possible incorporation level in the given conditions. Still, according to *Mosina* et al.'s studies on the biological properties of the Ga-substituted HAp nanoparticles, this amount falls within the optimal Ga content range (2.0–5.5 (± 0.1) wt%), which shows antibacterial properties and maintains appropriate cell viability[16].

The XRD patterns shown in Fig. 3(A) were used to evaluate the effect of Ga on the ACP's crystallinity and phase purity.

Regardless of the Ga content, the synthesized powders were X-ray amorphous, i.e., they do not have the long-range configurational order characteristic of materials with a high degree of crystallinity. This was confirmed by the broad diffraction maxima characteristic of ACP, of which the peak with the highest intensity was centred at 30° 2θ[9,10,20]. The $CaCl_2 \cdot 2H_2O$ used in the synthesis could form NaCl with NaOH, and $Ga(NO_3)_3 \cdot 9.5H_2O$ could form $NaNO_3$ with NaOH. These by-products must not be in the synthesis products. Therefore, the precipitates were rinsed as shown in Fig. 1(B). Since the characteristic XRD peaks of the mentioned crystalline by-products, i.e., NaCl or $NaNO_3$, were not observed, the efficiency of the used precipitate processing (rinsing) was approved.

The ATR-FTIR spectra shown in Fig. 3(B) were used to evaluate the effect of Ga on the ACP's functional groups. The ATR-FTIR spectra of the synthesized powders correlated with the literature data. Absorbance bands of functional group vibrations characteristic of the ACP phase were detected. The broad absorbance bands maxima at 552, 950, and 1000 cm^{-1} characteristic of phosphate groups (ν_4 PO_4^{3-}, ν_1 PO_4^{3-}, and ν_3 PO_4^{3-}) confirmed the non-crystalline nature of the synthesized powders[21–23]. According to the literature, ACP particles' most minor structural units are the so-called *Posner* clusters (neutral ion clusters)[9,10,12,22,24]. The absorbance band maximum at 1640 cm^{-1} and broad absorbance band in the region 2500–3700 cm^{-1} indicate the presence

of structurally bound (intercluster) and surface adsorbed water in the synthesized powders, respectively[9,22]. All synthesized powders contained carbonate ions (CO_3^{2-}), as indicated by a doublet of low-intensity absorbance bands at 1420 and 1490 cm^{-1}. The incorporation of CO_3^{2-} ions in the synthesized powders can be explained by the dissolution of atmospheric CO_2 in the synthesis medium, facilitated by continuous and rapid stirring of the reaction mixture[21–23]. Regardless of the Ga content, the ATR-FTIR spectra of the synthesized powders were similar. Thus, Ga content had a negligible effect on the absorbance bands' position and appearance (width and intensity).

The SSA_{BET} and ρ_{PYC} of the synthesized powders were determined using N_2 sorption and He pycnometry, respectively, and average values of d_{BET} were calculated. The obtained results are summarized in Table 1. Regardless of the Ga content, nano-sized particles with a relatively high SSA_{BET} were obtained. The measured SSA_{BET} values correlated with data available on the ACP obtained by the dissolution-recrystallization method[25].

STEM microphotographs were acquired to visualize the particle morphology of the synthesized powders (Fig. 4).

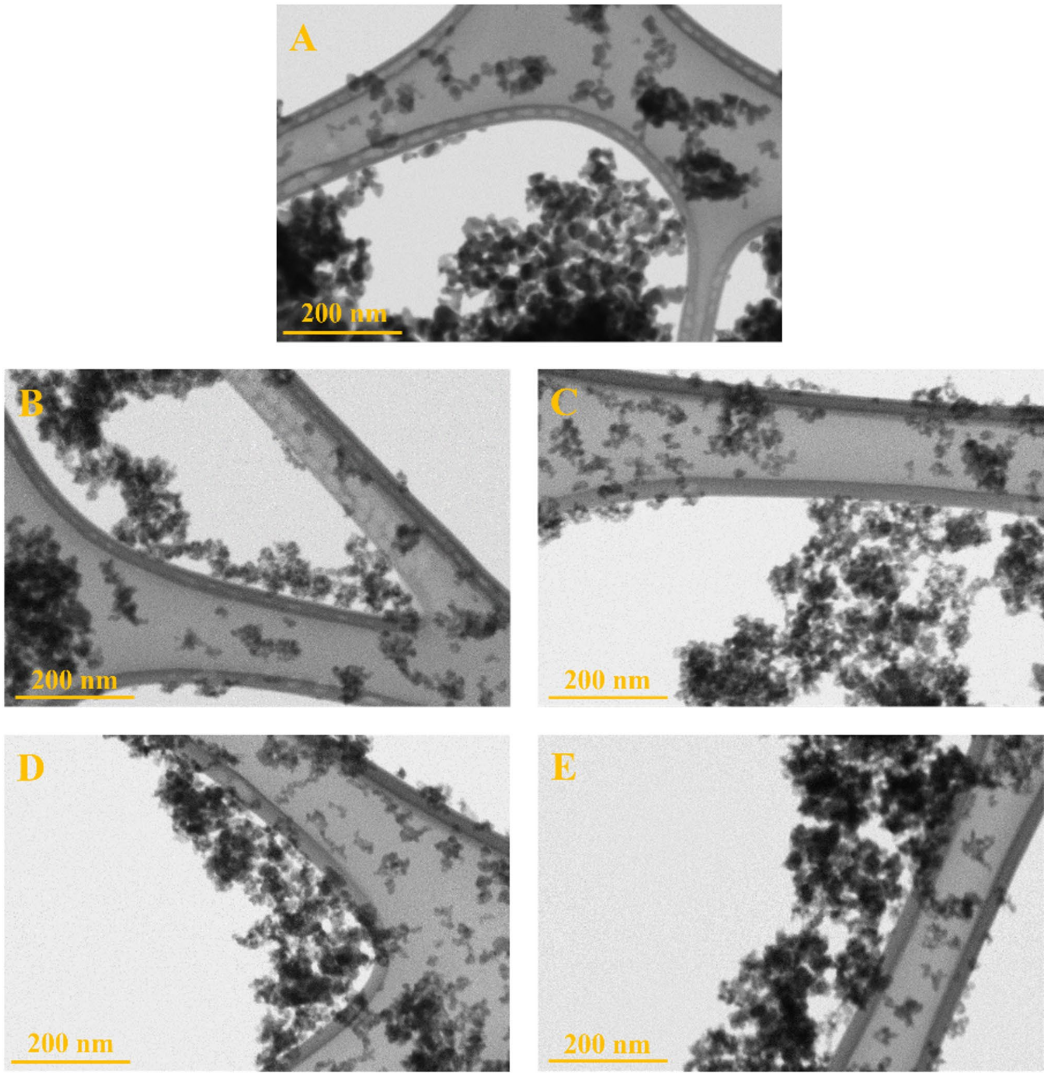

Fig. 4. STEM images of the synthesized powders: (**A**) – Ref-ACP, (**B**) – 2GaACP, (**C**) – 4GaACP, (**D**) – 6GaACP, and (**E**) – 12GaACP.

STEM images confirmed that the Ref-ACP and GaACP powders consist of spheroidal particles with sizes on the order of a few tens of nanometres, regardless of the Ga content. Results from acquired STEM images align with equivalent average primary particle diameters calculated by Eq. 1 (Table 1). However, precise measurements using STEM are challenging due to the electron-beam sensitivity of ACP, which undergoes crystallization upon intense electron beam exposure[26,27]. In addition, it was observed that the primary particles tend to form irregular shapes or branched chain aggregates, which aligns with the observations about ACP morphology reported in the literature[21–23,28–30]. The formation of agglomerates and branched chain structures could be attributed to the sample preparation, particularly drying conditions and the solvents used for synthesis and sample preparation[23,31]. During the removal of the last solvent layers, drying causes capillary bridges to form, resulting in irreversible aggregation due to solid-solid contacts formed under capillary pressure[32,33]. Moreover, without a supporting surface, hydrated ACP aggregates tend to shrink into clustered or chain-like spheroidal assemblies to minimize the air-solid interface energy[28,33]. Also, it is worth mentioning that different surface interactions (e.g., bridging hydrogen bonds) between neighbouring nanoparticles play an important role in nanoparticle agglomeration[33].

Stability of gallium-containing amorphous calcium phosphate powders in different aqueous media

The in vitro stability of the Ref-ACP and GaACP powders was evaluated in the DI H_2O (for control experiments), PBS (for assessing the effect of inorganic ions), DMEM, and TSB (for evaluating the impact of complex inorganic and organic substances simultaneously). The XRD patterns of the powders after incubation in the DMEM at different time points are shown in Fig. 5 (in DI H_2O - Fig. S1, Supplementary Information, in PBS - Fig. S2, Supplementary Information, in TSB - Fig. S3, Supplementary Information).

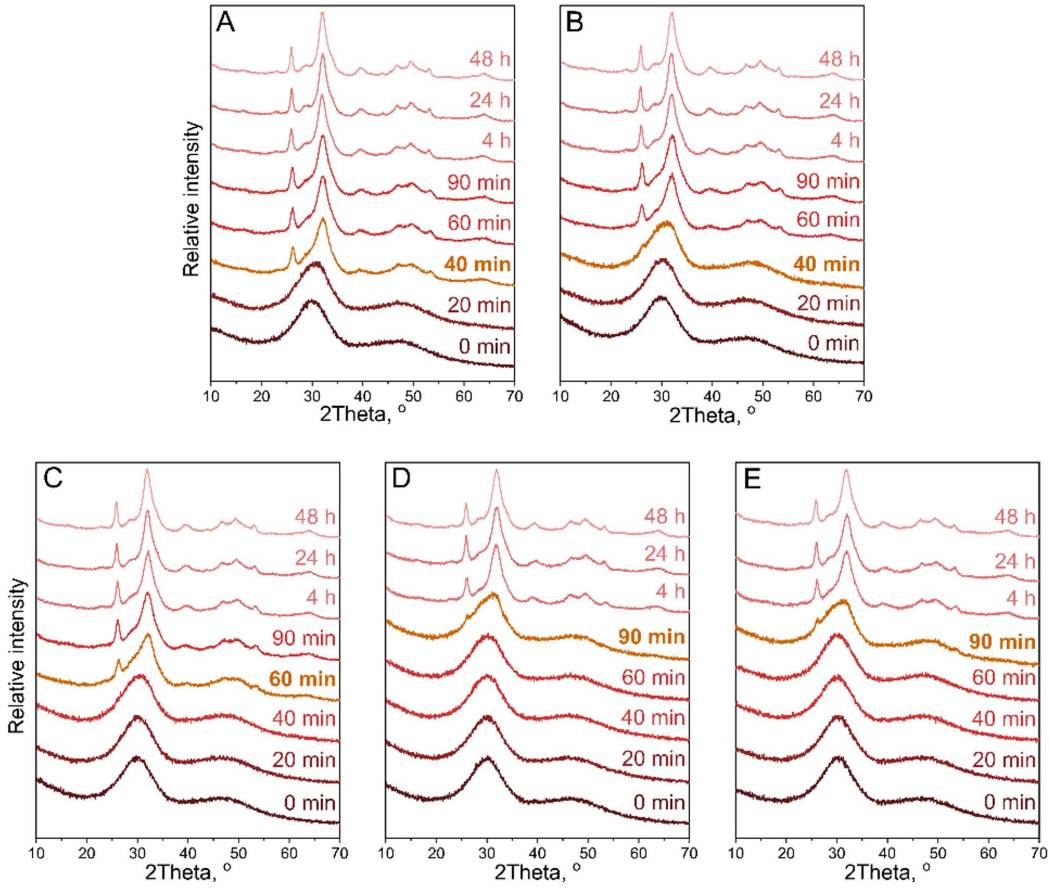

Fig. 5. The XRD patterns of the (**A**) - Ref-ACP, (**B**) – 2GaACP, (**C**) – 4GaACP, (**D**) – 6GaACP, and (**E**) – 12GaACP powders after incubation in DMEM.

The XRD results showed that the phase composition and the crystallinity of all samples subjected to in vitro stability tests altered over time, as evidenced by the formation and narrowing of diffraction maxima characteristic of the apatitic CaP phase at 26° and 32° 2θ[34]. After 48 h of incubation, all samples were converted to carbonated partially crystalline calcium deficient HAp (CDHAp) as evidenced by ATR-FTIR spectra (Fig. S4, Supplementary Information), which mimics the inorganic phase of bone tissue[9,10,12,27,34–36].

The stability time of powders in different aqueous media was determined and summarized in Table 2.

In general, the stability time of the Ref-ACP was short, as indicated by fast crystallization in DI H_2O, PBS, DMEM, and TSB. According to existing literature, pure ACP is stable in aqueous media for at least several hours at room temperature, depending on the chemical composition of the incubation media[26,34,37,38]. However, the relatively fast crystallization under the conditions used in this study could be explained by the high SSA_{BET} of the synthesized powders (Table 1) and the incubation temperature (37 °C), which enhances release of Ca^{2+} and PO_4^{3-} ions and their redeposition on the particles' surface and thus promotes phase transformation[10,39,40].

The most pronounced influence on the stability of the synthesized powders was observed from the composition of the aqueous incubation media and the Ga content in the powders.

The most rapid ACP crystallization was observed in the PBS, which aligns with findings reported in the literature[26,41]. The accelerated transformation in PBS could be explained by the predominance of phosphate ions (Table S2, Supplementary Information), which accelerates the nucleation and growth of new particles through complementary dissolution-recrystallization and solution-mediated solid-solid transformation mechanisms[28,30,42,43]. Moreover, high concentration of free phosphate ions in PBS with respect to the concentration of Ga^{3+} ions incorporated in samples might suppress the stabilizing effect of Ga. Consequently, Ga had a minimal effect on the stability of ACP in PBS. The 2GaACP was stable for 20 min. Still, by increasing the Ga content in ACP, the induction period began to decrease, and the stability of these samples was similar to that of the Ref-ACP in PBS. Additionally, it is worth mentioning that there might be a decrease in pH of the medium because of Ga^{3+} hydrolysis, which reduces the stability of ACP and promotes the nucleation of crystalline CaP phases[44].

The stability of the powders in DMEM and TSB was notably higher than that in PBS. This enhanced stability is likely due to various organic molecules in DMEM and TSB (Table S2, Supplementary Information) that can interact with ACP, thereby influencing its crystallization behaviour. Moreover, scientific literature has reported that the crystallization rate of ACP depends on the type of organic molecules and their concentration[26,40,45]. DMEM is a relatively complex cell culture medium containing a high concentration of various amino acids, vitamins, and inorganic salts, including calcium and phosphate ions (Table S2), Supplementary Information). While specific components, such as carbonate ions, can stabilize ACP through incorporation into the structure, other constituents, like phosphate ions or small organic molecules, promote its crystallization[26,46]. In general, organic molecules in aqueous media can affect ACP stability through various possible mechanisms, including adsorption onto ACP nanoparticles' surface, chelation of free calcium or phosphate ions, and interactions between phosphate and carboxylate groups present in amino acids[26,47]. These interactions can either inhibit or promote crystallization[37]. Inorganic ions present in the media may adsorb on the surface of ACP nanoparticles, thus facilitating the ion exchange process and fostering the formation of the apatite layer or potentially influencing nucleation sites, directing the crystallization pathway of ACP[46]. Additionally, DMEM in our experiments was supplemented with $NaHCO_3$. Thus, introduced carbonate ions can incorporate into the ACP structure or precipitate as calcite, thereby stabilizing the ACP[9,12,26,48,49] (ATR-FTIR spectra in Fig. S4(C), Supplementary Information). However, the pH of DMEM (supplemented with $NaHCO_3$) increases in ambient air and requires a CO_2 environmental atmosphere to maintain physiological pH[50]. In our study, a CO_2 atmosphere was not provided for the stability tests; thus, the influence of pH changes on the stability cannot be ruled out. According to the scientific literature, ACP is more stable at physiological conditions (pH ≈ 7.4) than at alkaline conditions (pH > 7.4)[51]. However, we cannot unequivocally state the stability of the powders under cell assay conditions (pH ≈ 7.2–7.4 with 5% CO_2); they are expected to be stable for an even more extended period than the 60 min observed in our stability tests.

The enhanced stability of ACP in TSB could be attributed to its high protein content (Table S2, Supplementary Information). Notably, casein-derived phosphopeptides are well documented for their ability to stabilize CaPs by several concentration-dependent mechanisms, i.e., adsorbing proteins on CaPs particles' surface due to high affinity, electrostatic interactions, and by chelating calcium ions, therefore sterically hindering crystal growth[37,52–54]. In this study, ATR-FTIR spectra of the samples incubated in TSB for 48 h (Fig. S4, Supplementary Information) indicate the presence of the Amide II band at 1545 cm^{-1}, suggesting the adsorption of proteins from the medium onto the surface of ACP particles[55,56].

Sample series	Incubation time, min			
	DI H_2O	PBS	DMEM	TSB
Ref-ACP	< 20	< 20	20	< 20
2GaACP	60	20	20	20
4GaACP	60	< 20	40	20
6GaACP	60	< 20	60	60
12GaACP	60	< 20	60	40

Table 2. Stability time of the synthesized powders in different aqueous media.

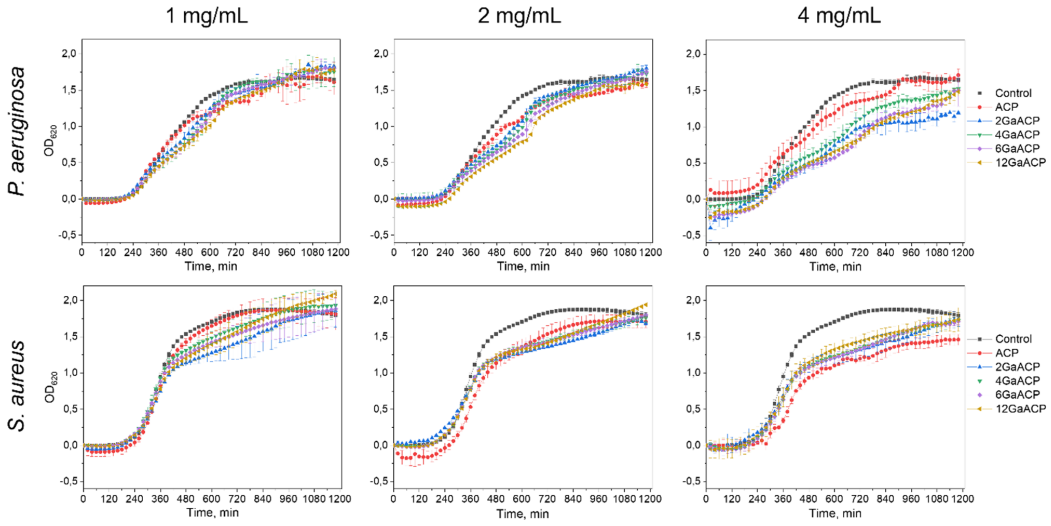

Fig. 6. Growth inhibition of *S. aureus* and *P. aeruginosa* induced by the GaACP powder suspensions in TSB media at 1 mg/mL, 2 mg/mL, and 4 mg/mL. The represented OD_{620} values were obtained by subtracting the initial OD_{620-0_h} (starting time = 0 h) from the measured OD_{620-x_h} at specific time points, i.e., x h.

In the DI H_2O, DMEM, and TSB, the GaACP powders were more stable than the Ref-ACP powders. Moreover, in the DMEM and TSB, the stability of the GaACP increased gradually with the Ga content in the powders. It agrees with the literature data, reporting that incorporating vicarious metallic (e.g., magnesium, zinc, iron) ions stabilizes ACP and inhibits its crystallization[9,10,12].

Antibacterial properties of gallium-containing amorphous calcium phosphate powders

The growth curves of *P. aeruginosa* and *S. aureus* in the presence of 1, 2, and 4 mg/mL GaACP powder suspensions are shown in Fig. 6.

Regardless of the Ga content, the ACP powders at a 1 mg/mL concentration did not show a significantly different antibacterial effect compared to the control (bacterial suspension without powder). However, increasing the powder concentration to 2 mg/mL and 4 mg/mL inhibited bacterial growth. All samples had delayed exponential growth (log phase) compared to the control. However, complete prevention of bacterial growth was not observed. This indicates the bacteriostatic effect of the powders. In the case of *S. aureus*, no significant differences were observed among the powders with different Ga content. A more significant effect due to the Ga addition was observed in the case of *P. aeruginosa*. Namely, statistical analysis of the obtained results (Fig. S5, Supplementary Information) showed the higher inhibition of *P. aeruginosa* growth in the presence of GaACP compared to the Ga-free ACP powder. ACP powders with higher Ga content (6GaACP and 12GaACP) showed significantly higher inhibition of *P. aeruginosa* growth than the Ga-free ACP powder from the beginning of the test. In contrast, the powders with lower Ga content (2GaACP and 4GaACP) showed a significant difference in *P. aeruginosa* growth compared to ACP powder only after 400 min. Thus, the *P. aeruginosa* growth inhibition effect increased with increasing Ga content. The above is consistent with our previous study, where adding Ga to HAp provided more pronounced antibacterial properties against *P. aeruginosa* than other bacterial species[16]. Still, since the incorporation of Ga into ACP is limited, i.e., the achieved Ga content in the ACP is relatively low (up to 2.2 ± 0.1 wt%), the corresponding powder concentrations in the microbial culture medium (up to 4 mg/mL) may be insufficient to ensure significant inhibition of bacterial growth. Also, the stability of the tested powders in TSB plays a role. The stability tests showed that after 90 min, all samples, regardless of Ga content, crystallized in TSB medium (Table 2). The time before the exponential growth of bacteria starts for all samples, including the control, was up to 240 min (4 h). This means that when bacterial growth begins, the powders have transformed to the more stable partially crystalline CDHAp phase, affecting ions' release. Also, it is unclear whether Ga^{3+} ions are released into the medium during this transition or are incorporated into the CDHAp structure. To explain this, the ion release in TSB medium should be tested.

It cannot be ruled out that the inhibition of bacterial growth was due to the nanoscale nature of the powders. The nanosized ACP and GaACP particles can have an adverse effect on the bacteria by disrupting cell membranes and DNA synthesis, and interfering with metabolic processes[57,58].

Conclusions

Using the wet chemical precipitation method, amorphous calcium phosphate with variable and reproducible gallium content was obtained. Incorporating gallium into the amorphous calcium phosphate was limited,

reaching 2.2 ± 0.1 wt%. Despite the different chemical composition, the local symmetry of the phosphate groups in amorphous calcium phosphate remained unchanged. Regardless of gallium content, the specific surface area of all synthesized powders ranged from 151 to 167 m^2/g. In addition, scanning transmission electron microscopy images confirmed the nanosize of the synthesized powders, showing a spheroidal nanoparticle morphology.

The study provides new insight into the stability of the amorphous calcium phosphates. Generally, the synthesized gallium-containing amorphous calcium phosphate powders had low stability in various aqueous media, retaining the amorphous structure only up to 90 min. However, the effect of gallium content was observed, and it varied depending on the composition of the aqueous incubation medium. In deionized water, gallium slightly improved the stability of the amorphous calcium phosphate powders, inhibiting their crystallization. In addition, the gallium content significantly influenced the powders' stability in the biologically relevant incubation media, i.e., *Dulbecco's* modified *Eagle* medium and tryptone soya broth. Still, advanced analysis is required to understand the exact gallium-containing amorphous calcium phosphate crystallization mechanism in various aqueous media and interaction with multiple media components.

Although the gallium concentration in the media was too low to obtain total inhibition, the synthesized powders inhibited the growth of gram-negative (*Pseudomonas aeruginosa*) and gram-positive (*Staphylococcus aureus*) bacteria. Thus, the synthesized powders possess potential as starting materials to fabricate novel antibacterial biomaterials for bone regeneration applications.

Data availability

All data generated or analysed during this study are included in this published article (and its Supplementary Information files).

Received: 3 June 2025; Accepted: 21 July 2025
Published online: 24 July 2025

References

1. Beloti, M. M. & Rosa, A. L. Bone regeneration and repair materials. *J. Funct. Biomater.* **15** (3), 78. https://doi.org/10.3390/jfb15030078 (2024).
2. Li, Q., Ma, L. & Gao, C. Biomaterials for in situ tissue regeneration: development and perspectives. *J. Mater. Chem. B*. **3**, 8921–8938. https://doi.org/10.1039/C5TB01863C (2015).
3. Hou, X. et al. Calcium phosphate-based biomaterials for bone repair. *J. Funct. Biomater.* **13** (4), 187. https://doi.org/10.3390/jfb13040187 (2022).
4. Oryan, A., Alidadi, S., Moshiri, A. & Maffulli, N. Bone regenerative medicine: classic options, novel strategies, and future directions. *J. Orthop. Surg. Res.* **9** (18). https://doi.org/10.1186/1749-799X-9-18 (2014).
5. Shen, Q. et al. Advances in copper-based biomaterials with antibacterial and osteogenic properties for bone tissue engineering. *Front. Bioeng. Biotechnol.* **9**, 795425. https://doi.org/10.3389/fbioe.2021.795425 (2022).
6. Sprio, S., Tampieri, A., Dapporto, M., Iafisco, M. & Montesi, M. *Bioceramics in Regenerative Medicine*. In Pomeroy, M. (ed.) *Encyclopedia of Materials: Technical Ceramics and Glasses*, 601–6013 (Elsevier, 2021).
7. Baldwin, P. et al. Autograft, allograft, and bone graft substitutes: clinical evidence and indications for use in the setting of orthopaedic trauma surgery. *J. Orthop. Trauma*. **33**, 203–213 (2019).
8. Jeong, J., Kim, J. H., Shim, J. H., Hwang, N. S. & Heo, C. Y. Bioactive calcium phosphate materials and applications in bone regeneration. *Biomater. Res.* **23**, 4. https://doi.org/10.1186/s40824-018-0149-3 (2019).
9. Combes, C. & Rey, C. Amorphous calcium phosphates: synthesis, properties and uses in biomaterials. *Acta Biomater.* **6** (9), 3362–3378. https://doi.org/10.1016/j.actbio.2010.02.017 (2010). https://doi.org/https://doi.org/
10. Dorozhkin, S. V. Synthetic amorphous calcium phosphates (ACPs): preparation, structure, properties, and biomedical applications. *Biomater. Sci.* **9**, 7748–7798. https://doi.org/10.1039/D1BM01239H (2021).
11. Eliaz, N. & Metoki, N. Calcium phosphate bioceramics: a review of their history, structure, properties, coating technologies and biomedical applications. *Materials* **10**, 334 (2017).
12. Edén, M. Structure and formation of amorphous calcium phosphate and its role as surface layer of nanocrystalline apatite: implications for bone mineralization. *Materialia* **17**, 101107. https://doi.org/10.1016/j.mtla.2021.101107 (2021).
13. Adzila, S., Murad, M. & Sopyan, I. Doping metal into calcium phosphate phase for better performance of bone implant materials. *Recent. Pat. Mater. Sci.* **5** (1), 18–47 (2012).
14. Minandri, F., Bonchi, C., Frangipani, E., Imperi, F. & Visca, P. Promises and failures of gallium as an antibacterial agent. *Future Microbiol.* **9** (3), 379–397. https://doi.org/10.2217/fmb.14.3 (2014).
15. Mosina, M., Kovrlija, I., Stipniece, L. & Locs, J. Gallium containing calcium phosphates: potential antibacterial agents or fictitious truth. *Acta Biomater.* **150**, 48–57. https://doi.org/10.1016/j.actbio.2022.07.063 (2022).
16. Mosina, M. et al. Gallium-Doped hydroxyapatite shows antibacterial activity against Pseudomonas aeruginosa without affecting cell metabolic activity. *J. Funct. Biomater.* **14** (2), 51. https://doi.org/10.3390/jfb14020051 (2023).
17. Mouriño, V., Cattalini, J. P. & Boccaccini, A. R. Metallic ions as therapeutic agents in tissue engineering scaffolds: an overview of their biological applications and strategies for new developments *J. R. Soc. Interface*. 9, 401–419; (2012). https://doi.org/10.1098/rsif.2011.0611
18. Yang, M., Ren, J. & Zhang, R. Novel gallium-doped amorphous calcium phosphate nanoparticles: preparation, application and structure study. *J. Non-Cryst Solids*. **446–467**, 15–20 (2017).
19. Doebelin, N. & Kleeberg, R. Profex: a graphical user interface for the Rietveld refinement program BGMN. *J. Appl. Crystallogr.* **48**, 1573–1580. https://doi.org/10.1107/S1600576715014685 (2015).
20. Mosina, M. & Locs, J. Synthesis of amorphous calcium phosphate: a review. *Key Eng. Mater.* **850**, 199–206 (2020).
21. Rubenis, K., Zemjane, S., Vecstaudza, J., Bitenieks, J. & Locs, J. Densification of amorphous calcium phosphate using principles of the cold sintering process. *J. Eur. Ceram. Soc.* **41** (1), 912–919 (2021).
22. Rubenis, K. et al. Sintering of amorphous calcium phosphate to near-full density by uniaxial compaction at room temperature. *J. Eur. Ceram. Soc.* **42** (13), 6199–6205 (2022).
23. Vecstaudza, J., Gasik, M. & Locs, J. Amorphous calcium phosphate materials: formation, structure and thermal behaviour. *J. Eur. Ceram. Soc.* **39** (4), 1642–1649 (2019).
24. Roohani, I., Cheong, S. & Wang, A. How to build a bone? - Hydroxyapatite or posner's clusters as bone minerals. *Open. Ceram.* **6**, 100092. https://doi.org/10.1016/j.oceram.2021.100092 (2021).
25. Vecstaudza, J. & Locs, J. Novel Preparation route of stable amorphous calcium phosphate nanoparticles with high specific surface area. *J. Alloys Compd.* **700**, 215–222 (2017).

26. Indurkar, A. et al. Small organic molecules containing amorphous calcium phosphate: synthesis, characterization and transformation. *Front. Bioeng. Biotechnol.* **11**, 1–14. https://doi.org/10.3389/fbioe.2023.1329752 (2023).
27. Lotsari, A., Rajasekharan, A. K., Halvarsson, M. & Andersson, M. Transformation of amorphous calcium phosphate to bone-like apatite. *Nat. Commun.* **9**, 4170. https://doi.org/10.1038/s41467-018-06570-x (2018).
28. Eanes, E. D., Termine, J. D. & Nylen, M. U. An electron microscopic study of the formation of amorphous calcium phosphate and its transformation to crystalline apatite. *Calcif Tissue Res.* **12**, 143–158. https://doi.org/10.1007/BF02013730 (1973).
29. Čadež, V. et al. Amorphous calcium phosphate formation and aggregation process revealed by light scattering techniques. *Cryst. (Basel).* **8** (6), 254. https://doi.org/10.3390/cryst8060254 (2018).
30. Jin, B. et al. Phase transformation mechanism of amorphous calcium phosphate to hydroxyapatite investigated by Liquid-Cell transmission Electron microscopy. *Cryst. Growth Des.* **21** (9), 5126–5134. https://doi.org/10.1021/acs.cgd.1c00503 (2021).
31. Brangule, A. & Gross, K. A. Effect on drying conditions on amorphous calcium phosphate. *Key Eng. Mater.* **631**, 99–103 (2015).
32. Leroch, S. & Wendland, M. Influence of capillary Bridge formation onto the silica nanoparticle interaction studied by grand canonical Monte Carlo simulations. *Langmuir* **29** (40), 12410–12420. https://doi.org/10.1021/la402002f (2013).
33. Shrestha, S., Wang, B. & Dutta, P. Nanoparticle processing: Understanding and controlling aggregation. *Adv. Colloid Interface Sci.* **279**, 102162. https://doi.org/10.1016/j.cis.2020.102162 (2020).
34. Kim, S., Ryu, H. S., Shin, H., Jung, H. S. & Hong, K. In situ observation of hydroxyapatite nanocrystal formation from amorphous calcium phosphate in calcium-rich solutions. *Mater. Chem. Phys.* **91**, 500–506. https://doi.org/10.1016/j.matchemphys.2004.12.016 (2005).
35. Stammeier, J. A., Purgstaller, B., Hippler, D., Mavromatis, V. & Dietzel, M. In-situ Raman spectroscopy of amorphous calcium phosphate to crystalline hydroxyapatite transformation. *MethodsX* **5**, 1241–1250. https://doi.org/10.1016/j.mex.2018.09.015 (2018).
36. Dridi, A., Riahi, K. Z. & Somrani, S. Mechanism of apatite formation on a poorly crystallized calcium phosphate in a simulated body fluid (SBF) at 37°C. *J. Phys. Chem. Solids.* **156**, 110122. https://doi.org/10.1016/j.jpcs.2021.110122 (2021).
37. Sun, R. et al. Highly porous amorphous calcium phosphate for drug delivery and bio-medical applications. *Nanomaterials* **10** (1), 20. https://doi.org/10.3390/nano10010020 (2020).
38. Uskokovic, V., Tang, S. & Wu, V. M. On grounds of the memory effect in amorphous and crystalline apatite: kinetics of crystallization and biological response. *ACS Appl. Mater. Interfaces.* **10** (17), 14491–14508. https://doi.org/10.1021/acsami.8b02520 (2018).
39. Jin, W., Jiang, S., Pan, H. & Tang, R. Amorphous phase mediated crystallization: fundamentals of biomineralization. *Cryst. (Basel).* **8** (1), 48. https://doi.org/10.3390/cryst8010048 (2018).
40. Gelli, R., Ridi, F. & Baglioni, P. The importance of being amorphous: calcium and magnesium phosphates in the human body. *Adv. Colloid Interface Sci.* **269**, 219–235 (2019).
41. Gao, Y. et al. Preparation, characterization and cytocompatibility of porous ACP/PLLA composites. *J. Biomed. Mater. Res. A.* **79** (1), 193–200. https://doi.org/10.1002/jbm.a.30761 (2006).
42. Yu, Y., Bacsik, Z. & Edén, M. Contrasting in vitro apatite growth from bioactive glass surfaces with that of spontaneous precipitation. *Materials* **11** (9), 1690. https://doi.org/10.3390/ma11091690 (2018).
43. Chatzipanagis, K. et al. Crystallization of citrate-stabilized amorphous calcium phosphate to nanocrystalline apatite: A surface-mediated transformation. *CrystEngComm* **18**, 3170–3173. https://doi.org/10.1039/C6CE00521G (2016).
44. Mekmene, O. et al. Effects of pH and ca/p molar ratio on the quantity and crystalline structure of calcium phosphates obtained from aqueous solutions. *Dairy. Sci. Technol.* **89**, 301–216. https://doi.org/10.1051/dst/2009019 (2009).
45. Jiang, S., Cao, Y., Li, S., Pang, Y. & Sun, Z. Dual function of Poly (acrylic acid) on controlling amorphous mediated hydroxyapatite crystallization. *J. Cryst. Growth.* **557**, 125991. https://doi.org/10.1016/j.jcrysgro.2020.125991 (2021).
46. Bleotu, C., Iconaru, S. L., Ciobanu, C. S., Groza, A. & Predoi, D. Exploring the effects of dulbecco's modified eagle's medium on irradiated layers of magnesium-doped hydroxyapatite in a Chitosan matrix for biomedical applications. *Coatings* **15** (2), 209. https://doi.org/10.3390/coatings15020209 (2025).
47. Zong, C., Wang, Y. & Jiang, S. Toward the Understanding of Poly (Acrylic Acid) on amorphous calcium phosphate mediated collagen intrafibrillar mineralization: surface adsorption versus bulk incorporation. *J. Cryst. Growth.* **616**, 1–7 (2023).
48. Rohanová, D. et al. Is non-buffered DMEM solution a suitable medium for in vitro bioactivity tests? *J. Mater. Chem. B.* **2**, 5068–5076 (2014).
49. Saito, H., Araki, Y., Katsuno, H. & Nakada, T. Phase transition of amorphous calcium phosphate to calcium hydrogen phosphate dihydrate in simulated body fluid. *J. Cryst. Growth.* **553**, 125937 (2021).
50. Dontchos, B. N. et al. Optimizing CO_2 normalizes pH and enhances chondrocyte viability during cold storage. *J. Orthop. Res.* **26**, 643–650. https://doi.org/10.1002/jor.20534 (2008).
51. Eanes, E. D. Springer,. Amorphous calcium phosphate: thermodynamic and kinetic considerations, in: *Calcium phosphates in biological and industrial systems* (ed. Amjad, Z.) 21–39 (1998).
52. Romero, M. J. R. H. et al. Inhibition of hydroxyapatite growth by casein, a potential salivary phosphoprotein homologue. *Eur. J. Oral Sci.* **123** (4), 288–296. https://doi.org/10.1111/eos.12196 (2015).
53. Cross, K. J., Huq, N. L., Palamara, J. E., Perich, J. W. & Reynolds, E. C. Physicochemical characterisation of casein phosphopeptide-amorphous calcium phosphate nanocomplexes. *J. Biol. Chem.* **280** (15), 15362–15369. https://doi.org/10.1074/jbc.M413504200 (2005).
54. Liu, G. et al. Promoting the calcium-uptake bioactivity of casein phosphopeptides *in vitro* and *in vivo*. *Front. Nutr.* **8**, 1–9. https://doi.org/10.3389/fnut.2021.743791 (2021).
55. Lin, Z. et al. A further insight into the adsorption mechanism of protein on hydroxyapatite by FTIR-ATR spectrometry. *Spectrochim Acta Mol. Biomol. Spectrosc.* **173**, 527–531. https://doi.org/10.1016/j.saa.2016.09.050 (2017).
56. Xie, J., Riley, C., Kumar, M. & Chittur, K. FTIR/ATR study of protein adsorption and brushite transformation to hydroxyapatite. *Biomaterials* **23** (17), 3609–3616. https://doi.org/10.1016/S0142-9612(02)00090-X (2002).
57. Uskoković, V., Tang, S., Nikolić, M. G., Marković, S. & Wu, V. M. Calcium phosphate nanoparticles as intrinsic inorganic antimicrobials: in search of the key particle property. *Biointerphases* **14**, 031001. https://doi.org/10.1116/1.5090396 (2019).
58. Grynyuk, I. I. et al. Influence of nanoscale-modified apatite-type calcium phosphates on the biofilm formation by pathogenic microorganisms. *Open. Chem.* **19**, 39–48. https://doi.org/10.1515/chem-2021-0199 (2021).

Acknowledgements

The authors acknowledge access to infrastructure and competence from the European Union's Horizon 2020 research and innovation programme under the grant agreement No. 857287 (BBCE – Baltic Biomaterials Centre of Excellence).

Author contributions

Conceptualization - R.V., M.S., L.S.; Data curation - R.V., M.S., L.S., J.L.; Formal analysis - R.V.; Funding acquisition - R.V., J.L., L.S.; Investigation - R.V., M.S., L.S.; Methodology - R.V., M.S.; Project administration - J.L.; Resources - J.L.; Supervision - M.S., L.S., J.L.; Validation - R.V.; Visualization - R.V.; Writing original draft - R.V.,

L.S.; and Review & editing - M.S., L.S., J.L.

Funding
This research was funded by Riga Technical University 2024/2025 Project for Strengthening Scientific Personnel Capacity No. ZM-2025/9.

Declarations

Competing interests
The authors declare no competing interests.

Additional information
Supplementary Information The online version contains supplementary material available at https://doi.org/10.1038/s41598-025-12906-7.

Correspondence and requests for materials should be addressed to M.S. or L.S.

Reprints and permissions information is available at www.nature.com/reprints.

Publisher's note Springer Nature remains neutral with regard to jurisdictional claims in published maps and institutional affiliations.

Appendix III

Gallium-doped hydroxyapatite shows antibacterial activity against Pseudomonas aeruginosa without affecting cell metabolic activity

Marika Mosina, Claudia Siverino, Liga Stipniece, Artemijs Sceglovs, Renats Vasiljevs, Fintan T. Moriarty, Janis Locs.

Journal of Functional Biomaterials, **2023**, 14, 51. doi:10.3390/jfb14020051

M.S. input: conceptualization, investigation, data curation, formal analysis, visualization, writing the original draft, reviewing and editing.

Journal of *Functional Biomaterials*

MDPI

Article

Gallium-Doped Hydroxyapatite Shows Antibacterial Activity against *Pseudomonas aeruginosa* without Affecting Cell Metabolic Activity

Marika Mosina [1,2], Claudia Siverino [3], Liga Stipniece [1,2], Artemijs Sceglovs [1,2], Renats Vasiljevs [1,2], T. Fintan Moriarty [3] and Janis Locs [1,2,*]

[1] Rudolfs Cimdins Riga Biomaterials Innovation and Development Centre, Institute of General Chemical Engineering, Faculty of Materials Science and Applied Chemistry, Riga Technical University, Pulka 3, LV-1007 Riga, Latvia
[2] Baltic Biomaterials Centre of Excellence, Headquarters at Riga Technical University, LV-1048 Riga, Latvia
[3] AO Research Institute Davos, 7270 Davos, Switzerland
* Correspondence: janis.locs@rtu.lv; Tel.: +37-126-437-878

Abstract: Calcium phosphates (CaPs) have been used in bone regeneration for decades. Among the described CaPs, synthetic hydroxyapatite (HAp) has a chemical composition similar to that of natural bone. Gallium-containing compounds have been studied since the 1970s for the treatment of autoimmune diseases and have shown beneficial properties, such as antibacterial activity and inhibition of osteoclast activity. In this study, we synthesized hydroxyapatite (HAp) powder with Ga doping ratios up to 6.9 ± 0.5 wt% using the wet chemical precipitation method. The obtained products were characterized using XRD, BET, FTIR, and ICP-MS. Ga^{3+} ion release was determined in the cell culture media for up to 30 days. Antibacterial activity was assessed against five bacterial species: *Pseudomonas aeruginosa*, *Escherichia coli*, *Staphylococcus aureus*, *Staphylococcus epidermidis*, and *Streptococcus pyogenes*. The biocompatibility of the GaHAp samples was determined in human fibroblasts (hTERT-BJ1) through direct and indirect tests. The structure of the synthesized products was characteristic of HAp, as revealed with XRD and FTIR, although the addition of Ga caused a decrease in the crystallite size. Ga^{3+} was released from GaHAp paste in a steady manner, with approximately 40% being released within 21 days. GaHAp with the highest gallium contents, 5.5 ± 0.1 wt% and 6.9 ± 0.5 wt%, inhibited the growth of all five bacterial species, with the greatest activity being against *Pseudomonas aeruginosa*. Biocompatibility assays showed maintained cell viability (~80%) after seven days of indirect exposure to GaHAp. However, when GaHAp with Ga content above 3.3 ± 0.4 wt% was directly applied on the cells, a decrease in metabolic activity was observed on the seventh day. Overall, these results show that GaHAp with Ga content below 3.3 ± 0.4 wt% has attractive antimicrobial properties, without affecting the cell metabolic activity, creating a material that could be used for bone regeneration and prevention of infection.

Keywords: calcium phosphate; antibacterial properties; gallium; biocompatibility

Citation: Mosina, M.; Siverino, C.; Stipniece, L.; Sceglovs, A.; Vasiljevs, R.; Moriarty, T.F.; Locs, J. Gallium-Doped Hydroxyapatite Shows Antibacterial Activity against *Pseudomonas aeruginosa* without Affecting Cell Metabolic Activity. *J. Funct. Biomater.* **2023**, *14*, 51. https://doi.org/10.3390/jfb14020051

Academic Editor: Cecilia Persson

Received: 15 December 2022
Revised: 4 January 2023
Accepted: 11 January 2023
Published: 17 January 2023

1. Introduction

Calcium phosphates (CaPs) are widely used in bone regeneration due to their unique properties, such as biocompatibility, osteoinductivity, and osteoconductivity [1–3]. They are often applied as bone cements [4], scaffolds [5], and coatings [1,2]. The biological activity of any CaP depends on the physicochemical properties, such as Ca/P molar ratio and solubility. Even though there is a great number of CaPs, hydroxyapatite (HAp) is the most extensively used one due to its similarity to the mineral component of bone. HAp is the most thermodynamically stable phase of CaP, with a characteristic Ca/P molar ratio of 1.67 and relatively low solubility. Numerous studies focusing on HAp have been undertaken in

the last decades with both in vitro and in vivo assays, and conclusions have underlined its osteoconductive and osteoinductive properties [6–13].

In orthopedics, bacterial infection is a major problem leading to revision surgeries, implant removal, and possibly even amputation. Bacterial contamination of the wound may arise from the patient's skin or from the surrounding environment [14–17]. Antibiotics have proven to be the gold standard in preventing and treating infections. However, the systemic administration of antibiotics can have a negative effect on the body (e.g., renal toxicity or microbiome dysbiosis), and it can lead to the potentially low active local concentration of antibiotic at the infection site. Additionally, antibiotic resistance of clinically relevant pathogens is increasing every year, which only emphasizes the need for the development of new biomaterials with improved antibacterial properties [18].

The doping of CaPs, including HAp, with different metal ions has often been performed to enhance the material properties, in terms of bioactivity and/or antibacterial properties [19]. HAp has the ability to incorporate isomorphic substituents, such as magnesium (Mg), sodium (Na), strontium (Sr), silver (Ag), copper (Cu), etc., due to its flexible and stable crystalline structure [20]. The addition of antibacterial ions such as Ag [21,22], Cu [23,24], Zn [25], and Ga [26] provides antibacterial assets to CaPs. Tailoring a biomaterial with the aforementioned capacities could help to prevent bacterial growth at the surgical site after implantation.

Gallium has been known since the 1970s, and next to its antibacterial potential, it has been used to treat bone diseases. Gallium nitrate ($Ga(NO_3)_3$) is used as a drug to treat hypercalcemia [27–29]. The antibacterial activity of gallium compounds, such as gallium maltolate, nitrate, and citrate has been reported against different bacterial species, such as *Mycobacteriaceae (M.) tuberculosis*, *Mycobacterium (M.) avium*, *Staphylococcus (S.) aureus*, *Escherichia (E.) coli* [30], and *Pseudomonas (P.) aeruginosa* [31,32]. To date, the antibacterial activity of gallium-doped hydroxyapatite (GaHAp) has primarily been assessed against *P. aeruginosa* [29,33]. The antibacterial activity of gallium against both Gram-positive and Gram-negative bacterial species is supported by the similarity between Ga^{3+} and Fe^{3+} ions [34]. Namely, Ga^{3+} replaces Fe^{3+} in bacteria, resulting in the disruption of protein metabolism and leading to bacterial death [16,32].

In this study the antibacterial activity of GaHAp synthesized using the wet precipitation method was tested for the first time against a wide range of bacterial species: *P. aeruginosa*, *E. coli*, *S. aureus*, *S. epidermidis*, and *S. pyogenes*. Additionally, the biocompatibility of the produced GaHAp was assessed on human fibroblasts (hTERT-BJ1).

2. Materials and Methods

2.1. Synthesis of the Gallium-Doped Hydroxyapatite (GaHAp)

Gallium-doped hydroxyapatite (GaHAp) was synthesized via wet chemical precipitation using calcium oxide (CaO; >98%; Jost chemical, St. Louis, MI, USA), orthophosphoric acid (H_3PO_4; 75%; "Latvijas ķīmija" Ltd., Riga, Latvia), and gallium nitrate hydrate ($Ga(NO_3)_3 \cdot xH_2O$; 99.9% trace metal; Sigma-Aldrich, Burlington, MA, USA). In order to calculate the mass of gallium nitrate hydrate, the amount of water molecules of $Ga(NO_3)_3 \cdot 4.2H_2O$ was determined with inductively coupled plasma mass spectrometry (ICP-MS; Agilent 7700X; Santa Clara, CA, USA). The gallium concentrations used in the synthesis were 2, 4, 6.3, and 8 wt% with respect to the theoretical HAp yield. The initial (Ca + Ga)/P molar ratio of the reagents was 1.67. The molar ratio was kept constant for all the concentrations. Three replicates of the synthesis were performed for each Ga concentration.

The synthesis processes were performed in the synthesis workstation EasyMax 102 Advanced (Mettler Toledo, Columbus, OH, USA). CaO powder was added to deionized water, under vigorous stirring (420 rpm) at room temperature (22 °C), in order to obtain $Ca(OH)_2$ suspension. Then, $Ga(NO_3)_3 \cdot 4.2H_2O$ powder was added and stirred for five minutes. The synthesis mixture was heated to 45 °C, and the temperature was maintained constant during synthesis. Then, 2M H_3PO_4 was added to the starting suspension of

$Ca(OH)_2$ and $Ga(NO_3)_3 \cdot 4.2H_2O$ at an addition rate of 0.6 mL/min. The addition rate was reduced to 0.1 mL/min while approaching the synthesis end pH, 6.90 ± 0.05. The obtained precipitates were aged in the mother liquors at ambient temperature overnight (approximately 20 h). After ageing, the precipitates were vacuum-filtered and washed with 1 L of deionized water. HAp synthesized without $Ga(NO_3)_3 \cdot 4.2H_2O$ (also known as pure HAp) was used as a reference.

The synthesized products were used in two forms depending on the performed test: as paste (filtered wet precipitates) or as dried powder. GaHAp paste was steam-sterilized in a table-top autoclave at 121 °C for 20 min. To obtain powder, the paste (sterilized or non-sterilized) was dried in an oven at 105 °C for 24 h. Dried agglomerates were crushed with a mortar and pestle to obtain fine powder. GaHAp paste was used in the indirect cytotoxicity tests, while GaHAp powder was used in physicochemical characterization, antibacterial assays, and direct cytotoxicity tests.

2.2. Characterization Methods

2.2.1. X-ray Diffraction

The phase composition of the powders was analyzed using X-ray diffractometry (XRD; PANalytical X'Pert PRO; Westborough, MA, USA). XRD patterns were recorded using Ni filter and Cu Kα radiation at 40 kV and 30 mA, with a 2θ range of 10–70°.

The crystallite size was calculated from the X-ray diffraction profiles, according to the Debye–Scherrer equation (Equation (1)). The strong reflection of [002] was used by measuring the full width at half maximum (FWHM).

$$D = \frac{k\lambda}{\beta cos\theta} \quad (1)$$

where K is the Scherrer constant with a value of 0.9 [30], λ is the wavelength of light used for diffraction, β is the "full width at half maximum (FWHM)" of the [002] peak, and θ is the measured angle.

2.2.2. Fourier Transform Infrared Spectrometry

The chemical composition of the powders was analyzed using Fourier Transform Infrared Spectroscopy (FTIR; Bruker Tensor 27 spectrometer; Bruker Corporation, Billerica, MA, USA). FTIR spectra were recorded in Attenuated Total Reflectance (ATR) mode. Spectra were obtained at a resolution of 4 cm^{-1}, over a range of wavenumbers from 400 cm^{-1} to 4000 cm^{-1}, with an average of 50 scans. Before every measurement, a background spectrum was taken and deducted from the sample spectrum.

2.2.3. Specific Surface Area and Particle Size

The specific surface area (SSA) of the powders was determined using the Brunauer–Emmett–Teller (BET) method (ISO 9277:2010; QUADRASORB SI and Quadra Win, Quantachrome Instruments, Boynton Beach, FL, USA). Before BET analysis, samples were degassed for 24 h at 25 °C (Autosorb Degasser Model AD-9; USA) to remove all moisture and vapor. The SSA of the samples was analyzed using a nitrogen adsorption–desorption isotherm.

Particle size d_{BET} was calculated according to Equation (2) as stated in ISO standard No. 13779-3 "Implants for surgery Hydroxyapatite Part 3: Chemical analysis and characterization of crystallinity and phase purity", assuming particles to be spherical and nonporous.

$$d_{BET} = 6/(\rho \times SSA) \quad (2)$$

where ρ is the density of HAp and GaHAp, determined with a helium pycnometer (Micro UltraPyc 1200e; Quantachrome Instruments, Boynton Beach, FL, USA) as described in Section 2.2.4.

2.2.4. Helium Pycnometry

The true density of the powders was determined using a helium pycnometer. The instrument (cell volume) was calibrated with stainless-steel calibration spheres of known volume. After calibration, samples with known weight were filled into the sample cell and purged with helium gas in pulse mode (50 pulses). Detailed measurement parameters for helium pycnometry are described elsewhere [35].

2.2.5. Transmission Electron Microscope

The morphology of the powders was observed using a transmission electron microscope (TEM; FEI Tecnai G2 F20; Hillsboro, OR, USA) operated at 200 kV. Detailed sample preparation for TEM analysis is described elsewhere [36].

2.3. In Vitro Release of Gallium Ions

The investigation of Ga^{3+} ion release from GaHAp paste was performed in Dulbecco's Modified Eagle Medium (DMEM) with 1 g/L glucose (without $NaHCO_3$; Gibco, Thermo fiscer science, Waltham, MA, USA), with the addition of $NaHCO_3$ (99.7%; Sigma-Aldrich, Burlington, MA, USA) and NaN_3 (99.5% (as preservative); Sigma-Aldrich, Burlington, MA, USA). Afterwards, the medium was filter-sterilized through a 0.22 µm filter.

Prior to the ion release tests, GaHAp paste was steam-sterilized at 121 °C for 20 min. The sterile paste samples (50 mg of dry mass) were added to 50 mL of DMEM, vortexed and incubated at 37 °C in a table-top environmental shaker–incubator at 70 rpm (ES-20; Biosan, Riga, Latvia). During the first 72 h, the medium was collected by centrifuging the samples at 1610 g for 3 min and was then replaced with 50 mL of fresh DMEM every 24 h. Thereafter, the medium was refreshed every 72 h. The Ga concentration in the eluate was measured using ICP-MS (Agilent 7700X; Santa Clara, CA, USA). Three parallel measurements were performed for each GaHAp paste composition.

2.4. Antibacterial Tests

The antibacterial properties of GaHAp and $Ga(NO_3)_3{\cdot}4.2H_2O$ were determined against five bacterial species: Gram-negative *P. aeruginosa* (strain Paer09) and *E. coli* (strain American Type Culture Collection (ATCC) 25922); Gram-positive *S. aureus* (strain JAR 06013), *S. epidermidis* (strain ATCC 35984), and *S. pyogenes* (strain ATCC 19615). Different bacterial species were recovered from frozen stocks (−80 °C in 20% (*v/v*) glycerol) and cultured in tryptic soy broth (TSB; Oxoid, Basel, Switzerland) overnight in ambient air at 37 °C and agitation at 100 rpm. The overnight culture was then diluted with TSB to an optical density (OD) of 0.1 at 600 nm (10^6–10^7 colony-forming units (CFU)/mL).

The GaHAp powder used for the antibacterial experiments was prepared from sterilized paste that was dried for 24 h at 105 °C and ground using a pestle. Afterwards, the powder was packed and sterilized with hot air in a drying oven for 2 h at 134 °C.

2.4.1. Minimal Inhibitory Concentration (MIC) of $Ga(NO_3)_3{\cdot}4.2H_2O$

$Ga(NO_3)_3{\cdot}4.2H_2O$ was dissolved in milliQ water and diluted from 75 µg/mL to 450 µg/mL with TSB. A total volume of 150 µL of the solutions was mixed with 150 µL of TSB in a 96-well plate. A volume of 5 µL of bacterial culture with OD_{600} = 0.1 was added to each well and incubated for 24 h at 37 °C at 100 rpm. Bacterial growth (OD_{600}) was measured for 18 h at 37 °C in a plate reader (MultiskanGo; Thermo Scientific, Waltham, MA, USA) or it was quantified via serial dilution and total viable count on tryptic soy agar (TSA) plates.

2.4.2. Antibacterial Properties of GaHAp

GaHAp powders were suspended in TSB at concentrations of 1, 2, and 4 mg/mL. A total of 300 µL of the suspension was transferred to a 96-well plate, and 5 µL (OD_{600} = 0.1) of bacteria was added to each well. The absorbance of the plate at 600 nm was measured as described in Section 2.4.1.

2.5. Cytocompatibility Test

2.5.1. Cytotoxicity of $Ga(NO_3)_3 \cdot 4.2H_2O$

Cytotoxicity was tested on telomerase-immortalized human foreskin fibroblasts (hTERT-BJ1), which were purchased from Clontech (Clontech Laboratories, Mountain View, CA, USA). hTERT-BJ1 were routinely cultured as previously described [37]. Briefly, hTERT-BJ1 were cultivated in DMEM with 1 g/L glucose (without $NaHCO_3$; Gibco, Thermo fiscer science, Waltham, MA, USA), supplemented with $NaHCO_3$ (99.7%; Sigma-Aldrich, Burlington, MA, USA) and 10 % fetal bovine serum (Biochrome, Sigma-Aldrich, Burlington, MA, USA), with the addition of 100 µg/mL streptomycin (Gibco) and 100 U/mL penicillin (Gibco), at 37 °C in a humidified 5% CO_2 atmosphere. In total, 10^4 cells per well were seeded on a 96-well plate. The following day, $Ga(NO_3)_3 \cdot 4.2H_2O$ solutions at different concentrations (75–450 µg/mL) were applied to the cells and incubated for one and three days. To determine cell viability, CellTiter-Blue (Promega, Promega Corporation, Madison, WI, USA) was performed following the manufacturer's instructions. Cell viability (calculated in %) was determined as the fluorescence ratio between cells grown in the presence and absence of $Ga(NO_3)_3 \cdot 4.2H_2O$ solutions. The average values and standard deviations were calculated from three parallel samples in three independent experiments. Dimethyl sulfoxide (DMSO; Sigma-Aldrich, Burlington, MA, USA) was used as a negative control.

2.5.2. Cytotoxicity of GaHAp

hTERT-BJ1 cells were cultured as described above, and the cytotoxicity of GaHAp was assessed using direct and indirect methods. For the direct test, 10^4 cells per well were seeded on a 96-well plate, and the following day, GaHAp powder suspensions (prepared as described in Section 2.4.2, at concentrations of 1, 2, and 4 mg/mL in DMEM) were applied to the cells and incubated for one, three, and seven days.

In the indirect test, 1.5×10^4 cells per well were seeded on a six-well plate, and the following day, a cell strainer (Corning®, Amsterdam, The Netherlands), with a pore size of 100 µm containing GaHAp paste (250 ± 50 mg), was placed in each well and incubated for one, three, and seven days. In order to determine cell viability, CellTiter-Blue was performed in both tests following the manufacturer's instructions. Cell viability (%) was determined as the fluorescence ratio between cells grown in the presence and absence of GaHAp. The average values and standard deviations were calculated from three parallel samples. As a negative control, DMSO was used.

2.6. Statistical Analysis

The results are presented as mean values ± standard deviations (SDs) of three experiments. Statistical analysis was performed on microstructure parameters (specific surface area, density, and particle size) and on cytocompatibility test data using one-way ANOVA with Tukey's multiple comparison test, and $p < 0.05$ was used as a limit to indicate statistical significance (ns > 0.05; * $p < 0.05$; ** $p < 0.01$; *** $p < 0.005$; **** $p < 0.001$).

3. Results

3.1. Physicochemical Characteristics

The main characteristics of the synthesized powders are summarized in Table 1. The GaHAp powders had a higher specific surface area (SSA) than the HAp powders ($p < 0.05$), revealing that the addition of Ga led to the reduction in the particle size. After steam sterilization, the SSA decreased. Nevertheless, the SSA of the sterilized GaHAp powders was higher than that of the HAp powders ($p < 0.05$).

The phase composition of the synthesized powders was analyzed using XRD, and the corresponding XRD patterns are shown in Figure 1. Regardless of the chemical composition, all the XRD patterns have characteristic apatite peaks that correspond to the values reported in the literature [38,39]. The XRD patterns did not reveal the presence of additional phases or peak shifts across the different materials. The different amounts of Ga added to the synthesis (2, 4, 6.3, or 8 wt%) did, however, produce a broadening of the XRD peaks

(Figure 1A). After steam sterilization, the characteristic peaks become sharper, which indicates an increase in the crystallinity of the samples (Figure 1B).

Table 1. Ga contents, particle sizes (d_{BET}), densities, and SSAs of the synthesized products before and after sterilization.

Sample	Theoretical Ga Content (wt%)	Gallium Content (wt%)	Before Sterilization			After Sterilization		
			SSA (m^2/g)	ρ (g/cm^3)	d_{BET} (nm)	SSA (m^2/g)	ρ (g/cm^3)	d_{BET} (nm)
HAp	-	-	71 ± 7	2.77 ± 0.04	31 ± 3	50 ± 2	2.94 ± 0.01	41 ± 2
2 GaHAp	2	1.6 ± 0.1	95 ± 5	2.85 ± 0.06	22 ± 1	78 ± 3	2.86 ± 0.08	27 ± 1
4 GaHAp	4	3.3 ± 0.4	117 ± 4	2.80 ± 0.06	18 ± 1	88 ± 5	2.92 ± 0.09	23 ± 1
6.3 GaHAp	6.3	5.5 ± 0.1	109 ± 2	2.83 ± 0.01	20 ± 1	89 ± 4	2.92 ± 0.05	23 ± 1
8 GaHAp	8	6.9 ± 0.5	102 ± 5	2.79 ± 0.03	21 ± 1	104 ± 3	2.84 ± 0.04	20 ± 1

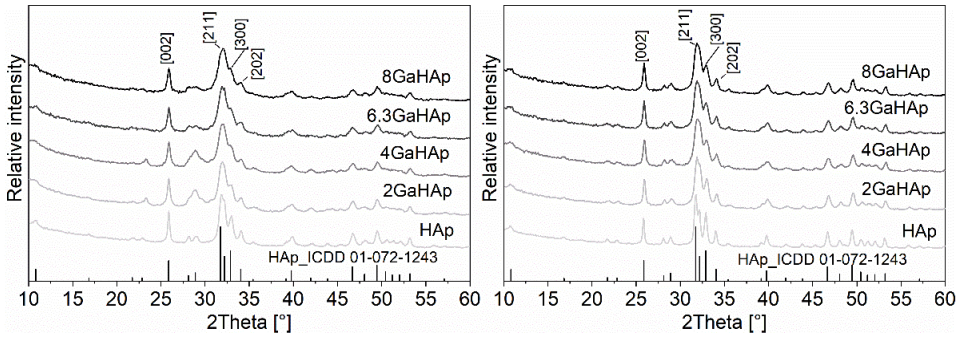

Figure 1. X-ray diffraction patterns of the synthesized powders with different amounts of gallium (**A**) before and (**B**) after steam sterilization at 121 °C for 20 min.

The crystallite sizes of the diffraction plane [002] for HAp and GaHAp powders were calculated using the Debye–Scherrer equation, and the obtained values are summarized in Table 2. According to these calculations, nano-sized crystallites were obtained, regardless of their chemical composition. With the addition of Ga, the crystallite size of GaHAp decreased compared with the HAp powders. However, before sterilization, differences in crystallite size were not observed among the GaHAp powders.

Table 2. Crystallite sizes of the synthesized products calculated using the Debye–Scherrer equation.

Sample	Plane (hkl)	Before Sterilization		After Sterilization	
		FWHM	Crystallite Size (nm)	FWHM	Crystallite Size (nm)
HAp	[002]	0.274	31.1	0.219	38.9
2 GaHAp	[002]	0.347	24.5	0.284	30.0
4 GaHAp	[002]	0.384	22.2	0.279	30.5
6.3 GaHAp	[002]	0.383	22.2	0.309	27.6
8 GaHAp	[002]	0.372	22.9	0.316	27.0

The FTIR spectra (Figure 2) of HAp and GaHAp show similar appearances. All spectra have HAp characteristic absorbance bands corresponding to ν_3 PO_4^{3-} group vibrations at 1030 and 1097 cm^{-1}. The absorbance band from the vibration of group ν_1 PO_4^{3-} is observed at 960 cm^{-1}. Moreover, the absorbance bands at 604 and 560 cm^{-1} can be attributed to

ν_4 PO_4^{3-} group vibrations. The band at 635 cm^{-1} corresponds to the vibration of the OH^- group. The band assignments are in accordance with literature data [40,41]. The characteristic absorbance bands become broader with the increase in Ga content in the synthesized powders.

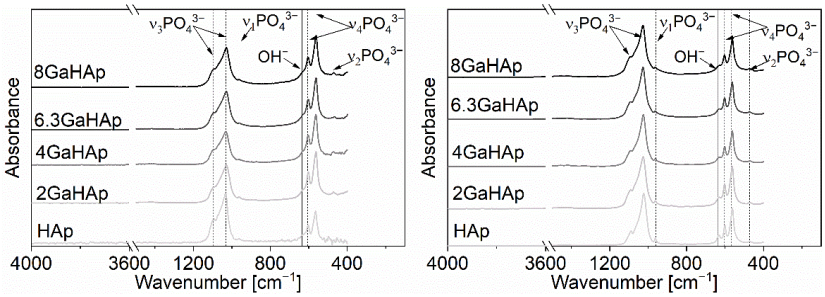

Figure 2. FTIR spectra of the synthesized powders with different amounts of gallium (**a**) before and (**b**) after steam sterilization at 121 °C for 20 min.

TEM micrographs were used to analyze the morphology of HAp and GaHAp particles (Figure 3). The TEM results showed a rod-like shape for GaHAp particles and a size less than 50 nm, which corresponds to the value calculated using BET data. The size of the nanoparticles decreased with the increase in Ga concentration.

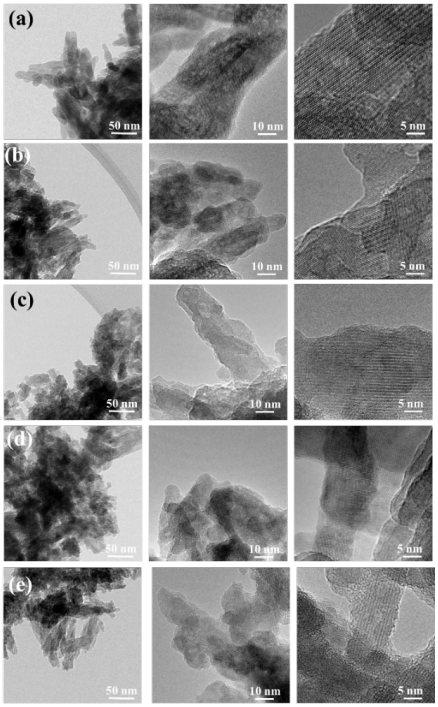

Figure 3. TEM images of synthesized GaHAp powders with different amounts of gallium: (**a**) HAp (**b**) 2 GaHAp; (**c**) 4 GaHAp; (**d**) 6.3 GaHAp; (**e**) 8 GaHAp.

3.2. In Vitro Ga^{3+} Release

The release profiles of Ga^{3+} from the GaHAp paste samples are shown in Figure 4. For 2 GaHAp and 4 GaHAp, ion release was measured until days 21 and 27, respectively, as the amount of Ga detected at subsequent time points was below the ICP-MS detection limit (<0.2 mg/kg). In the case of samples with higher Ga concentrations, i.e., 6.3 GaHAp and 8 GaHAp, a gradual release was observed up to 30 days. No high initial or burst release of Ga^{3+} was observed for any GaHAp. The cumulative Ga^{3+} release rate was higher from samples with lower Ga content, namely, 2 GaHAp (44.3 ± 0.9%) and 4 GaHAp (43.1 ± 3.6%), while 6.3 GaHAp and 8 GaHAp Ga release rates were 48.6 ± 1.1% and 49.8 ± 4.6%, respectively, within 30 days.

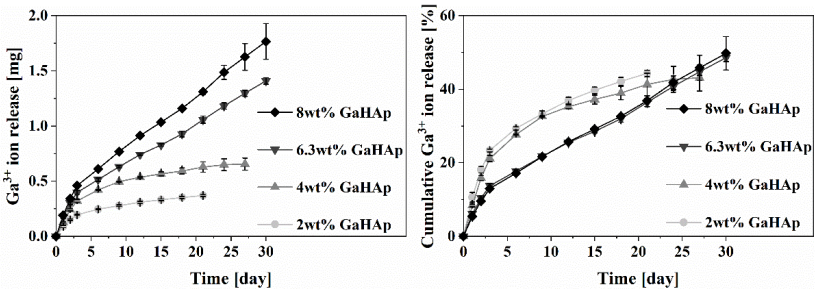

Figure 4. Ga^{3+} ion release from GaHAp paste with different amounts of gallium as a function of a time. Release overtime was performed in DMEM media at 37 °C (n = 3 ± SD).

3.3. Antibacterial Activity

3.3.1. Minimal Inhibitory Concentration of $Ga(NO_3)_3 \cdot 4.2H_2O$

P. aeruginosa and *S. aureus* growth in the presence of $Ga(NO_3)_3 \cdot 4.2H_2O$ solution was measured by means of absorbance (OD_{600}), and the results are shown in Figure 5. After 18 h of incubation, a total inhibition of *P. aeruginosa* growth was observed (Figure 5a). In contrast, *S. aureus* (Figure 5b) and *E. coli*, *S. epidermidis*, and *S. pyogenes* (Figure S1) showed growth reduction in the presence of $Ga(NO_3)_3 \cdot 4.2H_2O$, but not complete inhibition.

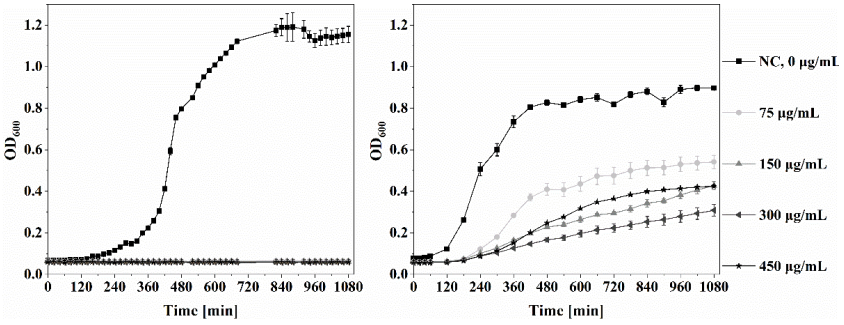

Figure 5. Bacterial growth of *P. aeruginosa* and *S. aureus* in the presence of $Ga(NO_3)_3 \cdot 4.2H_2O$. (**a**) *P. aeruginosa* and (**b**) *S. aureus* were grown in TSB with different concentrations of $Ga(NO_3)_3 \cdot 4.2H_2O$ (from 0 µg/mL to 450 µg/mL $Ga(NO_3)_3 \cdot 4.2H_2O$). The optical density (OD) at 600 nm was measured over 18 h using a plate reader.

The minimal inhibitory concentration (MIC) and CFU/mL of bacterial species are shown in supplementary data Figure S2. The MIC of $Ga(NO_3)_3 \cdot 4.2H_2O$ against *P. aerugi-*

nosa was 75 µg/mL; against *S. aureus*—150 µg/mL; against *E. coli*—200 µg/mL; against *S. epidermidis*—250 µg/mL; and against *S. pyogenes*—75 µg/mL.

3.3.2. Antibacterial Properties of GaHAp

The growth curves of *P. aeruginosa* and *S. aureus* in the presence of 1, 2, and 4 mg/mL GaHAp powder suspensions are shown in Figures 6 and 7. The growth curves of the other bacterial species (*S. epidermidis*, *S. pyogenes*, and *E. coli*) are shown in Figure S2.

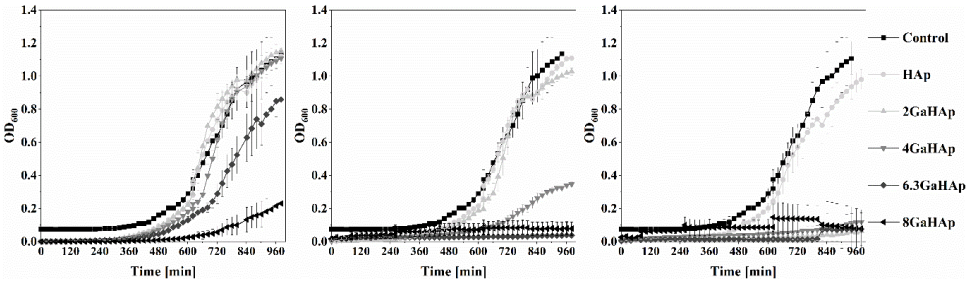

Figure 6. *P. aeruginosa* growth in the presence of GaHAp powder suspensions in TSB at (**a**) 1 mg/mL (**b**) 2 mg/mL, and (**c**) 4 mg/mL. The represented OD_{600} was obtained by subtracting the initial OD_{600_oh} (starting time = 0 h) from the measured $OD_{600\_x\ h}$ at specific time points.

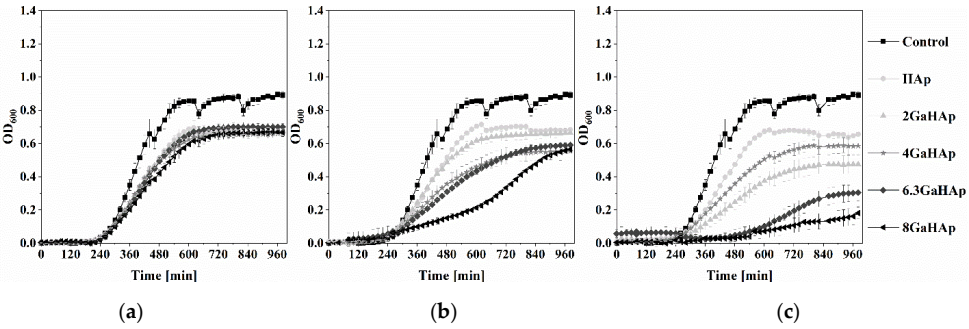

Figure 7. *S. aureus* growth inhibition induced by GaHAp powder suspensions in TSB at (**a**) 1 mg/mL (**b**) 2 mg/mL, and (**c**) 4 mg/mL concentrations. The represented OD_{600} was obtained by subtracting the initial OD_{600_oh} (starting time = 0 h) from the measured $OD_{600\_x\ h}$ at specific time points.

In the case of 1 mg/mL GaHAp, only the highest Ga-containing powder (8 GaHAp) showed inhibitory effects on *P. aeruginosa* growth (Figure 6a). With 2 mg/mL (Figure 6b) and 4 mg/mL (Figure 6c) GaHAp, a stronger inhibitory effect was observed, and when using 4 mg/mL (Figure 6c), total inhibition of *P. aeruginosa* growth with 4 GaHAp, 6.3 GaHAp, and 8 GaHAp was observed. Growth inhibition was detected with the same concentration of 4 GaHAp and 6 GaHAp against *S. aureus* (Figure 7c), *S. epidermidis* (Figure S3), *S. pyogenes* (Figure S4), and *E. coli* (Figure S5).

3.4. Cytocompatibility Test

3.4.1. Cytotoxicity of $Ga(NO_3)_3 \cdot 4.2H_2O$

The cell viability of hTERT-BJ1 in the presence of $Ga(NO_3)_3 \cdot 4.2H_2O$ solution is shown in Figure 8. A rapid decrease in cell viability was observed after the first day, starting from 150 µg/mL $Ga(NO_3)_3 \cdot 4.2H_2O$ ($p < 0.001$). Concentrations of $Ga(NO_3)_3 \cdot 4.2H_2O$ above

the MIC (75 µg/mL) exhibited an increased toxicity already on the first day. After three days, only the cells exposed to 75 µg/mL $Ga(NO_3)_3 \cdot 4.2H_2O$ showed maintained metabolic activity, around 80%.

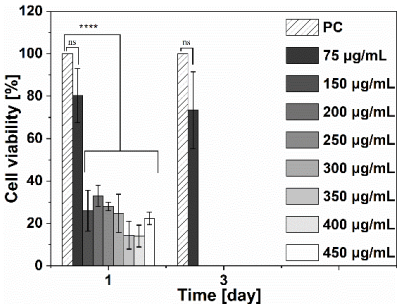

Figure 8. Metabolic activity of human fibroblasts (hTERT-BJ1) exposed to different concentrations of $Ga(NO_3)_3 \cdot 4.2H_2O$ solutions, where PC—positive control. Negative control results were omitted from the graphs as the values were approximately 0%. (One-way ANOVA single factor with Tukey's multiple comparison test, $n = 3$; ns > 0.05; **** $p < 0.001$).

3.4.2. Cytotoxicity of GaHAp

The influence of GaHAp on human fibroblast (hTERT-BJ1) viability was tested by applying GaHAp powder directly on the cells. After three days of exposure to different GaHAp concentrations (1, 2, and 4 mg/mL), cells were still metabolically active (above 80% viability) (Figure 9b). However, on day seven (Figure 9c), a rapid decrease in cell viability was observed with 2 mg/mL 8 GaHAp and with 4 mg/mL 4 GaHAp, 6.3 GaHAp, and 8 GaHAp paste samples (less than 40 %).

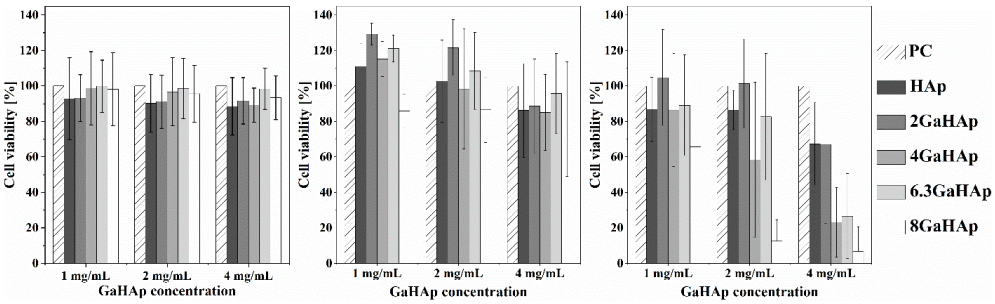

(**a**) (**b**) (**c**)

Figure 9. Metabolic activity of human fibroblasts (hTERT-BJ1) exposed to GaHAp powder suspensions at different concentrations (1, 2, and 4 mg/mL) obtained using the direct test: (**a**) day 1; (**b**) day 3, and (**c**) day 7. PC—positive control (ANOVA test, $n = 3$).

Human fibroblast (hTERT-BJ1) viability using the different GaHAp paste samples is shown in Figure 10. The indirect test results indicate that the released Ga^{3+} from GaHAp paste samples did not have cytotoxic effect at any time point, and even after seven days, cell viability was around 90%. Additionally, the metabolic activity of the cells exposed to 6.3 GaHAp and 8 GaHAp paste samples on day three was significantly increased.

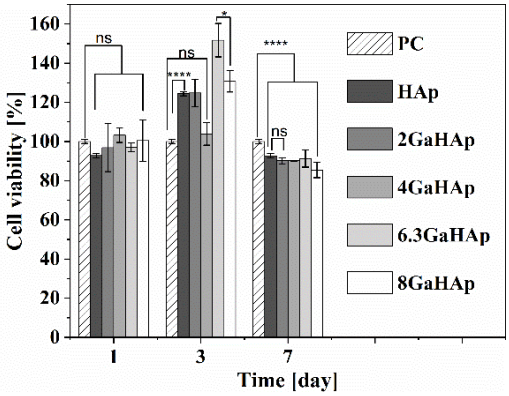

Figure 10. Metabolic activity of human fibroblasts (hTERT-BJ1) exposed to Ga^{3+} released from GaHAp paste obtained using the indirect test. (One-way ANOVA single factor with Tukey's multiple comparison test, $n = 3$; ns > 0.05; * $p < 0.005$; **** $p < 0.001$).

4. Discussion

In the present work, we successfully synthesized Ga-doped-HAp using the wet chemical precipitation method.

The morphological and structural nature of the obtained GaHAp coincides with that in previously described studies [29,33,42,43]. The synthesized products had low crystallinity, as suggested by the low-intensity, broad XRD peaks [38,39]. The adsorption of smaller ions, such as Ga^{3+} compared with Ca^{2+}, on the HAp crystal surface results in the inhibition of crystallization and crystal growth [29,42,44–46]. Additionally, steam sterilization had a significant effect on the morphology of the final product. Re-crystallization of the product was observed in the XRD patterns, due to the fact that a hydrothermal reaction occurs under high-temperature and -pressure conditions. This process leads to the nucleation of the crystals and their growth as described in [44,45]. Due to the low crystallinity of the samples obtained in our study, it is challenging to detect the Ga^{3+} substitution of Ca^{2+} in the structure. Possibly, Ga^{3+} is adsorbed/chemisorbed on the particle surface or taken up in the interstitial positions [47]. However, there is no universal technique to detect ion substitution in the interstitial position.

The potential of HAp materials to act as delivery systems of antibacterial Ga^{3+} ions was investigated by assessing ion release in the cell culture medium. The release of antibacterial ions from the implant material during the initial periods after surgery is important in preventing the development of infections [48]. As bone-associated infections oftenoccur within four months of surgical interventionsprolonged delivery of antibacterial ions may be necessary [28]. Thus, it is important to evaluate the release of Ga^{3+} ions over long periods. The Ga^{3+} release profile depends on the Ga content in products, the degree of Ca deficiency of products, the released media, and the conditions [49]. The increase in Ga content in the HAp samples is at the expense of reducing the Ca/P molar ratio. Thus, non-stoichiometric or Ca-deficient HAp (CDHAp) is obtained, which is more soluble than HAp [50]. If Ga does not enter the Ca site in HAp crystallites, it accumulates in the hydrated layer on the surface of crystallites. Additionally, during the first 72 h, the cumulatively released amount of Ga^{3+} increases more rapidly, i.e., the frequent refreshing of the medium results in a faster release of the ions. Ideally, the flow of the release medium should be aligned with the flow rate of physiological fluids at the site of implantation. The results of the ion release tests have shown that by increasing the Ga concentration above 3.3 ± 0.4 wt%, it is possible to obtain HAp for long-term delivery of Ga^{3+}. Furthermore, approximately 50% of ions were not released within the timeframe of our study, suggesting further long-term delivery up to four months.

The biological properties of $Ga(NO_3)_3 \cdot 4.2H_2O$, used as the gallium source, were compared to GaHAp paste or GaHAp powder. $Ga(NO_3)_3 \cdot 4.2H_2O$ and GaHAp showed similar antibacterial activity against different Gram-positive and Gram-negative bacterial species. This might be connected to the bacterial cell wall structure (Figure S7) [32,51]. Gram-positive bacteria have a thicker cell wall, which makes the bacterial cell impenetrable for Ga compared with Gram-negative bacteria. On the other hand, Gram-negative bacteria, with their thinner cell wall, have a membrane that can lead to Ga penetration. Additionally, Gram-negative bacteria have Fe-dependent metabolism, and Ga^{3+} can replace Fe^{3+} on active enzymatic sites and disrupt protein metabolism, leading to bacterial death [52]. Interestingly, the HAp nanoparticles without Ga also showed delayed bacterial growth. This could be explained by the fact that nanoparticles themselves can have a negative effect on bacterial growth [48,50]. However, GaHAp did not show total inhibition of *P. aeruginosa* growth, as observed in the case of $Ga(NO_3)_3 \cdot 4.2H_2O$. This effect is related to the delayed Ga^{3+} release from HAp, leading to lower Ga^{3+} concentration in media during the first 24 h. $Ga(NO_3)_3 \cdot 4.2H_2O$ completely inhibited *P. aeruginosa* growth, but this was not observed in the case of *E. coli*, even though both bacteria are Gram negative. The iron uptake pathway via siderophore enterobactin (ENT) in *P. aeruginosa* and *E. coli* is different [53]. In contrast with other studies, in our results, we obtained bacterial growth inhibition at higher concentrations of GaHAp powder. For example, Kurtjak et al. obtained inhibition of *P. aeruginosa* growth with 0.9 g/mL GaHAp containing 3 wt% of Ga (synthesized using the co-precipitation method) [29]. In addition, Ballardini et al. showed an antibacterial effect of Ga-doped HAp against *P. aeruginosa* and *S. aureus*. However, *E. coli* and *C. albicans* showed higher resistance to Ga-doped HAp after 24 h [54]. Even though the final product was Ga-doped-HAp, the synthesis methods used differed in the previous examples. These important findings indicate that the synthesis method influences key properties of the final material.

It is also important to test the biocompatibility of the produced material. In this study, we observed different effects of $Ga(NO_3)_3 \cdot 4.2H_2O$ and GaHAp paste or powder on cell metabolic activity. $Ga(NO_3)_3 \cdot 4.2H_2O$ has a strong acidic nature, which hydrolyzes in a wide pH range of aqueous media. This process leads to the formation of hydroxylate species, predominantly $[Ga(OH)_4]^-$ and hydronium ion (H_3O^+) [55–57], leading to the acidification of cell culture media. Indeed, we observed a change in medium color between 75 and 450 μg/mL $Ga(NO_3)_3 \cdot 4.2H_2O$, indicating a decrease in pH, which results in cell death. The results from the direct and indirect tests of GaHAp on human fibroblast show the importance of evaluating the interactions between the new developed biomaterial and cells. When the materials (GaHAp paste or powder) were not in direct contact with the cells, we observed a higher metabolic activity in fibroblasts after 7 days. Presumably, the ions released from GaHAp paste (Ga^{3+} but also Ca^{2+}) can stimulate cell growth. In the case of pure HAp, cell viability was approximately 120%. It has already been reported that Ca^{2+} ions promote bone formation and maturation [2]. From the literature, Pajor et al. observed the toxic effect of GaHAp prepared with the dry method on the BALB/c 3T3 clone A31 mammalian cell line compared with the same material prepared with the wet method. In the study, this coherence was explained with the solubility of the materials obtained with different synthesis methods [42]. That was another confirmation that the material form and the method used can have an influence on material–cell interactions.

5. Conclusions

Gallium-doped hydroxyapatite (GaHAp) was successfully obtained, and it showed promising biological properties. The optimal Ga^{3+} doping rate of HAp ranges from 2 to 5.5 ± 0.1 wt%, as it was shown from the analyses of the morphological properties and biological activity. The addition of Ga to the synthesis media promoted the formation of HAp with smaller particle sizes. GaHAp provided long-term gallium ion release with Ga concentrations above 3.3 ± 0.4 wt%. Additionally, GaHAp had a bacteriostatic effect on multiple bacterial species, both Gram positive and Gram negative, without substantial

toxicity towards human fibroblasts. The GaHAp samples showed superior inhibition of *P. aeruginosa* compared with the other bacterial species, representing a material advantage for the early-stage treatment of bone defect, as it prevents further bacterial growth and could prevent the development of chronic and acute infection.

Supplementary Materials: The following supporting information can be downloaded at: https://www.mdpi.com/article/10.3390/jfb14020051/s1, Figure S1: Growth curves in the presence of $Ga(NO_3)_3{\cdot}4.2H_2O$ at different concentrations of (A) *E. coli*, (B) *S. epidermidis*, and (C) *S. pyogenes*, Figure S2: *S. epidermidis* growth curves in the presence of GaHAp paste at different concentrations, Figure S3: *S. pyogenes* growth curves in the presence of GaHAp paste at different concentrations, Figure S4: *E. coli* growth curves in the presence of GaHAp paste at different concentrations, Figure S5: The minimal inhibitory concentration of $Ga(NO_3)_3{\cdot}4.2H_2O$ against 5 bacterial species, Figure S6: Human fibroblasts (hTERT-BJ1) were exposed to GaHAp for the indirect test on day 3. PC—positive control; scale bar—200 µm, Figure S7: The structural difference between Gram-negative and Gram-positive bacteria (created using Biorender.com. accessed on 7 December 2022).

Author Contributions: Conceptualization, M.M., L.S. and J.L.; methodology, M.M., C.S., R.V. and A.S.; validation, J.L., T.F.M., L.S. and C.S.; formal analysis, M.M., R.V. and A.S.; investigation, M.M., L.S., R.V., C.S. and A.S.; resources, J.L. and T.F.M.; data curation, L.S., C.S., A.S., J.L. and T.F.M.; writing—original draft preparation, M.M. and L.S.; writing—reviewing and editing, M.M., L.S., C.S., A.S., J.L. and T.F.M.; visualization, M.M.; supervision, L.S, J.L, C.S. and T.F.M.; project administration, J.L; funding acquisition, J.L. All authors have read and agreed to the published version of the manuscript.

Funding: This work was funded by the EuroNanoMedIII project "NANO delivery system for one-shot regenerative therapy of peri-implantis" (ImplantNano, GA.ES RTD/2020/19) and the European Union's Horizon 2020 research and innovation program under grant agreement No. 857287.

Institutional Review Board Statement: Not applicable.

Informed Consent Statement: Not applicable.

Data Availability Statement: The data presented in this study are available upon request from the corresponding author. The data are not publicly available due to project agreement.

Acknowledgments: The authors would like to thank Jana Vecstaudza and Kristaps Rubenis for their scientific discussion sessions.

Conflicts of Interest: The authors declare no conflict of interest.

References

1. Ben-Nissan, B. *Advances in Calcium Phosphate Biomaterials*; Springer: Berlin/Heidelberg, Germany, 2014. [CrossRef]
2. Jeong, J.; Kim, J.H.; Shim, J.H.; Hwang, N.S.; Heo, C.Y. Bioactive Calcium Phosphate Materials and Applications in Bone Regeneration. *Biomater. Res.* **2019**, *23*, 4. [CrossRef]
3. Samavedi, S.; Poindexter, L.K.; Van Dyke, M.; Goldstein, A.S. *Synthetic Biomaterials for Regenerative Medicine Applications*; Elsevier Inc.: Amsterdam, The Netherlands, 2014; pp. 81–99. [CrossRef]
4. Ambard, A.J.; Mueninghoff, L. Calcium Phosphate Cement: Review of Mechanical and Biological Properties. *J. Prosthodont.* **2006**, *15*, 321–328. [CrossRef] [PubMed]
5. Sun, H.; Yang, H.L. Calcium Phosphate Scaffolds Combined with Bone Morphogenetic Proteins or Mesenchymal Stem Cells in Bone Tissue Engineering. *Chin. Med. J.* **2015**, *128*, 1121–1127. [CrossRef]
6. Driskell, T.D.; Hassler, C.R.; Tennery, V.J.; McCoy, L. Calcium Phosphate Resorbable Ceramics: A Potential Alternative to Bone Grafting. *J. Dent. Res.* **1973**, *52*, 123–131.
7. Denissen, H.W.; de Groot, K. Immediate Dental Root Implants from Synthetic Dense Calcium Hydroxylapatite. *J. Prosthet. Dent.* **1979**, *42*, 551–556. [CrossRef] [PubMed]
8. Zaner, D.J.; Yukna, R.A. Particle Size of Periodontal Bone Grafting Materials. *J. Periodontol.* **1984**, *55*, 406–409. [CrossRef]
9. Klein, C.P.A.T.; de Groot, K.; Drissen, A.A.; van der Lubbe, H.B.M. Interaction of Biodegradable β-Whitlockite Ceramics with Bone Tissue: An in Vivo Study. *Biomaterials* **1985**, *6*, 189–192. [CrossRef]
10. Brown, W.E.; Chow, L.C.C. A New Calcium Phosphate, Water–Setting Cement. *Acc. Chem. Res.* **1986**, 351–379.
11. Yuan, H.; Barbieri, D.; Luo, X.; Van Blitterswijk, C.A.; De Bruijn, J.D. Calcium Phosphates and Bone Induction. *Compr. Biomater. II* **2017**, *1*, 333–349. [CrossRef]

12. Lin, L.; Chow, K.L.; Leng, Y. Study of Hydroxyapatite Osteoinductivity with an Osteogenic Differentiation of Mesenchymal Stem Cells. *J. Biomed. Mater. Res.-Part A* **2009**, *89*, 326–335. [CrossRef]
13. Wang, Z.; Han, T.; Zhu, H.; Tang, J.; Guo, Y.; Jin, Y.; Wang, Y.; Chen, G.; Gu, N.; Wang, C. Potential Osteoinductive Effects of Hydroxyapatite Nanoparticles on Mesenchymal Stem Cells by Endothelial Cell Interaction. *Nanoscale Res. Lett.* **2021**, *16*, 67. [CrossRef] [PubMed]
14. Ribeiro, M.; Monteiro, F.J.; Ferraz, M.P. Infection of Orthopedic Implants with Emphasis on Bacterial Adhesion Process and Techniques Used in Studying Bacterial-Material Interactions. *Biomatter* **2012**, *2*, 176–194. [CrossRef] [PubMed]
15. Campoccia, D.; Montanaro, L.; Arciola, C.R. The Significance of Infection Related to Orthopedic Devices and Issues of Antibiotic Resistance. *Biomaterials* **2006**, *27*, 2331–2339. [CrossRef]
16. Mosina, M.; Kovrlija, I.; Stipniece, L.; Locs, J. Gallium Containing Calcium Phosphates: Potential Antibacterial Agents or Fictitious Truth. *Acta Biomater.* **2022**, *150*, 48–57. [CrossRef]
17. Coppey, E.; Mommaerts, M.Y. Early Complications from the Use of Calcium Phosphate Paste in Mandibular Lengthening Surgery. A Retrospective Study. *J. Oral Maxillofac. Surg.* **2017**, *75*, 1274.e1–1274.e10. [CrossRef]
18. Mokabber, T. *Electrochemically Deposited Antimicrobial Hydroxyapatite Coatings*; University of Groningen: Groningen, The Netherlands, 2020. [CrossRef]
19. Jiang, Y.; Yuan, Z.; Huang, J. Substituted Hydroxyapatite: A Recent Development. *Mater. Technol.* **2020**, *35*, 785–796. [CrossRef]
20. Stötzel, C.; Müller, F.A.; Reinert, F.; Niederdraenk, F.; Barralet, J.E.; Gbureck, U. Ion Adsorption Behaviour of Hydroxyapatite with Different Crystallinities. *Colloids Surf. B Biointerfaces* **2009**, *74*, 91–95. [CrossRef] [PubMed]
21. Wang, L.; Hu, C.; Shao, L. The Antimicrobial Activity of Nanoparticles: Present Situation and Prospects for the Future. *Int. J. Nanomed.* **2017**, *12*, 1227–1249. [CrossRef]
22. Chernousova, S.; Epple, M. Silver as Antibacterial Agent: Ion, Nanoparticle, and Metal. *Angew. Chem.-Int. Ed.* **2013**, *52*, 1636–1653. [CrossRef]
23. Shanmugam, S.; Gopal, B. Copper Substituted Hydroxyapatite and Fluorapatite: Synthesis, Characterization and Antimicrobial Properties. *Ceram. Int.* **2014**, *40*, 15655–15662. [CrossRef]
24. Jacobs, A.; Renaudin, G.; Forestier, C.; Nedelec, J.M.; Descamps, S. Biological Properties of Copper-Doped Biomaterials for Orthopedic Applications: A Review of Antibacterial, Angiogenic and Osteogenic Aspects. *Acta Biomater.* **2020**, *117*, 21–39. [CrossRef]
25. Mouriño, V.; Cattalini, J.P.; Boccaccini, A.R. Metallic Ions as Therapeutic Agents in Tissue Engineering Scaffolds: An Overview of Their Biological Applications and Strategies for New Developments. *J. R. Soc. Interface* **2012**, *9*, 401–419. [CrossRef]
26. Kircheva, N.; Dudev, T. Gallium as an Antibacterial Agent: A DFT/SMD Study of the Ga^{3+}/Fe^{3+} Competition for Binding Bacterial Siderophores. *Inorg. Chem.* **2020**, *59*, 6242–6254. [CrossRef] [PubMed]
27. Kelson, A.B.; Carnevali, M.; Truong-Le, V. Gallium-Based Anti-Infectives: Targeting Microbial Iron-Uptake Mechanisms. *Curr. Opin. Pharmacol.* **2013**, *13*, 707–716. [CrossRef] [PubMed]
28. Qiu, C.; Lu, T.; He, F.; Feng, S.; Fang, X.; Zuo, F.; Jiang, Q.; Deng, X.; Ye, J. Influences of Gallium Substitution on the Phase Stability, Mechanical Strength and Cellular Response of β-Tricalcium Phosphate Bioceramics. *Ceram. Int.* **2020**, *46*, 16364–16371. [CrossRef]
29. Kurtjak, M.; Vukomanović, M.; Krajnc, A.; Kramer, L.; Turk, B.; Suvorov, D. Designing Ga(III)-Containing Hydroxyapatite with Antibacterial Activity. *RSC Adv.* **2016**, *6*, 112839–112852. [CrossRef]
30. Wren, A.W.; Jones, M.C.; Misture, S.T.; Coughlan, A.; Keenan, N.L.; Towler, M.R.; Hall, M.M. A Preliminary Investigation into the Structure, Solubility and Biocompatibility of Solgel SiO_2-CaO-Ga_2O_3 Glass-Ceramics. *Mater. Chem. Phys.* **2014**, *148*, 416–425. [CrossRef]
31. Lemire, J.A.; Harrison, J.J.; Turner, R.J. Antimicrobial Activity of Metals: Mechanisms, Molecular Targets and Applications. *Nat. Rev. Microbiol.* **2013**, *11*, 371–384. [CrossRef]
32. Kaneko, Y.; Thoendel, M.; Olakanmi, O.; Britigan, B.E.; Singh, P.K. The Transition Metal Gallium Disrupts Pseudomonas Aeruginosa Iron Metabolism and Has Antimicrobial and Antibiofilm Activity. *J. Clin. Investig.* **2007**, *117*, 877–888. [CrossRef]
33. Kurtjak, M.; Vukomanović, M.; Suvorov, D. Antibacterial Nanocomposite of Functionalized Nanogold and Gallium-Doped Hydroxyapatite. *Mater. Lett.* **2017**, *193*, 126–129. [CrossRef]
34. Rzhepishevska, O.; Ekstrand-Hammarström, B.; Popp, M.; Björn, E.; Bucht, A.; Sjöstedt, A.; Antti, H.; Ramstedt, M. The Antibacterial Activity of Ga^{3+} Is Influenced by Ligand Complexation as Well as the Bacterial Carbon Source. *Antimicrob. Agents Chemother.* **2011**, *55*, 5568–5580. [CrossRef] [PubMed]
35. Rubenis, K.; Zemjane, S.; Vecstaudza, J.; Bitenieks, J.; Locs, J. Densification of Amorphous Calcium Phosphate Using Principles of the Cold Sintering Process. *J. Eur. Ceram. Soc.* **2021**, *41*, 912–919. [CrossRef]
36. Smits, K.; Grigorjeva, L.; Millers, D.; Kundzins, K.; Ignatans, R.; Grabis, J.; Monty, C. Luminescence Properties of Zirconia Nanocrystals Prepared by Solar Physical Vapor Deposition. *Opt. Mater.* **2014**, *37*, 251–256. [CrossRef]
37. Meredith, D.O.; Eschbach, L.; Wood, M.A.; Riehle, M.O.; Curtis, A.S.G.; Richards, R.G. Human Fibroblast Reactions to Standard and Electropolished Titanium and Ti-6Al-7Nb, and Electropolished Stainless Steel. *J. Biomed. Mater. Res.-Part A* **2005**, *75*, 541–555. [CrossRef]
38. Indrani, D.J.; Soegijono, B.; Adi, W.A.; Trout, N. Phase Composition and Crystallinity of Hydroxyapatite with Various Heat Treatment Temperatures. *Int. J. Appl. Pharm.* **2017**, *9*, 87–91. [CrossRef]

39. Matsumoto, T.; Tamine, K.I.; Kagawa, R.; Hamada, Y.; Okazaki, M.; Takahashi, J. Different Behavior of Implanted Hydroxyapatite Depending on Morphology, Size and Crystallinity. *J. Ceram. Soc. Jpn.* **2006**, *114*, 760–762. [CrossRef]
40. Ślósarczyk, A.; Paszkiewicz, Z.; Paluszkiewicz, C. FTIR and XRD Evaluation of Carbonated Hydroxyapatite Powders Synthesized by Wet Methods. *J. Mol. Struct.* **2005**, *744–747*, 657–661. [CrossRef]
41. Michelot, A.; Sarda, S.; Audin, C.; Deydier, E.; Manoury, E.; Poli, R.; Rey, C. Spectroscopic Characterisation of Hydroxyapatite and Nanocrystalline Apatite with Grafted Aminopropyltriethoxysilane: Nature of Silane–Surface Interaction. *J. Mater. Sci. Vol.* **2015**, *50*, 5746–5757. [CrossRef]
42. Pajor, K.; Pajchel, Ł.; Zgadzaj, A.; Piotrowska, U.; Kolmas, J. Modifications of Hydroxyapatite by Gallium and Silver Ions—Physicochemical Characterization, Cytotoxicity and Antibacterial Evaluation. *Int. J. Mol. Sci.* **2020**, *21*, 5006. [CrossRef]
43. Melnikov, P.; de Fatima Cepa Matos, M.; Malzac, A.; Rainho Teixeira, A.; de Albuquerque, D.M. Evaluation of In Vitro Toxicity of Hydroxyapatite Doped with Gallium. *Mater. Lett.* **2019**, *253*, 343–345. [CrossRef]
44. Zhang, T.; Xiao, X. Hydrothermal Synthesis of Hydroxyapatite Assisted by Gemini Cationic Surfactant. *J. Nanomater.* **2020**, *2020*, 5006. [CrossRef]
45. In, Y.; Amornkitbamrung, U.; Hong, M.H.; Shin, H. On the Crystallization of Hydroxyapatite under Hydrothermal Conditions: Role of Sebacic Acid as an Additive. *ACS Omega* **2020**, *5*, 27204–27210. [CrossRef] [PubMed]
46. Blumenthal, N.C.; Cosma, V.; Levine, S. Effect of Gallium on the in Vitro Formation, Growth, and Solubility of Hydroxyapatite. *Calcif. Tissue Int.* **1989**, *45*, 81–87. [CrossRef] [PubMed]
47. Tite, T.; Popa, A.C.; Balescu, L.M.; Bogdan, I.M.; Pasuk, I.; Ferreira, J.M.F.; Stan, G.E. Cationic Substitutions in Hydroxyapatite: Current Status of the Derived Biofunctional Effects and Their in Vitro Interrogation Methods. *Materials* **2018**, *11*, 2081. [CrossRef] [PubMed]
48. Vrchovecká, K.; Pávková-Goldbergová, M.; Engqvist, H.; Pujari-Palmer, M. Cytocompatibility and Bioactive Ion Release Profiles of Phosphoserine Bone Adhesive: Bridge from In Vitro to In Vivo. *Biomedicines* **2022**, *10*, 736. [CrossRef]
49. Mocanu, A.; Cadar, O.; Frangopol, P.T.; Petean, I.; Tomoaia, G.; Paltinean, G.-A.; Racz, C.P.; Horovitz, O.; Tomoaia-Cotisel, M. Ion Release from Hydroxyapatite and Substituted Hydroxyapatites in Different Immersion Liquids: In Vitro Experiments and Theoretical Modelling Study. *R. Soc. Open Sci.* **2021**, *8*, 201785. [CrossRef]
50. Koppala, S.; Swamiappan, S.; Gangarajula, Y.; Xu, L.; Sadasivuni, K.K.; Ponnamma, D.; Rajagopalan, V. Calcium Deficiency in Hydroxyapatite and Its Drug Delivery Applications. *Micro Nano Lett.* **2018**, *13*, 562–564. [CrossRef]
51. Minandri, F.; Bonchi, C.; Frangipani, E.; Imperi, F.; Visca, P. Promises and Failures of Gallium as an Antibacterial Agent. *Future Microbiol.* **2014**, *9*, 379–397. [CrossRef]
52. Silhavy, T.J.; Kahne, D.; Walker, S. The Bacterial Cell Envelope. *Cold Spring Harb. Perspect. Biol.* **2010**, *2*, a000182. [CrossRef]
53. Gasser, V.; Kuhn, L.; Hubert, T.; Aussel, L.; Hammann, P.; Schalk, I.J. The Esterase PfeE, the Achilles' Heel in the Battle for Iron between Pseudomonas Aeruginosa and Escherichia Coli. *Int. J. Mol. Sci.* **2021**, *22*, 2814. [CrossRef]
54. Ballardini, A.; Montesi, M.; Panseri, S.; Vandini, A.; Balboni, P.G.; Tampieri, A.; Sprio, S. New Hydroxyapatite Nanophases with Enhanced Osteogenic and Anti-Bacterial Activity. *J. Biomed. Mater. Res. Part A* **2018**, *106*, 521–530. [CrossRef] [PubMed]
55. Kircheva, N.; Dudev, T. Competition between Abiogenic and Biogenic Metal Cations in Biological Systems: Mechanisms of Gallium's Anticancer and Antibacterial Effect. *J. Inorg. Biochem.* **2021**, *214*, 111309. [CrossRef] [PubMed]
56. Lessa, J.A.; Parrilha, G.L.; Beraldo, H. Gallium Complexes as New Promising Metallodrug Candidates. *Inorg. Chim. Acta* **2012**, *393*, 53–63. [CrossRef]
57. Gómez-Cerezo, N.; Verron, E.; Montouillout, V.; Fayon, F.; Lagadec, P.; Bouler, J.M.; Bujoli, B.; Arcos, D.; Vallet-Regí, M. The Response of Pre-Osteoblasts and Osteoclasts to Gallium Containing Mesoporous Bioactive Glasses. *Acta Biomater.* **2018**, *76*, 333–343. [CrossRef] [PubMed]

Appendix IV

Influence of gallium doping on the thermal stability and microstructure of sintered hydroxyapatite bioceramics

Marika Sceglova, Nicola Döbelin, Renats Vasiljevs, Liga Stipniece, Janis Locs.

Ceramics International, **2025**, 51(14), 41150-42261. doi: 10.1016/j.ceramint.2025.06.440

M.S. input: conceptualization, investigation, data curation, formal analysis, visualization, writing the original draft, reviewing and editing

Ceramics International 51 (2025) 42250–42261

Contents lists available at ScienceDirect

Ceramics International

journal homepage: www.elsevier.com/locate/ceramint

Influence of gallium doping on the thermal stability and microstructure of sintered hydroxyapatite bioceramics

Marika Sceglova [a,b], Nicola Döbelin [c], Renats Vasiljevs [a,b], Liga Stipniece [a,b,*], Janis Locs [a,b,**]

[a] Riga Technical University Faculty of Natural Sciences and Technology, Institute of Biomaterials and Bioengineering, Paula Valdena Street 3-K1, Riga, LV-1048, Latvia
[b] Baltic Biomaterials Centre of Excellence, Headquarters at Riga Technical University, Riga, Latvia
[c] RMS Foundation, Bischmattstrasse 12, 2544, Bettlach, Switzerland

ARTICLE INFO

Handling Editor: Dr P. Vincenzini

Keywords:
Hydroxyapatite
Gallium substitution
Sinterability
Bioceramics
Rietveld refinement

ABSTRACT

Calcium phosphates (CaPs) are extensively used in the biomedical field for bone regeneration applications. Hydroxyapatite (HAp), the main component of human bone, has been successfully used as a bone graft material. Partial calcium (Ca) substitution with gallium (Ga) can influence HAp's physicochemical properties and biological activity. In this study, Ga-doped Ca-deficient HAp (GaCDHAp) powders containing 1.6 ± 0.1 and 3.3 ± 0.4 wt% Ga were synthesized using wet chemical precipitation. Bioceramics were prepared from the synthesized GaCDHAp powders using uniaxial compaction and sintering at temperatures between 600 and 1200 °C. The quantitative phase composition and the Ga substitution in the HAp lattice were investigated by *Rietveld* refinement. It was observed that the sintering of the GaCDHAp led to the formation of biphasic CaP bioceramics composed of HAp and α-TCP. The secondary phase inhibited the densification, leading to a microporous structure of GaHAp bioceramics. Structure refinement showed that Ga substituted Ca on the Ca1 site in the HAp lattice. Charge balance was maintained by an additional partially occupied oxygen site in the structural channel.

1. Introduction

Calcium phosphate (CaP) bioceramics have been used in hard tissue reconstruction since 1980 [1]. Hydroxyapatite (HAp) is a naturally occurring CaP mineral and the main mineral component of human bone. This similarity in composition confers HAp-based biomaterials osteoconductivity, allowing integration within bone tissues. Thus, for decades, HAp-based biomaterials have been widely used for applications in bone repair, replacement, and tissue engineering [1–4]. The range of HAp-based materials is extensive and constantly expanding [5]. In the case of HAp bioceramics, numerous factors, *e.g.*, preparation and processing methods, influence their performance. Moreover, HAp has the capacity for ion exchange, and doping with different metal ions has enhanced its biological properties [6–9]. These dopants affect the physicochemical properties of HAp, which determine the possibilities of processing and application of new materials [10]. Different ions, such as magnesium (Mg), zinc (Zn), and strontium (Sr), promote the formation of secondary phases during the sintering of HAp [11–13]. The secondary phase in the form of tricalcium phosphate (TCP) can influence the biodegradability of CaP bioceramics.

Among others, due to its compelling biological properties, gallium (Ga) as a dopant has seen an increasing interest in the biomaterials field. Ga compounds are currently investigated as effective antibacterial and promising anticancer agents [14,15]. Ga^{3+} mimics iron (Fe^{3+}) in biological processes, thus disrupting iron-dependent processes in tumor cells and bacteria, leading to cell death [16,17]. In the material science field, multiple materials doped with Ga are being investigated, such as bioglass [18], CaPs [19,20], and composites [19,20]. The study focuses on Ga-containing CaPs (GaCaPs), which have shown promising results against different bacteria [21–23]. *Kurtjak* et al. studied different formulations of Ga-doped HAp (GaHAp) and revealed an antibacterial effect against *Pseudomonas aeruginosa* (*P. aeruginosa*) by the disc diffusion method [24,25]. *Pajor* et al. showed antibacterial properties of Ga and silver (Ag) functionalised HAp against *Pseudomonas fluorescens* (*P. fluorescens*) by the disc diffusion method [9]. *Shokri* et al. studied the synergy of Ga and Zn in HAp doping. By increasing the Ga concentration, they disclosed the enhanced antibacterial properties of Ga-doped or Zn- and Ga-co-doped HAp (ZnGaHAp). The results show reduced

* Corresponding author. Riga Technical University Faculty of Natural Sciences and Technology, Institute of Biomaterials and Bioengineering, Paula Valdena Street 3-K1, Riga, LV-1048, Latvia.
** Corresponding author. Baltic Biomaterials Centre of Excellence, Headquarters at Riga Technical University, Riga, Latvia.
E-mail addresses: liga.stipniece@rtu.lv (L. Stipniece), janis.locs@rtu.lv (J. Locs).

https://doi.org/10.1016/j.ceramint.2025.06.440
Received 23 April 2025; Received in revised form 27 June 2025; Accepted 28 June 2025
Available online 28 June 2025

cell viability of *S. aureus* from 48 % to 6 % and *E. coli* from 57 % to 18 %. Additionally, by increasing the concentration of Ga, the viability of human mesenchymal stem cells (hMSCs) decreased compared to that of undoped HAp; however, it retained cell viability above 70 % [26]. GaCaP used as a coating for MgCa alloy reduced degradation of the alloy and promoted the formation of new bone in sheep cranial defects [27]. *Ngoc Huu* et al. introduced a multifunctional biomaterial sintered at 1200 °C, where the HAp pellets were covered with liquid Ga and Ag nanoparticles or their combination. *In vivo* findings indicate a significant reduction of bacterial growth in the presence of HAp-Ag-GaNPs in the infected cranial defects model [28].

The studies available in the literature on Ga doping mainly focus on low-crystallinity (heat-treatment temperature does not exceed 100 °C) HAp synthesized by various methods [9,22,23,26,29–32]. It has generally been observed that GaHAp has a characteristic hexagonal structure and a decrease in crystallinity with increasing Ga concentration [9,22,23,26,29–32]. *Mellier* et al. studied Ga^{3+} influence on β-TCP ceramic obtained at 1000 °C and observed a reduction in unit cell volume with increasing Ga^{3+} concentration [21]. However, there is a shortage of information on the effect of Ga^{3+} on the high-temperature behavior of HAp (heat-processed above 600 °C). In this study, systematic and complex analyses of coherence between Ga substitution and sintering temperature of the HAp bioceramics were performed for the first time.

In our previous study, we evaluated the effect of Ga on the physicochemical and biological characteristics of HAp nanoparticles (low crystalline). The GaHAp with 2–8 wt% of Ga showed bacteriostatic properties against *P. aeruginosa* and *S. aureus*. However, when the Ga was above 4 wt%, the GaHAp showed a significant decrease in fibroblast cell viability on day 7 [29]. Accordingly, the optimal doping level of Ga was 2–4 wt%, which was used for doping the GaHAp bioceramics in this study. Insight into how Ga alters crystallinity and structural characteristics during sintering is crucial to expand the possibilities of using the GaHAp in developing new biomaterials. For the first time, the in-depth justification and the substitution behavior of Ga in the HAp crystal lattice were explored to gain deeper insights into the properties of GaHAp bioceramics.

2. Materials and methods

2.1. Synthesis of Ga-doped HAp powders

Ga-doped HAp (GaHAp) powders were synthesized using wet chemical precipitation from calcium oxide (CaO, >98 %, *Jost Chemical*, USA), orthophosphoric acid (H_3PO_4, 75 %, *Latvijas kimija Ltd.*, Latvia), and gallium nitrate hydrate ($Ga(NO_3)_3{\cdot}xH_2O$, 99.9 % trace metal, *Sigma-Aldrich*, USA) as described in Ref. [29]. To calculate the required amount of $Ga(NO_3)_3{\cdot}xH_2O$, the number of water molecules was determined using an inductively coupled plasma mass spectrometry (ICP-MS, *Agilent 7700X*, USA). Thus, the $Ga(NO_3)_3{\cdot}9.95H_2O$ was used as a source of Ga^{3+} ions.

Synthesis was performed in the *IKA EUROSTAR Power Control-Visc P7* (*Ika-Werke,* Germany) synthesis reactor equipped with an anchor stirrer, following the procedure below. First, the starting suspension, 0.44M $Ca(OH)_2$, was prepared by dispersing CaO in the deionized H_2O (Eq. (1)):

$$CaO + H_2O \rightarrow Ca(OH)_2 \quad (1)$$

The starting suspension was heated to 45 °C and this temperature was maintained using a laboratory hot plate with an external temperature probe. Second, the $Ga(NO_3)_3{\cdot}9.95H_2O$ powder was added to the $Ca(OH)_2$ and stirred at 100 rpm for 5 min. The nominal Ga concentrations in the synthesis were 2 wt% (2GaHAp) and 4 wt% (4GaHAp) of the theoretical HAp yield. The sample series is designated according to the nominal Ga concentration. Third, an aqueous solution of 2M H_3PO_4 was added to the starting suspension at an addition rate of 1 mL/min using an automated dosing unit (*TITRONIC® universal, Schott*, Germany) until the pH 6.70 ± 0.05 was reached. The (Ca + Ga)/P molar ratio of the reagents was 1.67 (for pure HAp, Ca/P molar ratio was 1.67). The molar ratio was the same for all the synthesis series. Reaction occurs according to Eq. (2):

$$(10\text{-}x)Ca(OH)_2 + xGa(NO_3)_3{\cdot}9.95H_2O + 6H_3PO_4 \rightarrow Ca_{10\text{-}x}Ga_x(\text{-}PO_4)_6(OH)_{2\text{-}x}O_x + 3xHNO_3 + (18 + 7.95x)H_2O \quad (2)$$

where $x = 0.3$ (for 2GaHAp), 0.6 (for 4GaHAp), calculated, considering that 2 and 4 wt% are the nominal amount of Ga from the total product yield.

Obtained precipitates were aged in mother liquors at ambient temperature overnight (approximately 20 h). After aging, the precipitates were vacuum-filtered and washed with 1 L of deionized water. Filtered precipitates were dried in an oven at 105 °C for 24 h. Dried precipitates were crushed in a pestle to obtain a fine powder (bioceramic precursor powder). The HAp synthesized without $Ga(NO_3)_3{\cdot}9.95H_2O$ was used as a reference (sample series designated as HAp). To ensure the reproducibility of the syntheses, each composition was synthesized in triplicate.

2.2. Preparation of the bioceramics

To prepare a bioceramic pellet, 0.5 g of the as-synthesized powder was transferred to a cylindrical die of 13 mm diameter and compacted at a uniaxial compression force of 100 MPa for 1 min. The compacted pellets (disks) were sintered at 600, 700, 800, 900, 1000, 1100, and 1200 °C with a heating/cooling rate of 5 °C/min and a holding time of 1 h.

2.3. Physicochemical characterisation

2.3.1. X-ray diffraction analysis

The phase composition of the as-synthesized powders and the heat-treated (600–1200 °C) powders was analyzed using X-ray diffractometry (XRD, *PANalytical*, AERIS, The Netherlands). Before analysis, the heated powders were ground in a mortar to remove aggregates that may have formed due to temperature-induced sintering of the particles. XRD patterns were recorded in a 2θ range from 10 to 70°, with a step size of 0.0435°, using a Ni-filter and Cu Kα radiation at 40 kV and 15 mA.

The quantitative phase composition and Ga substitution in the HAp structure were studied by *Rietveld* refinement with the software *Profex* [33]. Structure models were taken from the ICDD PDF-4+ database version 2023 [34] for hexagonal HAp (PDF# 01-074-0565), monoclinic HAp (PDF# 01-076-0694), and α-TCP (PDF# 04-010-4348). For α-TCP, the scale factor, cell parameters, and crystallite-size-related peak broadening were refined. For HAp, the scale factor, cell parameters, crystallite-size- and micro-strain-related peak broadening, and preferred orientation were refined. The crystallite size was determined from complete refinement of the full pattern using the crystallite size estimation model implemented in *Profex's Rietveld* refinement kernel BGMN [35]. Unit cell volume was calculated using Eq. (3) for the hexagonal structure and Eq. (4) for the monoclinic structure [35]:

$$V = \frac{\sqrt{3}a^2c}{2} \quad (3)$$

where a, c – unit cell parameters

$$V = abc\sin\gamma \quad (4)$$

where a, b, c – unit cell parameters, γ - monoclinic angle.

To locate Ga substitution in the HAp crystal lattice, a complete structure refinement of the 4GaHAp heat-treated at 1100 °C was performed, including refinement of Ca site occupancy factors, fractional coordinates, and thermal displacement parameters. This dataset was selected based on its high Ga substitution and processing temperature,

Table 1
Designation of the sample series, Ga concentration measured using ICP-MS (NM – not measured), and *Rietveld* refinement results of phase composition (errors of phase quantities represent standard deviations of triplicate measurements).

Sample series	Nominal Ga conc., wt %	Measured Ga conc., wt %	Heat treatment temp., °C	HAp, %	α-TCP, %	HAp crystallite size, nm	α-TCP crystallite size, nm
HAp	0	–	as-synthesized	100	0	16.5 ± 1.3 (1,0,0) 47.0 ± 5.5 (0,0,1)	–
		–	800	100	0	77 ± 4	–
		–	900	100	0	100 ± 3	–
		–	1000	99.6 ± 0.5	0.4 ± 0.5	154 ± 15	NM
		–	1100	99.3 ± 0.8	0.7 ± 0.8	247 ± 22	NM
		–	1200	99.2 ± 1.4	0.8 ± 1.4	264 ± 27	NM
2GaHAp	2	1.6 ± 0.1	as-synthesized	100	0	11.0 ± 0.3 (1,0,0) 30.5 ± 0.2 (0,0,1)	–
		NM	800	100	0	37 ± 1	–
		NM	900	90.1 ± 3.3	9.9 ± 3.3	69 ± 2	–
		NM	1000	84.4 ± 1.7	15.6 ± 1.7	85 ± 0	145 ± 17
		NM	1100	80.1 ± 1.5	19.9 ± 1.5	112 ± 6	136 ± 14
		NM	1200	72.3 ± 7.2	27.7 ± 7.2	175 ± 32	148 ± 22
4GaHAp	4	3.3 ± 0.4	as-synthesized	100	0	9.3 ± 0.2 (1,0,0) 25.6 ± 0.3 (0,0,1)	–
		3.6 ± 0.4	800	100	0	32 ± 4	–
		3.6 ± 0.4	900	87.0 ± 5.5	13.0 ± 5.5	62 ± 6	–
		NM	1000	82.1 ± 4.5	17.9 ± 4.5	85 ± 0	145 ± 23
		3.7 ± 0.4	1100	72.8 ± 4.3	27.2 ± 4.3	97 ± 5	122 ± 4
		NM	1200	70.1 ± 7.2	29.9 ± 7.2	150 ± 30	136 ± 25

allowing for a relatively reliable structure refinement. Difference *Fourier* maps of the refined structure were created with the Electron Density Map module in *Profex*.

2.3.2. Inductively coupled plasma mass spectrometry

Inductively coupled plasma mass spectrometry (ICP-MS) (7700X, *Agilent*, USA) was used to measure Ga concentration. The powders were dissolved in deionized H_2O (*Synergy 185, Millipore,* MA, USA) and high-purity HNO_3 (65 %, *ChemLab*, Belgium) solution for at least 20 min at room temperature. Then, suspensions were microwaved at 150 °C for 30 min (heating rate 5 °C/min) to facilitate the complete dissolution of the solid particles. The obtained solutions were cooled and filtered through a filter with a pore size of 12–15 μm to eliminate solid phase impurities.

2.3.3. Fourier transformation infrared spectroscopy

The functional groups of the as-synthesized powders and the heat-treated (600–1200 °C) powders were analyzed using *Fourier* transform infrared spectroscopy (FTIR, *Thermo Fisher Scientific*, USA). Before analysis, the heated powders were ground in a mortar to remove aggregates that may have formed due to temperature-induced sintering of the particles. Spectra were recorded in attenuated total reflectance (ATR) mode. Spectra were obtained at a resolution of 4 cm^{-1} over a range of wavenumbers from 400 cm^{-1} to 4000 cm^{-1}, by co-adding 64 scans. Before every measurement, a background spectrum was taken and subtracted from the sample spectrum.

2.3.4. Thermal analysis

The thermal properties of the as-synthesized powders were determined with thermogravimetric analysis (TGA) (*TGA/DSC 3+, Mettler Toledo,* Switzerland). Approximately 10 mg of the sample was placed into an alumina crucible and heated to 1200 °C at 10 °C/min under an airflow of 10 mL/min.

2.3.5. Scanning electron microscopy and energy dispersive X-ray analysis

The surface morphology of the GaHAp bioceramics pellets was analyzed using a high-resolution field emission scanning electron microscope (*FE-SEM/STEM, Verios 5 UC, Thermo Fisher*). SEM imaging was performed at an accelerating voltage of 2 kV, utilizing through-lens and *Everhart-Thornley* detectors to capture detailed surface features. A low beam current and vector scanning mode were employed to minimize charging effects and potential sample damage, with a dwell time of 50 ns. Before imaging, the samples were coated with a 10 nm carbon layer (calculated for a completely flat Si wafer surface) using a *LEICA EM ACE 200* coater. Other processing of the bioceramics pellet samples was not done. The carbon coating thickness was doubled for energy-dispersive X-ray spectroscopy (EDX) analysis. EDX was performed at 20 kV and 1.6 nA using an *Oxford Instruments X-Max 150* detector.

2.3.6. Density measurement by Archimedes' method and bulk density

The apparent density and open porosity of sintered bioceramics were determined using the *Archimedes* principle and a density determination kit (*YDK 01, Sartorius AG*, Germany). First, the samples were weighed and transferred to a vessel for impregnation with water. Then, the vacuum was applied (the air was pumped out from the vessel using a vacuum pump) for 30 min. Samples were poured with water under vacuum and impregnated for 30 min following increased pressure in the chamber, reaching atmospheric pressure. Afterwards, the samples were transferred to the density determination kit and weighed in water and air. The apparent density (d_A) was calculated using Eq. (5):

$$d_A = \frac{m_d{}^* \rho_{liquid}}{m_1 - m_2}, \tag{5}$$

where m_d - a mass of the dry sample (g), ρ_{liquid} - a density of water (g/cm^3), m_1 - a mass of the water-impregnated sample in the air (g), m_2 - a mass of the water-impregnated sample in water (g).

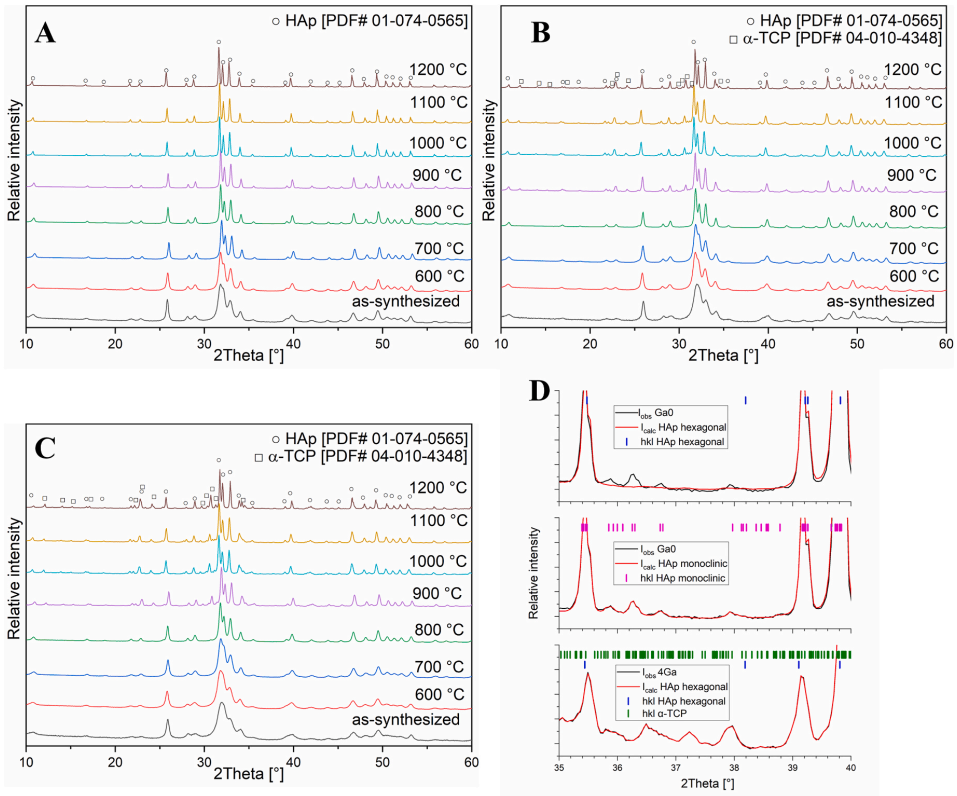

Fig. 1. XRD patterns of the A – Ga-free HAp, B – 2GaHAp, C – 4GaHAp powders heat-treated at temperatures ranging from 600 to 1200 °C, D – XRD patterns at 35–40° 2Theta range of the HAp and 4GaHAp powders heat-treated at 1100 °C, revealing maxima of monoclinic structure (I_{obs} – observed intensity, I_{calc} – calculated intensity).

The open porosity (P_{Op}) was calculated using Eq. (6):

$$P_{Op} = \frac{m_1 - m_d}{m_1 - m_2} * 100, \quad (6)$$

where m_d - the mass of the dry sample (g), m_1 - the mass of the water-impregnated sample in the air (g), m_2 - the mass of the water-impregnated sample in water (g). The bulk density of the green bodies (ρ_0) and sintered bioceramics (ρ) was calculated by dividing the sample mass by its bulk volume (V_{bulk}). The bulk volume was calculated using Eq. (7):

$$V_{bulk} = \frac{\pi d^2 h}{4}, \quad (7)$$

where d and h are the average diameter and height of the sample, respectively, measured using a digital caliper for five samples.

The shrinkage (Sh) of the bioceramics after sintering was determined using Eq. (8):

$$Sh = \frac{d_b - d_a}{d_a} * 100, \quad (8)$$

where d_b and d_a are the sample diameters before and after heat treatment, respectively.

3. Results

3.1. Chemical and phase composition

The measured Ga concentrations of the as-synthesized powders are summarized in Table 1. The measured Ga concentrations were close to the theoretically planned or nominal ones. ICP-MS (see 4GaHAp in Table 1) and EDX (Supplementary material, Table S1) analysis confirmed that Ga concentration in the samples does not change after heat treatment.

The phase composition of the HAp and the GaHAp before and after heat treatment at temperatures ranging from 600 to 1200 °C is shown in XRD patterns (Fig. 1(A–C)). Relatively broad and merged XRD diffraction maxima characteristic of the hexagonal HAp phase (PDF# 01-074-0565) indicated low crystallinity of the as-synthesized powders. Furthermore, with increasing Ga concentration, the crystallinity of HAp decreased with temperature increase, as indicated by the broadening of the characteristic XRD diffraction maxima, especially the triplet of (2,1,1), (1,1,2), and (3,0,0) between 30 and 35° 2Theta. The XRD diffraction reveals the formation of a secondary phase that corresponds to the α-TCP phase (PDF# 04-010-4348). In addition, the content of the secondary phase increased with increasing Ga concentration (Fig. 1 (A–C), Table 1).

The crystallite size of HAp is displayed in Table 1. The (0,0,l) diffraction maxima of the as-synthesized powders were less affected by

Table 2
Cell parameters (a, b, c), cell volume (V) of HAp and α-TCP, and crystallite size of α-TCP from complete *Rietveld* refinement of full structure (errors represent standard deviations of triplicate measurements).

Heat treatment temp. °C	Sample	HAp				α-TCP			
		a, Å	b, Å	c, Å	Unit cell V, Å^3	a, Å	b, Å	c, Å	Unit cell V, Å^3
1000	HAp	9.430 ± 0.002	18.775 ± 0.149	6.887 ± 0.002	530.398 ± 0.181	–	–	–	–
	2GaHAp	9.433 ± 0.001	–	6.902 ± 0.002	531.892 ± 0.264	12.890 ± 0.000	27.311 ± 0.002	15.237 ± 0.001	4330.196 ± 0.847
	4GaHap	9.433 ± 0.001	–	6.904 ± 0.002	532.081 ± 0.345	12.8904 ± 0.006	27.311 ± 0.005	15.238 ± 0.001	4330.325 ± 0.808
1100	HAp	9.427 ± 0.001	18.854 ± 0.001	6.886 ± 0.000	529.943 ± 0.047	–	–	–	–
	2GaHAp	9.431 ± 0.002	–	6.907 ± 0.001	532.049 ± 0.376	12.891 ± 0.006	27.306 ± 0.003	15.266 ± 0.005	4337.146 ± 14.606
	4GaHAp	9.431 ± 0.000	–	6.925 ± 0.001	533.387 ± 0.097	12.884 ± 0.000	27.305 ± 0.000	15.231 ± 0.001	4324.93 ± 0.465
1200	HAp	9.427 ± 0.002	18.852 ± 0.002	6.887 ± 0.001	529.956 ± 0.150	–	–	–	–
	2GaHAp	9.430 ± 0.001	–	6.919 ± 0.018	532.812 ± 1.399	12.887 ± 0.005	27.645 ± 0.586	15.231 ± 0.003	4424.457 ± 89.498
	4GaHAp	9.432 ± 0.001	–	6.936 ± 0.007	534.387 ± 0.617	12.886 ± 0.001	27.313 ± 0.004	15.232 ± 0.001	4326.896 ± 0.871

Fig. 2. Refined unit cell volume of the HAp and GaHAp bioceramic heat-treated at 1000, 1100, and 1200 °C as a function of the nominal Ga concentration. The volumes of the monoclinic HAp phase at 0 wt% Ga were divided by 2 to represent a domain equivalent to the hexagonal unit cell.

broadening than all other diffraction maxima, hence requiring refinement of anisotropic crystallite sizes. Datasets of the heat-treated samples were refined with isotropic crystallite sizes. Crystallite size decreased with increasing Ga concentration, and at the highest temperatures (1000–1200 °C), crystallite size was approximately 1.5 times smaller compared to HAp.

Cell parameters (a, b, c), cell volume (V) of HAp and α-TCP heat-treated above 1000 °C are displayed in Table 2. In the literature, reported values of hexagonal HAp are $a = b = 9.432$ Å, $c = 6.881$ Å [36], and of monoclinic HAp – $a = 9.4214$ Å, $b = 2a$, $c = 6.8814$ Å [36]. Accordingly, our results showed that the unit cell parameter c and the volume of the unit cell of HAp increased with increasing Ga concentration (Fig. 2), suggesting that Ga^{3+} ions were incorporated into the HAp crystal lattice.

The unit cell parameter of α-TCP, shown in Table 2, was not affected by Ga^{3+} substitution and is within the range reported in the literature. Unit cell parameters of α-TCP are reported to be $a = 12.881$ Å, $b = 27.290$ Å, $c = 15.221$ Å by *Stahl* et al. [37], $a = 12.859$ Å, $b = 27.354$ Å, $c = 15.222$ Å by *Tronco* et al. [38], and $a = 12.859$ Å, $b = 27.354$ Å, $c = 15.222$ Å by *Yashima* et al. [39]. The calculated unit cell volume from cell parameters of the α-TCP formed as a secondary phase was higher than reported in the literature, namely, 4310.59 Å3, by *Yashima* et al. [40]. However, it was uncertain to conclude Ga's influence on the α-TCP structure as the phase had a weak diffraction maximum.

3.1.1. Theoretical Ga substitution in the HAp structure

XRD datasets of the HAp heat-treated at 900, 1000, 1100, and 1200 °C showed monoclinic apatite diffraction maxima at 2Theta between 35.5 and 40° (Fig. 1(D)). These additional weak diffraction maxima, indicating a lowering of the symmetry from hexagonal to monoclinic, could not be identified in the XRD datasets of the 2GaHAp and the 4GaHAp heat-treated at the same temperatures, either due to hexagonal symmetry or due to overlap with the secondary α-TCP phase. Hence, a monoclinic HAp structure template was used for *Rietveld* refinement of the HAp datasets. In contrast, the hexagonal structure template was used for all datasets of the 2GaHAp and 4GaHAp at 800–1200 °C, and for the as-synthesized datasets. Structure refinement of the hexagonal HAp phase in the dataset 4GaHAp heat-treated at 1100 °C with a Ga-free hexagonal structure model showed residual unfitted electron densities at the Ca1 position in F_{obs}-F_{calc} *Fourier*

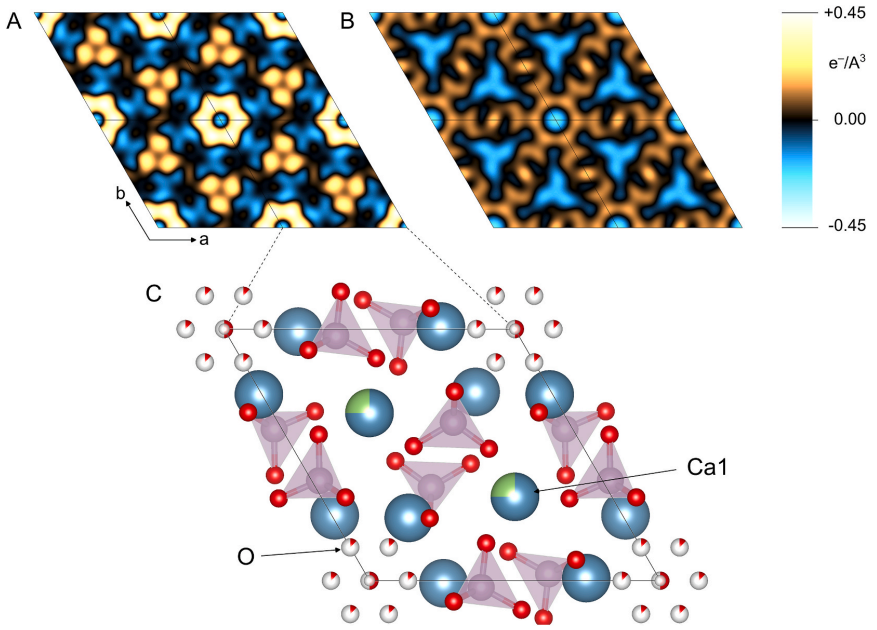

Fig. 3. F_{obs}-F_{calc} *Fourier* synthesis maps at $z = 0.0$ of the 4GaHAp sintered at 1100 °C, refined A – without and B – with the substitution model for Ga. The model is depicted schematically in C. "O" marks the additional oxygen ion compensating the charge imbalance introduced by Ga incorporation on "Ca1".

synthesis maps (Fig. 3(A)). In addition, excess electron densities were also found in the channel along the *c*-axis hosting the OH^- groups (Fig. 3 (A)).

From these signals, we derived a model for the substitution of Ga in the HAp structure. Ga^{3+} ions substitute for Ca^{2+} ions on the Ca1 site, thus introducing an additional positive charge. The charge imbalance is compensated by an additional anion site located in the channel at $x = 0.131$, $y = 0.000$, $z = 0.988$, represented in our refinement model by an additional O^{2-} ion. This uptake of additional ions can explain the unit cell volume expansion in the HAp structure due to the Ga addition. Refining this model with the 4GaHAp heat-treated at 1100 °C reduced residual electron densities in the F_{obs}-F_{calc} *Fourier* synthesis map (Fig. 3 (B)). The substitution model for the hexagonal HAp structure is schematically shown in Fig. 3(C). The refined Ga^{3+} content on the Ca1 site increased with increasing nominal Ga concentration. However, the presence of α-TCP diminished the resolution of the HAp diffraction signal. Hence, the quantification of Ga substitution by *Rietveld* refinement was not considered reliable.

3.2. Functional groups

The functional groups of the HAp and the GaHAp before and after sintering at temperatures ranging from 600 to 1200 °C were analyzed using ATR-FTIR spectra (Fig. 4).

The as-synthesized powders exhibited absorbance bands at 570–580 cm^{-1} attributed to the bending vibrations (ν_4) of PO_4^{3-} and bands centered at 900–1100 cm^{-1} derived from the symmetric and asymmetric stretching vibrations (ν_1 and ν_3) of PO_4^{3-}. Bands at 631 cm^{-1} corresponded to the librational mode (ν_L) of the hydroxyl OH^- groups [41]. Low-intensity absorbance bands were detected at approximately 1418 cm^{-1} and 879 cm^{-1}, attributed to CO_3^{2-} and HPO_4^{2-} groups [42]. The presence of CO_3^{2-} bands was due to a partial carbonation process of the synthesis products, due to the atmospheric CO_2 [43]. Substituting HPO_4^{2-} for PO_4^{3-} acts as a charge compensation mechanism for the cationic deficiency. CO_3^{2-} and HPO_4^{2-} absorbance bands disappeared after heat treatment [42]. The ATR-FTIR data correlated with the XRD data and confirmed the formation of a biphasic mixture of HAp and α-TCP after heat treatment of the 2GaHAp and the 4GaHAp (Fig. 4(B and C)). The difference with heat treatment appeared in the wavenumber region from 900 to 1100 cm^{-1}, where more significant distortion occurred as the heat treatment temperature increased (Fig. 4(A)). The absorbance bands characteristic of the α-TCP phase were detected after heat treatment at temperatures above 800 °C. Namely, the α-TCP PO_4^{3-} groups' absorbance bands at 900–1000 cm^{-1} due to the triple-degenerate asymmetric stretching ν_3, at 940–980 cm^{-1} due to the symmetric stretching ν_1, and at 400–500 cm^{-1} and 550–600 cm^{-1} due to the double and triple-degenerate bending ν_2 and ν_4 [44] were detected as "shoulders" which became more pronounced as the heat treatment temperature increased. In addition, an increase in α-TCP content promoted the decrease of OH^- groups' absorbance at ~3600 cm^{-1}. Moreover, in the case of the 2GaHAp and the 4GaHAp heat-treated above 1000 °C, additional peaks at 502, 734, and 928 cm^{-1} were detected. Their intensity increased with increasing Ga concentration (Fig. 4(D)). Nevertheless, concluding whether new functional groups are created is challenging because various phases and impurities have functional group bands overlapping in the same spectral region. Nonetheless, the presumed peaks might be ascribed to the possible formation of Ga-O bonds. Based on the literature, Ga_2O_3 heat-treated at 1000 °C contains bands (duplicates) in the region 400–850 cm^{-1} [45], and it corresponds to the region of formation of new groups in our study.

3.3. Thermal analysis

Thermal analysis was performed on the as-synthesized HAp, 2GaHAp, and 4GaHAp powders (Fig. 5). The region up to 300 °C corresponds to the dehydration of the samples [46]. The peaks around 50 °C were observed on the DTG curves. According to Refs. [47–49], in the temperature range 50–80 °C, desorption of surface adsorbed water

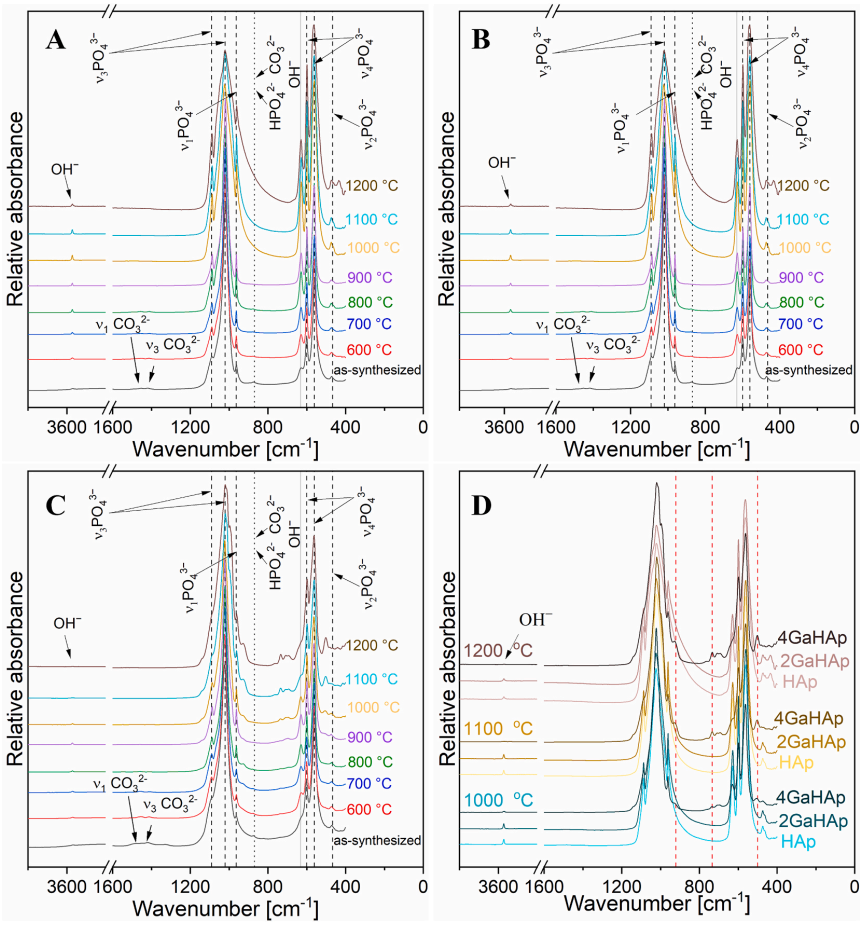

Fig. 4. ATR-FTIR spectra of the A – HAp, B – 2GaHAp, and C – 4GaHAp powders heat-treated at temperatures ranging from 600 to 1200 °C, D – revealing new functional group peaks (marked with red lines) for the samples heat-treated at 1000, 1100, and 1200 °C. (For interpretation of the references to colour in this figure legend, the reader is referred to the Web version of this article.)

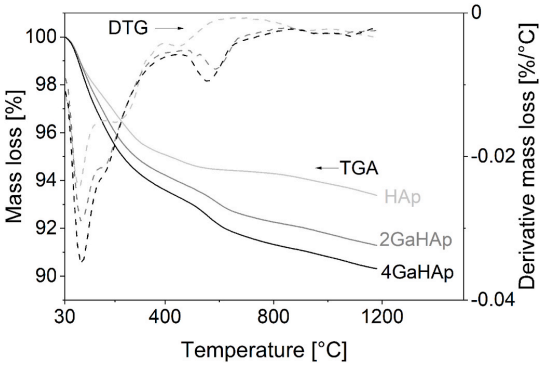

Fig. 5. Thermal analysis of the as-synthesized HAp, 2GaHAp, and 4GaHAp powders.

molecules occurs. In the HAp case, the surface adsorbed water loss resulted in a 1.5 % mass loss, 2GaHAp – 2.1 %, and 4GaHAp – 3.4 %. In turn, the peak shoulder from 80 to 300 °C is related to the water loss from the lattice, chemically bound water inside the pores, or chemisorbed water [50]. This accounted for a mass loss of 3.0 % in the case of HAp, 3.4 % – 2GaHAp, and 3.3 % – 4GaHAp. The temperature region 400–1100 °C corresponds to various thermal events related to crystallization and structural stabilization processes.

According to *Tõnsuaadu* et al., at ~900 °C, dehydroxylation of the HAp phase occurs [46]. The emergence of the additional peak in DTG at ~600 °C for the GaHAp samples can be associated with phase transformation during heat treatment and dihydroxylation that started at a lower temperature. The addition of Ga inhibited crystal growth, leading to the formation of the material with lower crystallinity and promoting the formation of the amorphous phase. It is suggested that at 600 °C, the amorphous part transforms to a more stable CaP. Furthermore, the quantity of the amorphous/low-crystalline phase increased as the Ga content increased, resulting in a higher mass loss of the GaHAp compared to pure HAp. The amorphous phase introduced extra water molecules to the structure due to the presence of a hydrated layer. The

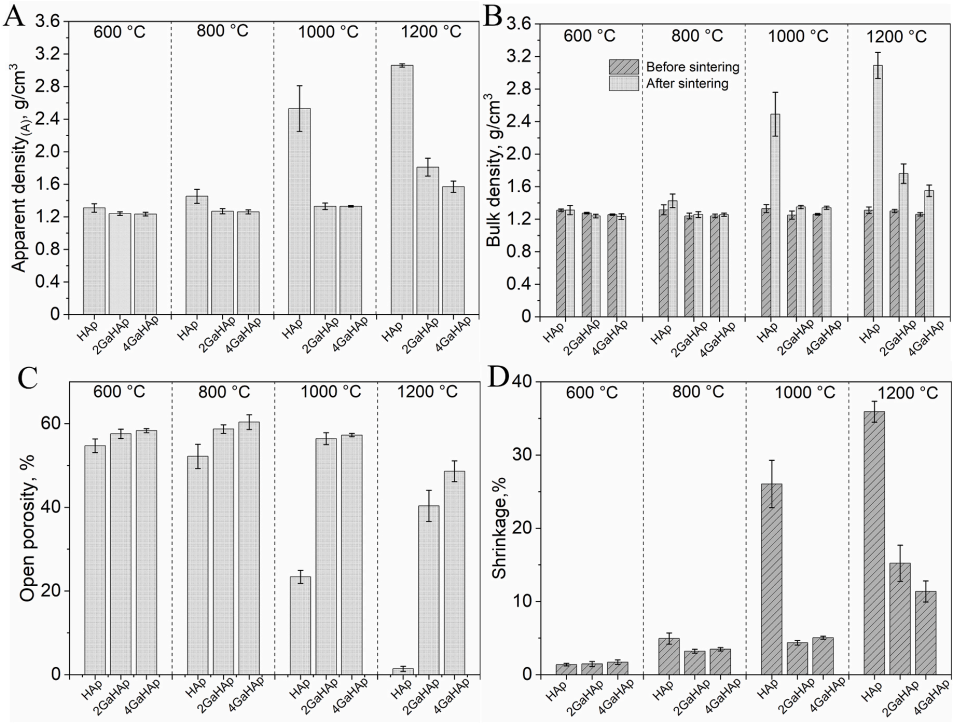

Fig. 6. A – apparent density, B – bulk density, C – open porosity by Archimedes' principle, and D – shrinkage of the HAp and GaHAp bioceramic pellets after sintering at 600 °C, 800 °C, 1000 °C, and 1200 °C.

totals mass loss at 1200 °C for HAp was 6.6 ± 0.4 %, for 2GaHAp – 9.3 ± 0.6 % and for 4GaHAp - 9.8 ± 0.3 %.

3.4. Density

Apparent density, open porosity, shrinkage, and bulk density of the HAp and GaHAp bioceramics sintered at 600, 800, 1000, and 1200 °C were determined and summarized in Fig. 6.

After sintering at 1100 and 1200 °C, the apparent density (Fig. 6(A)) and bulk density (Fig. 6(B)) of the 2GaHAp and 4GaHAp bioceramics were half that of the HAp bioceramics. The open porosity (Fig. 6(C)) was approximately 50 % higher than that of the HAp bioceramics. The shrinkage of the GaHAp bioceramics compared to the HAp was reduced by ~80 % (Fig. 6(D)). The densification process is affected by Ga's impact on crystal growth. Moreover, the formation of a secondary phase in the form of α-TCP significantly decreased densification.

3.5. Microstructure

SEM images confirmed the results of the density measurements, revealing significant differences between the HAp and GaHAp bioceramics microstructures sintered at different temperatures (Fig. 7).

At 600 (Fig. 7(A–C) and 800 °C (Fig. 7(D–F), a substantial difference in microporosity and grain sizes was not observed. Increasing the sintering temperature above 800 °C, *i.e.*, to 1000 °C (Fig. 7(G–I), 1100 °C (Fig. 7(J–L), 1200 °C (Fig. 7(M−O), led to an increase in grain sizes for both the HAp and GaHAp bioceramics. However, Ga promoted the formation of smaller grains and inhibited the densification of HAp regardless of the sintering temperature. As the sintering temperature exceeded 1000 °C, a compact structure consisting of individual hexagonal grains was observed in the case of the HAp bioceramics (Fig. 7(J–M)). At 1100 °C, the 2GaHAp (Fig. 7(K) and 4GaHAp (Fig. 7(L)) bioceramics had longitudinal-shaped grains. This is associated with grain growth in the *c*-direction. Formation of characteristic hexagonal grains was observed for the GaHAp bioceramics (Fig. 7(N and O) sintered at 1200 °C.

4. Discussion

In the present study, sintering of the GaHAp precursors, *i.e.*, HAp doping with Ga, led to the formation of biphasic CaP bioceramic composed of HAp and α-TCP phases. The refined α-TCP quantities in the Ga-free samples remained below their standard deviations and were thus considered to be below the detection limits. The presence of α-TCP in Ga-doped samples suggests that the Ca/P molar ratio of the synthesis products was less than for stoichiometric HAp, *i.e.*, <1.67. Thus, the syntheses products were CDHAp with chemical formula $Ca_{10-x-y}Ga_{x-y}(HPO_4)_y(PO_4)_{6-y}(OH)_{2-x-y}O_{x-y}$, where $x = 0.3$ (for 2GaHAp), 0.6 (for 4GaHAp), and $y = 10\text{-}6*Ca/P_{experimental}$. Experimental Ca/P was calculated from the relative proportion of the phases in heat-treated samples following the proposed procedure by *Raynaud* et al. [51]. For example, for the sample 2GaHAp at 1100 °C with a composition of 80.1 % HAp and 19.9 % α-TCP, $y = 0.211$, and 4GaHAp at 1100 °C with a composition of 72.8 % HAp and 27.2 % α-TCP, $y = 0.287$.

The α-TCP formed above 800 °C, and its ratio in the biphasic mixture increased with increasing Ga concentration. According to the literature, the stability of α-TCP is in the range of 1120–1430 °C and up to 1120 °C as a primary phase forms β-TCP, which then transforms to α-TCP [52, 53]. We observed that α-TCP formed at lower temperatures, *i.e.*, at 900 °C. *Martinez* et al. have reported that low-temperature α-TCP

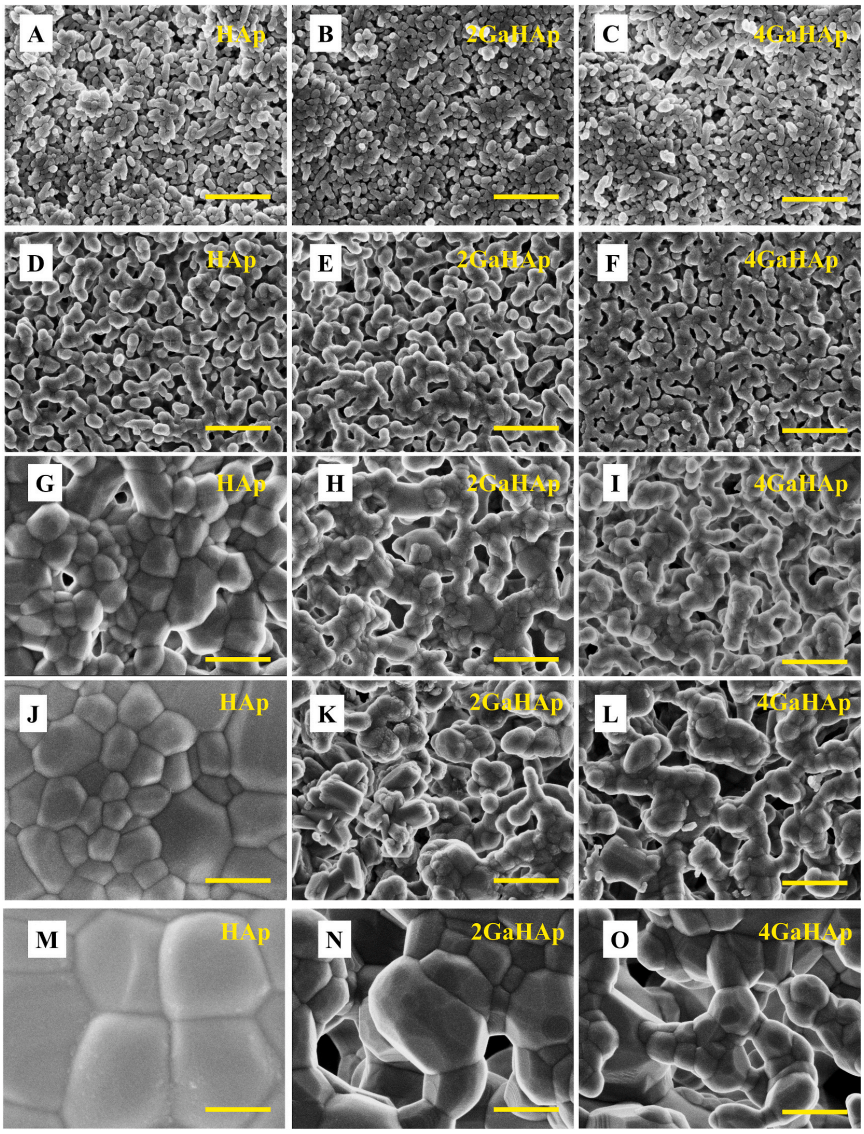

Fig. 7. SEM microphotographs of the A – HAp, B - 2GaHAp, and C – 4GaHAp bioceramic pellets sintered at 600 °C, D – HAp, E – 2GaHAp, F – 4GaHAp bioceramic pellets sintered at 800 °C, G – HAp, H – 2GaHAp, and I – 4GaHAp bioceramic pellets sintered at 1000 °C, J – HAp, K - 2GaHAp, L – 4GaHAp bioceramic pellets sintered at 1100 °C; M – HAp, N – 2GaHAp, and O – 4GaHAp bioceramic pellets sintered at 1200 °C. Scale bar – 500 nm.

(LT-α-TCP) can be obtained at 650 °C from amorphous CaP (ACP) with Ca/P molar ratio of 1.5 [54]. However, they also observed that LT-α-TCP gradually transforms to the β-TCP phase at temperatures above 650 °C. Moreover, *Sinusaite* et al. have suggested that the phase transformations between TCP polymorphs depend on the size and concentration of dopants in the ACP [55]. In our research, both the reduced Ca/P (resulting product is GaCDHAp) and the co-existence of an amorphous phase (reduction in crystallinity due to Ga addition) can promote the development of the α-form. Additionally, a low amount of impurities in the raw material (CaO) can further affect the physicochemical properties, including the thermal stability of CaP phases [56]. It is known that magnesium (Mg) has been shown to stimulate the formation of β-TCP at lower temperatures and increase the β→α transition temperature [46, 55]. As in the present work, the CaO used has a low concentration of Mg, which can also lead to the formation of α-TCP as a secondary phase. Nevertheless, due to the low intensity of secondary phases maxima, it is amiss to evaluate gallium intrusion into the TCP structure. Regarding the Ga effect, the structure refinement of the hexagonal HAp showed Ga incorporation into the Ca1 site in the HAp structure, leading to decreased crystallinity and, thus, disruption of the crystal lattice.

The presence of a secondary phase (TCP) can potentially improve the biodegradability of HAp bioceramics. Namely, the presence of more

soluble TCP could enhance the solubility of bioceramics, providing superior ion release and bioactivity [57]. Bioceramics becoming more reactive in biological environments can lead to enhanced formation of a biological apatite on the surface, promoting biomaterial's integration in bone tissues [58].

The observed preference of Ga to enter the HAp lattice structure is consistent with *Zhu* et al.'s proposed explanation that the ions with a smaller ionic radius than Ca tend to occupy the Ca(1) position [59]. Some authors have mentioned that Ga replaces Ca in the HAp lattice structure [60]. However, the specific position of Ga in the HAp crystal lattice was not determined. *Pereira Rocha* et al. proposed that Ga not only replaces Ca but is present in the hydrated or amorphous surface layer of HAp [31]. Poorly crystalline or nanocrystalline HAp was analyzed in the abovementioned studies. Meanwhile, heat-treated HAp was examined in our study, and during sintering, amorphous surface atoms become part of the ordered lattice. Substitution of smaller cations for Ca^{2+} in calcium phosphate phases often leads to a shrinkage of the unit cell volume, as was reported for Mg^{2+} substitution in HAp [61] and β-TCP [62]. In the case of Ga^{3+} substitution, we observed an opposite trend despite the substantially smaller ionic radius of $^{VI}Ga^{3+} = 0.760$ nm versus $^{VI}Ca^{2+} = 1.14$ nm [63]. A similar observation was reported by *Makshakova* et al. for Fe^{3+} substitution in HAp [64]. The unit cell expansion with increasing Ga concentration is most likely related to the incorporation of oxygen ions (O^{2-}) into the channel, replacing the hydroxyl ions (OH^-), to compensate for the additional positive charge introduced by Ga^{3+}.

The addition of Ga significantly influenced the sinterability of the HAp bioceramic at temperatures above 800 °C. According to *Mohammadi* et al., a lower Ca/P molar ratio (≤1.67) resulted in abnormal grain refinement consisting of a few coarse particles surrounded by finer grains. The authors attributed this unusual grain formation to the nucleation and growth of secondary phase crystals and further formations of different CaP phases [65]. In our study, the GaHAp bioceramics exhibited a similar microstructure (Fig. 7). Accordingly, the formation of micropores in the GaHAp bioceramics could be attributed to the formation of biphasic mixtures, where the secondary phase inhibits densification. It is related to the *Zener* pinning, where in the intermediate temperature during heat treatment, CDHAp transforms to the α-TCP and acts as a pinning agent, HAp remains as the matrix, and secondary phase forms dispersed particles at grain boundaries and inhibits grain growth [66]. Thus, in the case of the GaHAp, to obtain a denser bioceramic, higher sintering temperature and longer sintering time are required. This was supported by the increased density of the GaHAp bioceramics sintered at 1200 °C compared to lower temperatures. However, we can benefit from the microporous structure of biphasic GaCaP ceramics. Based on *Trzaskowska* et al. HAp sintered above 900 °C has low porosity, specific surface area (SSA), and bioactivity, and is not biodegradable [57]. Meanwhile, the presence of micropores increases SSA, affecting bioactivity and the ability to absorb liquids and adsorb proteins. The presence of macropores creates a surface essential for cell adhesion, proliferation, and tissue ingrowth [53].

5. Conclusions

The study presents the effect of gallium in a concentration up to 3.3 ± 0.4 wt% on the thermal stability of hydroxyapatite. Gallium affected the properties of the synthesized precursor powders. Hence, the as-synthesized powders contained calcium-deficient hydroxyapatite and amorphous phases, which led to the formation of biphasic calcium phosphates (mixture of hydroxyapatite and α-tricalcium phosphate) during sintering. Thus, doping of hydroxyapatite with gallium affected the phase composition and microstructure of the bioceramic after sintering. The secondary phase, α-tricalcium phosphate, was formed at 900 °C and above, and its content increased with increasing gallium concentration. The formation of the secondary phase during sintering significantly affected the microstructure of the obtained bioceramics. The microporous structure of the gallium-doped bioceramics was observed even at high sintering temperatures. Gallium-doped bioceramics had a density twice as low as that of pure hydroxyapatite bioceramics after sintering at 1200 °C. After sintering at 1200 °C, the porosity of gallium-doped bioceramics was 40.4 ± 3.7 % (2GaHAp) and 48.6 ± 2.5 % (4GaHAp), while for pure hydroxyapatite bioceramics it was only 1.1 ± 0.6 %. From full *Rietveld* refinement, we have created a theoretical substitutional model for gallium-doped hydroxyapatite. Incorporating gallium in the hydroxyapatite lattice occurs in the Ca1 position and introduces an additional positive charge. An additional anion site located in the OH channel is introduced to compensate for charge balance, expanding the hydroxyapatite unit cell volume.

CRediT authorship contribution statement

Marika Sceglova: Writing – review & editing, Writing – original draft, Visualization, Validation, Methodology, Investigation, Formal analysis, Data curation, Conceptualization. **Nicola Döbelin:** Writing – review & editing, Writing – original draft, Software, Resources, Investigation, Formal analysis, Data curation. **Renats Vasiljevs:** Methodology, Investigation, Data curation. **Liga Stipniece:** Writing – review & editing, Writing – original draft, Supervision, Investigation, Funding acquisition, Data curation, Conceptualization. **Janis Locs:** Writing – review & editing, Supervision, Resources, Project administration, Funding acquisition, Data curation.

Declaration of competing interest

The authors declare that they have no known competing financial interests or personal relationships that could have appeared to influence the work reported in this paper.

Acknowledgment

The authors acknowledge financial support for granting Open Access from the European Union's Horizon 2020 research and innovation programme under the grant agreement No. 857287 (BBCE – Baltic Biomaterials Centre of Excellence).

Appendix A. Supplementary data

Supplementary data to this article can be found online at https://doi.org/10.1016/j.ceramint.2025.06.440.

References

[1] E. Champion, Sintering of calcium phosphate bioceramics, Acta Biomater. 9 (2013) 5855–5875, https://doi.org/10.1016/j.actbio.2012.11.029.
[2] D.S. Gomes, A.M.C. Santos, G.A. Neves, R.R. Menezes, C. Grande, C. Grande, A brief review on hydroxyapatite production and use in biomedicine (Uma breve revisão sobre a obtenção de hidroxiapatita e aplicação na biomedicina), Cerâmica 65 (2019) 282–302, https://doi.org/10.1590/0366-69132019653742706.
[3] A. Haider, S. Haider, S.S. Han, I.-K. Kang, Recent advances in the synthesis, functionalization and biomedical applications of hydroxyapatite: a review, RSC Adv. 7 (2017) 7442–7458, https://doi.org/10.1039/C6RA26124H.
[4] D. Anandan, A.K. Jaiswal, Synthesis methods of hydroxyapatite and biomedical applications: an updated review, J. Austr. Ceramic Soc. 60 (2024) 663–679, https://doi.org/10.1007/s41779-023-00943-2.
[5] S. Mondal, S. Park, J. Choi, T.T.H. Vu, V.H.M. Doan, T.T. Vo, B. Lee, J. Oh, Hydroxyapatite: a journey from biomaterials to advanced functional materials, Adv. Colloid Interface Sci. 321 (2023) 103013, https://doi.org/10.1016/j.cis.2023.103013.
[6] X. Wang, S. Huang, Q. Peng, Metal ion-doped hydroxyapatite-based materials for bone defect restoration, Bioengineering 10 (12) (2023) 1367, https://doi.org/10.3390/bioengineering10121367.
[7] A. Noori, M. Hoseinpour, S. Kolivand, N. Lotfibakhshaiesh, S. Ebrahimi-Barough, J. Ai, M. Azami, Exploring the various effects of Cu doping in hydroxyapatite nanoparticle, Sci. Rep. 14, 3421. https://doi.org/10.1038/s41598-024-53704-x.
[8] Y. Li, D. Wang, S. Lim, Fabrication and applications of metal-ion-doped hydroxyapatite nanoparticles, JOJ Mater. Sci. 1 (2) (2017) 555558, https://doi.org/10.19080/JOJMS.2017.01.555559.

[9] K. Pajor, Ł. Pajchel, A. Zgadzaj, U. Piotrowska, J. Kolmas, Modifications of hydroxyapatite by gallium and silver ions—physicochemical characterization, cytotoxicity and antibacterial evaluation, Int. J. Mol. Sci. 21 (2020) 1–15, https://doi.org/10.3390/ijms21145006.
[10] D.-E. Radulescu, O.R. Vasile, E. Andronescu, A. Ficai, Latest research of doped hydroxyapatite for bone tissue engineering, Int. J. Mol. Sci. 24 (17) (2023) 13157, https://doi.org/10.3390/ijms241713157.
[11] S. Sprio, M. Dapporto, L. Preti, E. Mazzoni, M.R. Iaquinta, F. Martini, M. Tognon, N.M. Pugno, E. Restivo, L. Visai, A. Tampieri, Enhancement of the biological and mechanical performances of sintered hydroxyapatite by multiple ions doping, Front. Mater. 7 (2020), https://doi.org/10.3389/fmats.2020.00224.
[12] I. Cacciotti, Cationic and anionic substitutions in hydroxyapatite, in: I.V. Antoniac (Ed.), Handbook of Bioceramics and Biocomposites, Springer International Publishing, Switzerland, 2016, pp. 145–211, https://doi.org/10.1007/978-3-319-12460-5_7.
[13] A. Kurzyk, A. Szwed-Georgiou, J. Pagacz, A. Antosik, P. Tymowicz-Grzyb, A. Gerle, P. Szterner, M. Włodarczyk, P. Płociński, M.M. Urbaniak, K. Rudnicka, M. Biernat, Calcination and ion substitution improve physicochemical and biological properties of nanohydroxyapatite for bone tissue engineering applications, Sci. Rep. 13 (2023) 15384, https://doi.org/10.1038/s41598-023-42271-2.
[14] M. Mosina, I. Kovrlija, L. Stipniece, J. Locs, Gallium containing calcium phosphates: potential antibacterial agents or fictitious truth, Acta Biomater. 150 (2022) 48–57, https://doi.org/10.1016/j.actbio.2022.07.063.
[15] C.R. Chitambar, Gallium-containing anticancer compounds, Future Med. Chem. 4 (2012) 1257–1272, https://doi.org/10.4155/fmc.12.69.
[16] F. Minandri, C. Bonchi, E. Frangipani, F. Imperi, P. Visca, Promises and failures of gallium as an antibacterial agent, Future Microbiol. 9 (2014) 379–397, https://doi.org/10.2217/fmb.14.3.
[17] C.R. Chitambar, Gallium and its competing roles with iron in biological systems, biophys. Acta, Mol. Cell Res. 1863 (8) (2016) 2044–2053, https://doi.org/10.1016/j.bbamcr.2016.04.027.
[18] S.B. Hanaei, R.C. Murugesan, L. Souza, J.I. Cadiz-Miranda, L. Jeys, I.B. Wall, R. A. Martin, Multifunctional gallium doped bioactive glasses: a targeted delivery for antineoplastic agents and tissue repair against osteosarcoma, Biomed. Mater. 19 (6) (2023) 065008, https://doi.org/10.1088/1748-605X/AD76F1.
[19] H. Xi, X. Jiang, S. Xiong, Y. Zhang, J. Zhou, M. Liu, Z. Zhou, C. Zhang, S. Liu, Z. Long, J. Zhou, G. Qian, L. Xiong, 3D-printed gallium-infused scaffolds for osteolysis intervention and bone regeneration, Mater. Today Bio 31 (2025) 101524, https://doi.org/10.1016/j.mtbio.2025.101524.
[20] F. He, J. Rao, W. Fu, J. Zhou, Y. Zhang, T. Chen, W. Huang, Y. Wang, T. Lu, H. Shi, 3D printing and physicochemical and biological characterizations of gallium-containing magnesium/calcium phosphate ceramic scaffolds, Ceram. Int. 49 (21) (2023) 34173–34181, https://doi.org/10.1016/J.CERAMINT.2023.08.127.
[21] C. Mellier, F. Fayon, V. Schnitzler, P. Deniard, M. Allix, S. Quillard, D. Massiot, J. M. Bouler, B. Bujoli, P. Janvier, Characterization and properties of novel gallium-doped calcium phosphate ceramics, Inorg. Chem. 50 (17) (2011) 8252–8260, https://doi.org/10.1021/ic2007777.
[22] M. Shokri, M. Kharaziha, H. Ahmadi Tafti, F. Dalili, R. Mehdinavaz Aghdam, S. R. Ghiassi, M. Baghaban Eslaminejad, Melatonin-loaded mesoporous zinc- and gallium-doped hydroxyapatite nanoparticles to control infection and bone repair, Biomater. Sci. 12 (2024) 4194–4210, https://doi.org/10.1039/D4BM00377B.
[23] W. Shuai, J. Zhou, C. Xia, S. Huang, J. Yang, L. Liu, H. Yang, Gallium-doped hydroxyapatite: shape transformation and osteogenesis activity, Molecules 28 (21) (2023) 7379, https://doi.org/10.3390/molecules28217379.
[24] M. Kurtjak, M. Vukomanović, A. Krajnc, L. Kramer, B. Turk, D. Suvorov, Designing Ga(III)-containing hydroxyapatite with antibacterial activity, RSC Adv. 6 (114) (2016) 112839–112852, https://doi.org/10.1039/c6ra23424k.
[25] M. Kurtjak, M. Vukomanović, D. Suvorov, Antibacterial nanocomposite of functionalized nanogold and gallium-doped hydroxyapatite, Mater. Lett. 193 (2017) 126–129, https://doi.org/10.1016/j.matlet.2017.01.092.
[26] M. Shokri, M. Kharaziha, H.A. Tafti, M.B. Eslaminejad, R.M. Aghdam, Synergic role of zinc and gallium doping in hydroxyapatite nanoparticles to improve osteogenesis and antibacterial activity, Biomater. Adv. 134 (2022) 112684, https://doi.org/10.1016/j.msec.2022.112684.
[27] S. Gokyer, Y.A. Monsef, S. Buyuksungur, J. Schmidt, A.V. Dragomir, S. Uygur, C. Oto, K. Orhan, V. Hasirci, N. Hasirci, P. Yilgor, MgCa-Based alloys modified with Zn- and Ga-Doped CaP coatings lead to controlled degradation and enhanced bone formation in a sheep cranium defect model, ACS Biomater. Sci. Eng. 10 (7) (2024) 4452–4462, https://doi.org/10.1021/acsbiomaterials.4c00358.
[28] N.H. Nguyen, P. Zhang, F.S.P. Kadavan, Z. Xu, T.T. Nguyen, et al., Multifunctional hydroxyapatite coated with gallium liquid metal-based silver nanoparticles for infection prevention and bone regeneration, Adv. Funct. Mater. (2025) 2423496, https://doi.org/10.1002/adfm.202423496.
[29] M. Mosina, C. Siverino, L. Stipniece, A. Sceglovs, R. Vasiljevs, T.F. Moriarty, J. Locs, Gallium-doped hydroxyapatite shows antibacterial activity against Pseudomonas aeruginosa without affecting cell metabolic activity, J. Funct. Biomater. 14 (2) (2023) 51, https://doi.org/10.3390/jfb14020051.
[30] P. Melnikov, A.R. Teixeira, A. Malzac, M.D.B. Coelho, Gallium-containing hydroxyapatite for potential use in orthopedics, Mater. Chem. Phys. 117 (1) (2009) 86–90, https://doi.org/10.1016/j.matchemphys.2009.05.046.
[31] R.L. Pereira Rocha, T.L. Silva, F.P. Araujo, E.G. Vieira, L.M. Honório, M.B. Furtini, M.G. Da Fonseca, E.C. Da Silva-Filho, J.A. Osajima, Gallium-containing hydroxyapatite as a promising material for photocatalytic performance, Minerals 11 (12) (2021) 1347, https://doi.org/10.3390/min11121347.
[32] S. Ponnusamy, R. Subramani, S. Elangomannan, K. Louis, M. Periasamy, G. Dhanaraj, Novel strategy for gallium-substituted Hydroxyapatite/pergularia daemia fiber extract/poly(N-vinylcarbazole) biocomposite coating on titanium for biomedical applications, ACS Omega 6 (35) (2021) 22537–22550, https://doi.org/10.1021/acsomega.1c02186.
[33] N. Doebelin, R. Kleeberg, Profex: a graphical user interface for the rietveld refinement program BGMN, J. Appl. Crystallogr. 48 (5) (2015) 1573–1580, https://doi.org/10.1107/S1600576715014685.
[34] The International Centre for Diffraction Data. https://www.icdd.com, 2024 (accessed 22 October 2024).
[35] J. Bergmann, P. Friedel, R. Kleeberg, BGMN – a New Fundamental Parameters Based Rietveld Program for Laboratory X-Ray Sources, its Use in Quantitative Analysis and Structure Investigations, CPD, 1998, pp. 5–8.
[36] K. Lin, J. Chang, Structure and Properties of Hydroxyapatite for Biomedical Applications, Hydroxyapatite (Hap) for Biomedical Applications, Woodhead Publishing Series in Biomaterials, 2015, pp. 3–19, https://doi.org/10.1016/B978-1-78242-033-0.00001-8.
[37] C. Stähli, A.J. Salinas, N. Döbelin, A. Testino, M. Bohner, Density and phase-purity of α-TCP obtained by sintering of nano-crystalline powder, Ceram. Int. 50 (6) (2024) 8586–8593, https://doi.org/10.1016/J.CERAMINT.2023.07.068.
[38] M.C. Tronco, J.B. Cassel, L.A. dos Santos, α-TCP-based calcium phosphate cements: a critical review, Acta Biomater. 151 (1) (2022) 70–87, https://doi.org/10.1016/j.actbio.2022.08.040.
[39] M. Yashima, A. Sakai, High-temperature neutron powder diffraction study of the structural phase transition between α and α′ phases in tricalcium phosphate $Ca_3(PO_4)_2$, Chem. Phys. Lett. 372 (5–6) (2003) 779–783, https://doi.org/10.1016/S0009-2614(03)00505-0.
[40] M. Yashima, Y. Kawaike, M. Tanaka, Determination of precise unit-cell parameters of the α-Tricalcium phosphate $Ca_3(PO_4)_2$ through high-resolution synchrotron powder diffraction, J. Am. Chem. Soc. 90 (1) (2007) 272–274, https://doi.org/10.1111/J.1551-2916.2006.01375.X.
[41] F. Mohandes, E. Gómez, A. Serrà, Surface modification of hierarchical hydroxyapatite fabricated via hydrothermal method, Ceram. Int. 50 (11-A) (2024) 19283–19292, https://doi.org/10.1016/j.ceramint.2024.03.027.
[42] K. Salma, N. Borodajenko, A. Plata, L. Berzina-Cimdina, A. Stunda, Fourier transform infrared spectra of technologically modified calcium phosphates, IFMBE Proc. 20 (2008) 68–711, https://doi.org/10.1007/978-3-540-69367-3_19.
[43] S. Dey, M. Das, V.K. Balla, Effect of hydroxyapatite particle size, morphology and crystallinity on proliferation of colon cancer HCT116 cells, Mater. Sci. Eng. C 39 (2014) 336–339, https://doi.org/10.1016/J.MSEC.2014.03.022.
[44] M. Motisuke, R.G. Carrodeguas, C.A. de C. Zavaglia, Si-tricalcium phosphate cement: preparation, characterization and bioactivity in SBF, Math. Res. 14 (4) (2011) 493–498, https://doi.org/10.1590/S1516-14392011005000065.
[45] N. Vorobyeva, M. Rumyantseva, V. Platonov, D. Filatova, A. Chizhov, A. Marikutsa, I. Bozhev, A. Gaskov, Ga_2O_3(Sn) oxides for high-temperature gas sensors, Nanomaterials 11 (11) (2021) 2938, https://doi.org/10.3390/nano11112938.
[46] K. Tõnsuaadu, K.A. Gross, L. Plüduma, M. Veiderma, A review on the thermal stability of calcium apatites, J. Therm. Anal. Calorim. 110 (2012) 647–659, https://doi.org/10.1007/s10973-011-1877-y.
[47] D.P. Minh, M.G. Martinez, A. Nzihou, P. Sharrock, Thermal behavior of apatitic calcium phosphates synthesized from calcium carbonate and orthophosphoric acid or potassium dihydrogen orthophosphate, J. Therm. Anal. Calorim. 112 (2013) 1145–1155, https://doi.org/10.1007/s10973-012-2695-6.
[48] M.S. Djošić, V.B. Mišković-Stanković, S. Milonjić, Z.M. Kačarević-Popović, N. Bibić, J. Stojanović, Electrochemical synthesis and characterization of hydroxyapatite powders, Mater. Chem. Phys. 111 (1) (2008) 137–142, https://doi.org/10.1016/j.matchemphys.2008.03.045.
[49] P. Szterner, M. Biernat, Effect of reaction time, heating and stirring rate on the morphology of HAp obtained by hydrothermal synthesis, J. Therm. Anal. Calorim. 147 (2022) 13059–13071, https://doi.org/10.1007/s10973-022-11564-5.
[50] N. V Bulina, S. V Makarova, S.G. Baev, A.A. Matvienko, K.B. Gerasimov, O. A. Logutenko, V.S. Bystrov, A study of thermal stability of hydroxyapatite, Minerals 11 (12) (2021) 1310, https://doi.org/10.3390/min11121310.
[51] S. Raynaud, E. Champion, D. Bernache-Assollant, J.P. Laval, Determination of calcium/phosphorus atomic ratio of calcium phosphate apatites using X-ray diffractometry, J. Am. Ceram. Soc. 84 (2) (2001) 359–366, https://doi.org/10.1111/J.1151-2916.2001.TB00663.X.
[52] F. He, Y. Tian, Improvements in phase stability and densification of β-tricalcium phosphate bioceramics by strontium-containing phosphate-based glass additive, Ceram. Int. 44 (10) (2018) 11622–11627, https://doi.org/10.1016/j.ceramint.2018.03.236.
[53] J. Liu, L. Zhao, L. Ni, C. Qiao, D. Li, H. Sun, Z. Zhang, The effect of synthetic α-tricalcium phosphate on osteogenic differentiation of rat bone mesenchymal stem cells, Am. J. Transl. Res. 7 (9) (2015) 1588–1601. https://www.ncbi.nlm.nih.gov/pmc/articles/PMC4626420/.
[54] T. Martinez, M. Espanol, C. Charvillat, O. Marsan, M.P. Ginebra, C. Rey, S. Sarda, α-tricalcium phosphate synthesis from amorphous calcium phosphate: structural characterization and hydraulic reactivity, J. Mater. Sci. 56 (2021) 13509–13523, https://doi.org/10.1007/s10853-021-06161-0.
[55] L. Sinusaite, A. Kareiva, A. Zarkov, Thermally induced crystallization and phase evolution of amorphous calcium phosphate substituted with divalent cations having different sizes, Cryst. Growth Des. 21 (2) (2021) 1242–1248, https://doi.org/10.1021/acs.cgd.0c01534.
[56] K. Salma-Ancane, L. Stipniece, Z. Irbe, Effect of biogenic and synthetic starting materials on the structure of hydroxyapatite bioceramics, Ceram. Int. 42 (8) (2016) 9504–9510, https://doi.org/10.1016/J.CERAMINT.2016.03.028.

[57] M. Trzaskowska, V. Vivcharenko, A. Przekora, The impact of hydroxyapatite sintering temperature on its microstructural, mechanical, and biological properties, Int. J. Mol. Sci. 24 (6) (2023) 5083, https://doi.org/10.3390/ijms24065083.
[58] M. Prakasam, J. Locs, K. Salma-Ancane, D. Loca, A. Largeteau, L. Berzina-Cimdina, Fabrication, properties and applications of dense hydroxyapatite: a review, J. Funct. Biomater. 6 (4) (2015) 1099–1140, https://doi.org/10.3390/jfb6041099.
[59] X.D. Zhu, H.J. Zhang, H.S. Fan, W. Li, X.D. Zhang, Effect of phase composition and microstructure of calcium phosphate ceramic particles on protein adsorption, 6, Acta Biomater. 6 (4) (2010) 1536–1541, https://doi.org/10.1016/j.actbio.2009.10.032.
[60] A. Ballardini, M. Montesi, S. Panseri, A. Vandini, P.G. Balboni, A. Tampieri, S. Sprio, New hydroxyapatite nanophases with enhanced osteogenic and antibacterial activity, J. Biomed. Mater. Res., Part A 106 (2) (2018) 521–530, https://doi.org/10.1002/jbm.a.36249.
[61] A. Bigi, G. Falini, E. Foresti, M. Gazzano, A. Ripamonti, N. Roveri, Rietveld structure refinements of calcium hydroxylapatite containing magnesium, Acta Crystallogr. B 52 (1996) 87–92, https://doi.org/10.1107/S0108768195008615.
[62] R. Enderle, F. Götz-Neunhoeffer, M. Göbbels, F.A. Müller, P. Greil, Influence of magnesium doping on the phase transformation temperature of β-TCP ceramics examined by rietveld refinement, Biomaterials 26 (17) (2005) 3379–3384, https://doi.org/10.1016/j.biomaterials.2004.09.017.
[63] R.D. Shannon, Revised Effective Ionic Radii and Systematic Studies of Interatomic Distances in Halides and Chalcogenides, vol. 32, 1976, pp. 751–767, https://doi.org/10.1107/S0567739476001551, 5.
[64] O.N. Makshakova, D.V. Shurtakova, A.V. Vakhin, P.O. Grishin, M.R. Gafurov, Incorporation of iron(II) and (III) in hydroxyapatite—A theoretical study, Crystals 11 (10) (2021) 1219, https://doi.org/10.3390/cryst11101219.
[65] M. Mohammadi, J.M. Tulliani, L. Montanaro, P. Palmero, Gelcasting and sintering of hydroxyapatite materials: effect of particle size and Ca/P ratio on microstructural, mechanical and biological properties, J. Eur. Ceram. Soc. 41 (14) (2021) 7301–7310, https://doi.org/10.1016/j.jeurceramsoc.2021.07.025.
[66] D. Fan, L.Q. Chen, S.P.P. Chen, Numerical simulation of zener pinning with growing second-phase particles, J. Am. Ceram. Soc. 81 (3) (1998) 526–532, https://doi.org/10.1111/j.1151-2916.1998.tb02370.x.

Marika Ščeglova was born in 1994 in Riga, Latvia. She obtained a Bachelor's degree in Engineering (2018) and a Master's degree in Engineering in Chemical Technology (2020) from Riga Technical University (RTU). From 2013 to 2018, she worked at JSC Grindeks. From 2018 to 2025, she was a researcher at the Institute of Biomaterials and Bioengineering, Faculty of Natural Sciences and Technology, RTU. Her research interests focus on calcium phosphate biomaterials and their modification with various ions to improve physicochemical and biological properties. The results of her research have been presented at international scientific conferences and published in scientific journals. Currently, she works as a chemistry teacher.